SINTERING AND PHASE TRANSITION BEHAVIOUR OF SODIUM NIOBATE

Jurij Koruza

Doctoral Dissertation
Jožef Stefan International Postgraduate School
Ljubljana, Slovenia, February 2013

Evaluation Board:

Prof. Dr. Tomaž Kosmač, Engineering Ceramics Department, Jožef Stefan Institute, Jamova cesta 39, 1000 Ljubljana, Slovenia

Prof. Dr. Jürgen Rödel, Division for Nonmetallic-Inorganic Materials, Technische Universität Darmstadt, Petersenstraße 23, 64287 Darmstadt, Germany

Prof. Dr. Boštjan Markoli, Faculty of Natural Sciences and Engineering, University of Ljubljana, Aškerčeva cesta 12, 1000 Ljubljana, Slovenia

Prof. Dr. Klaus Reichmann, Institute for Chemistry and Technology of Materials, Graz University of Technology, Rechbauerstraße 12, 8010 Graz, Austria

MEDNARODNA PODIPLOMSKA ŠOLA JOŽEFA STEFANA
JOŽEF STEFAN INTERNATIONAL POSTGRADUATE SCHOOL

Jurij Koruza

SINTERING AND PHASE TRANSITION BEHAVIOUR OF SODIUM NIOBATE

Doctoral Dissertation

SINTRANJE IN FAZNE PREMENE NATRIJEVEGA NIOBATA

Doktorska disertacija

Supervisor: Prof. Dr. Barbara Malič

Co-Supervisor: Dr. Tadej Rojac

Ljubljana, Slovenia, February 2013

Index

Abstract

Sodium niobate ($NaNbO_3$) is the end member of several alkaline niobate-based solid solutions, which represent an important group of environment-friendly lead-free piezoceramics. Even though alkaline niobates are of considerable technological importance, problems in obtaining high densities and a fine-grained microstructure are still reported and not much is known about the basic mechanisms that take place during sintering. In addition, $NaNbO_3$ is interesting in its pure form, being a prototype antiferroelectric, exhibiting a complex, displacive phase-transition behaviour. Besides the temperature- and electric-field-induced transitions, size-induced phase-transition phenomena have been observed; however, controversy regarding the phase-transition behaviour still remains in the literature. In order to investigate the above-described problems, the present work was focused on the following topics: the preparation of $NaNbO_3$ powders, the sintering behaviour of $NaNbO_3$ ceramics and an investigation of the phase-transition behaviour of the obtained samples.

The submicron-sized $NaNbO_3$ powder was prepared by solid-state synthesis, while for the preparation of the nano-sized powder a top-down processing route was introduced, combining solid-state synthesis and agitator bead milling. The optimized milling parameters resulted in the production of the nanopowder with particle sizes of 25–30 nm and a narrow particle size distribution, which was comparable to the results obtained by other processing techniques based on the bottom-up approach, such as the solution-based chemical routes or mechanochemical synthesis. The nanopowder exhibited better compactability at isostatic pressures above 550 MPa than the submicron-sized powder, which resulted in higher relative green densities. In all the powder compacts, uniform pore-size distributions were observed with average pore-radius values of 4–10 nm and 20–30 nm for the nano- and the submicron-sized samples, respectively; however, the pore-size distributions were much broader for the coarser powder.

The sintering behaviour of the submicron- and nano-sized $NaNbO_3$ powder compacts was studied using optical dilatometry and microstructure analysis. All the samples exhibited similar dynamic sintering curves with a very narrow shrinkage interval just before reaching the melting point at approximately 1410 °C. Despite the different densification-onset temperatures, both samples reached the same relative density at 1280 °C and above this temperature their densification curves almost coincided, which indicated that the initial differences in particle sizes disappeared before the samples reached the main densification stage, as confirmed by the microstructure analysis. Similar developments of the microstructure were observed in all $NaNbO_3$ samples, regardless of the initial powder particle size or the applied heating rate, which indicated the dominance of the grain-growth processes during the initial sintering stage, well before the onset of densification. The cause of this behaviour was found to be the surface diffusion that, due to its estimated low activation energy of 50–60 kJ/mol, became activated already during the initial sintering stage. As a non-densifying material-transport mechanism, the surface diffusion initiated grain coarsening, reduced the sintering driving force and was thus identified as the primary cause of the difficulties in obtaining high densities and fine-grained microstructures in $NaNbO_3$. In addition, the investigations of the sintering

behaviour during the intermediate sintering stage indicated the dominance of the grain-boundary diffusion, which was related to the use of very fine particles. The results obtained from the Knudsen effusion mass spectrometry indicated a negligible vapour pressure of Na over $NaNbO_3$ during the initial sintering stage, while the vapour pressure increased to $1.6 \cdot 10^{-5}$ bar at 1350 °C, which suggested that the material transport via the vapour phase becomes increasingly important during the later stages of sintering.

In order to overcome the densification and coarsening problems, we applied pressure-assisted sintering using different temperatures, 1100 °C and 1150 °C, and different periods of time, 3 h and 6 h. The application of the external pressure resulted in a successful impediment of the surface diffusion due to the reduction of the total free surface area during the initial sintering stage and the increased grain-boundary area, which provided material transport paths for grain-boundary diffusion and thus enhanced densification. The highest relative density (98 %) and the smallest average grain size (0.70±0.29 μm) were obtained when sintering for 6 h at 1150 °C.

The phenomenon of abnormal grain growth (AGG) during conventional atmosphere sintering of $NaNbO_3$ ceramics was addressed. The samples sintered for 0–10 min at 1350 °C consisted of grains with average sizes of 2.5–2.9 μm and a uniform grain-size distribution; however, once the sintering time was increased to 15 min, a few large grains of several 10 μm were observed, while the grain size of the matrix remained as 2.8–2.9 μm. The AGG was related to the decreased quantity of pores and their sizes and the resulting increase in the grain-boundary-migration velocity, which exceeded the pore-migration velocity and initiated the pore/grain-boundary separation. A further increase of the sintering time resulted in a microstructure with an average grain size of 35–55 μm and a relative density of 95–96 %.

The temperature-induced phase transitions were first re-examined on a coarse-grained $NaNbO_3$ ceramic (grain size of approximately 50 μm) using differential scanning calorimetry (DSC), dielectric spectroscopy and high-temperature X-ray diffraction (XRD). We confirmed the presence of the antiferroelectric *P* phase at room temperature, which upon heating underwent the following transitions: 371.4 °C (*P*→*R*), 511 °C (*S*→*T(1)*), 564.7 °C (*T(1)*→*T(2)*), and 642.4 °C (*T(2)*→*U*). In addition, another anomaly was observed in the permittivity curve in the vicinity of 150 °C, but was not detected using DSC and XRD. The detailed dielectric analysis revealed the frequency dependence of the ε''(T) peaks, which excluded the presence of a phase transition in this temperature region.

The comparison of the coarse-grained ceramics and the submicron-NN powder (particle size 0.07–0.17 μm) revealed a difference of about 50 °C in the temperatures of the main transition peak, which was related to the stabilization of the ferroelectric *Q* phase in the case of the submicron-NN, as confirmed by XRD. During heating, the ferroelectric *Q* phase underwent a *Q*→*R* transition between 265 °C and 325 °C.

In order to investigate the size-induced phase transitions in $NaNbO_3$ ceramics, we prepared a series of samples with grain sizes ranging from about 0.15 μm to 50 μm. The decrease of the grain size from 50 μm to 0.62 μm resulted in a decrease of the *P*→*R* transition temperature. Upon decreasing the grain size to 0.23 μm, we observed the occurrence of the ferroelectric *Q* phase, the amount of which increased with a further decrease of the grain size to 0.19 μm, while the amount of the antiferroelectric *P* phase decreased. At a grain size of about 0.15 μm, only the ferroelectric *Q* phase was detected. The critical grain size for the inducement of the *P*→*Q* transition was found to be roughly about 0.2 μm.

Finally, we investigated the phase transition induced by the application of an external electric field. The antiferroelectric *P* phase was found to transform to the ferroelectric *Q*

phase upon applying an electric field of 8 kV/mm at 80 °C, as confirmed by the occurrence of the ferroelectric polarization hysteresis loops, the butterfly-like strain hysteresis loops and the XRD analysis. The obtained remanent polarization was 32 μC/cm^2 and the d_{33} piezoelectric coefficient was 28 pC/N. The induced ferroelectric state remained stable upon removal of the electric field and upon decreasing the temperature to room temperature, which indicated the irreversible nature of this $P \rightarrow Q$ phase transition.

Povzetek

Natrijev niobat ($NaNbO_3$) je mejna spojina številnih trdnih raztopin alkalijskih niobatov, ki so pomembna skupina okolju prijaznih piezoelektrikov brez svinca. Eden izmed osnovnih problemov pri pripravi alkalijskih niobatov je doseganje velike gostote in hkrati drobnozrnate mikrostrukture, kar lahko delno povežemo s pomanjkljivim razumevanjem osnovnih mehanizmov procesa sintranja. Spojina $NaNbO_3$ je prototipni antiferoelektrik z zapletenim zaporedjem faznih premen, o katerem obstajajo kljub dolgoletnim raziskavam neenotni literaturni podatki. Delo je tematsko razdeljeno na naslednja področja: priprava keramičnih prahov, preiskovanje procesa sintranja in študij faznih premen $NaNbO_3$ pod vplivom temperature, električnega polja in velikosti delcev.

Prah $NaNbO_3$ s submikronsko velikostjo delcev smo pripravili s sintezo v trdnem stanju, medtem ko smo za pripravo nanoprahu $NaNbO_3$ razvili postopek, ki združuje sintezo v trdnem stanju in koloidno kroglično mletje. Z optimizacijo procesa smo pripravili nanoprahove z velikostjo delcev med 25 in 30 nm ter ozko porazdelitvijo velikosti delcev, kar je primerljivo z rezultati priprave nanoprahov po drugih postopkih, kot sta na primer mehanokemijska sinteza in sinteza prahov iz raztopin. V nanoprahovih smo izmerili približno 2 % mikrodeformacijo, kar bi lahko bila posledica defektov, nastalih med procesom mletja. Surovci iz nanoprahov, pripravljeni z izostatsim stiskanjem, so v tlačnem območju nad 550 MPa dosegli večje zelene gostote kot surovci iz prahov s submikronsko velikostjo delcev. Srednja velikost por v zelenih vzorcih je bila 4–10 nm pri vzorcih, pripravljenih iz nanoprahov, in 20–30 nm pri vzorcih iz submikronskega prahu. Porazdelitve velikosti por so bile v vseh primerih monomodalne, vendar pa so bile le-te v primeru nanoprahov precej ožje.

Proces sintranja vzorcev $NaNbO_3$ s submikronsko in nanometrsko začetno velikostjo delcev smo preiskovali z optično dilatometrijo in mikrostrukturno analizo. Pri obeh vzorcih smo opazili podoben potek dinamične krivulje sintranja s pojavom značilnega ozkega temperaturnega intervala zgoščevanja tik pod tališčem materiala okoli 1400 °C. Navkljub različnim temperaturam začetka zgoščevanja sta pri 1280 °C oba vzorca dosegla enako relativno gostoto in se med nadaljnjim segrevanjem zgoščevala z enako hitrostjo, na podlagi česar smo sklepali, da začetne razlike med vzorcema izginejo, še preden dosežeta glavno stopnjo zgoščevanja, kar smo potrdili z mikrostrukturno analizo. Opazili smo, da začetna velikost delcev in hitrost segrevanja ne vplivata na razvoj mikrostrukture keramike $NaNbO_3$, kar je nakazovalo prevlado procesov rasti zrn v začetni stopnji sintranja, pred pričetkom zgoščevanja. Z metodo meritve zmanjševanja specifične površine med segrevanjem smo ugotovili, da je glavni razlog za opaženo rast površinska difuzija, ki se zaradi ocenjene nizke aktivacijske energije (50–60 kJ/mol) aktivira že med začetno stopnjo sintranja, kar zmanjšuje gonilno silo za sintranje in posledično zavira zgoščevanje. Na podlagi rezultatov sklepamo, da je rast zrn v začetni stopnji sintranja zaradi površinske difuzije glavna ovira za zgoščevanje in doseganje drobnozrnate mikrostrukture v keramiki $NaNbO_3$. Prav tako smo preiskovali mehanizme prenosa materiala v srednji stopnji sintranja, pri čemer smo opazili prevlado difuzije po mejah zrn, kar smo pripisali uporabi drobnozrnatih začetnih prahov. Z metodo Knudsenove efuzije,

sklopljene z masnim spektrometrom, smo dokazali zanemarljiv vpliv parnega tlaka natrija v začetni stopnji sintranja, medtem ko je vpliv le-tega v kasnejših stopnjah znatnejši in dopušča možnost aktivacije mehanizma prenosa materiala preko parne faze.

Da bi pripravili gosto in drobnozrnato keramiko $NaNbO_3$, smo uporabili metodo sintranja pod pritiskom pri različnih temperaturah, 1100 °C in 1150 °C, ter različnih časih sintranja, 3 h in 6 h. Z uporabo zunanjega tlaka med segrevanjem smo zmanjšali skupno prosto površino delcev v začetni stopnji sintranja in tako uspešno zavrli površinsko difuzijo, prav tako pa smo zaradi povečanja skupne površine mej ustvarili nove difuzijske poti za difuzijo po mejah zrn in s tem pospešili zgoščevanje. S sintranjem pod pritiskom, pri temperaturi 1150 °C in času 6 h, smo pripravili keramiko z relativno gostoto 98 % in povprečno velikostjo zrn 0,70±0,29 μm.

V nadaljevanju smo preiskovali pojav prekomerne rasti zrn, ki smo ga opazili med konvencionalnim sintranjem keramike $NaNbO_3$ pri temperaturi 1350 °C v zraku. Vzorci, sintrani med 0 min in 10 min, so imeli enakomerno porazdelitev velikosti zrn s povprečno velikostjo med 2,5 μm in 2,9 μm, medtem ko smo v vzorcih, sintranih 15 min, poleg matričnih zrn z velikostjo 2,8–2,9 μm opazili tudi nekaj zrn z velikostjo več 10 μm. Razloga za pojav prekomerne rasti zrn sta bila zmanjšanje števila por in njihovih velikosti. Posledica je bila povečana hitrost migracije mej, ki je v določenem trenutku prekoračila hitrost migracije por in privedla do ločitve mej od por. Z nadaljnjim podaljševanjem časa sintranja smo pripravili keramiko z velikostjo zrn 35–55 μm in relativno gostoto 95–96 %.

Fazne premene grobozrnate keramike $NaNbO_3$ (velikost zrn približno 50 μm) med segrevanjem smo preiskovali z metodami diferenčne dinamične kalorimetrije (DSC), dielektrične spektroskopije in visokotemperaturne rentgenske difrakcije (XRD). Potrdili smo obstoj antiferoelektrične faze *P* pri sobni temperaturi in med segrevanjem opazili naslednje zaporedje faznih prehodov: 371,4 °C (*P*→*R*), 511 °C (*S*→*T(1)*), 564,7 °C (*T(1)*→*T(2)*) in 642,4 °C (*T(2)*→*U*). V krivuljah dielektričnosti v odvisnosti od frekvence in temperature smo v bližini temperature 150 °C opazili dodatno anomalijo, katere z metodami DSC in XRD nismo zaznali. Pri natančni analizi dielektričnega odziva smo opazili frekvenčno odvisnost vrhov imaginarnega dela dielektričnosti *ε''(T)*, kar izključuje možnost obstoja fazne premene v tem temperaturnem območju.

Pri primerjavi DSC krivulj grobozrnate keramike in prahu s submikronsko velikostjo delcev (0,07–0,17 μm) smo opazili približno 50 °C razliko med temperaturama obeh glavnih uklonov. Z XRD analizo smo ugotovili, da je opažena razlika posledica stabilizacije feroelektrične faze *Q* v submikronskem prahu, ki se pri segrevanju med 265 °C in 325 °C pretvori v fazo *R*.

Da bi raziskali vpliv velikosti zrn na fazno sestavo keramike $NaNbO_3$, smo pripravili serijo vzorcev s povprečno velikostjo zrn med 0,15 μm in 50 μm. Pri zmanjšanju velikosti zrn s 50 μm na 0,62 μm smo opazili znižanje temperature premene *P*→*R* za okoli 35 °C, medtem ko smo v keramiki z 0,23 μm zrni poleg antiferoelektrične faze *P* opazili tudi feroelektrično fazo *Q*. Z nadaljnjim zmanjšanjem velikosti zrn na 0,19 μm se je delež feroelektrične faze *Q* povečal, delež antiferoelektrične faze *P* pa zmanjšal. V keramiki z velikostjo zrn okoli 0,15 μm smo opazili samo feroelektrično *Q* fazo. Na podlagi dobljenih rezultatov smo ugotovili, da je kritična velikost zrn za fazno premeno *P*→*Q* približno 0,2 μm.

V zadnjem delu smo preiskovali vpliv zunanjega električnega polja na fazne premene keramike $NaNbO_3$. Premena antiferolektrične faze *P* v feroelektrično fazo *Q* je potekla pri električnem polju 8 kV/mm in temperaturi 80 °C, kar smo potrdili z induciranjem feroelektrične histerezne zanke, pojavom deformacije pod vplivom zunanjega električnega polja in XRD analizo. Remanentna polarizacija je znašala 32 μC/cm^2,

piezoelektrični d_{33} koeficient pa 28 pC/N. Inducirana feroelektrična faza Q je ostala stabilna tudi po odstranitvi električnega polja in znižanju temperature, kar nakazuje ireverzibilnost premene $P \rightarrow Q$.

Abbreviations

AFE	antiferroelectric
DSC	differential scanning calorimetry
FE	ferroelectric
FE-SEM	field-emission scanning electron microscopy
KEMS	Knudsen effusion mass spectrometry
LVDT	linear variable differential transformer
PE	paraelectric
RT	room temperature
SG	space group
TE	thermal etching
XRD	X-ray diffraction

Symbols

a	radius of the particle
A_G	area of the grain
CTE	linear coefficient of thermal expansion
d_{BET}	BET equivalent particle diameter
d_{10}, d_{50}, d_{90}	particle sizes reached by 10 %, 50 %, and 90 % of the particles; obtained from the area particle size distributions
d_{33}	piezoelectric coefficient (field and strain along the polar axis)
D_{GB}, D_L, D_S	diffusion coefficients for grain boundary, lattice and surface diffusion
D_e^{BET}	grain size, as estimated from the BET analysis
D_e^{FR}	grain size, as estimated from the fracture surfaces
D_m^{TE}	mean grain diameter, as determined from the thermally etched surface
e_m	average maximum (upper limit) microstrain
E	electric field
E_F	critical electric field inducing the ferroelectric state in the antiferroelectric
E_S	surface free energy
F_b	driving force for the grain-boundary migration
F_p	inhibiting force of the pore against the grain-boundary movement
G	grain diameter
H	term, that collects material and geometric parameters of the powder system
K_p	planar electromechanical coupling factor
K_t	thickness electromechanical coupling factor
l_T	dimension of the sample at the selected temperature
l_{RT}	initial dimension of the sample at RT
$\Delta l/l$	relative (physical) shrinkage
$(\Delta l/l)_{\text{tech.}}$	technical shrinkage
m_A	mass of the atom
M_b	grain-boundary mobility
M_p	pore mobility
n, m	numerical exponents, that depend on the mechanism of sintering
N	number of pores per unit grain-boundary area
p_0	vapour pressure over a flat surface
p_1	vapour pressure over a curved surface
P	dielectric polarization
P_v	porosity
Q_{GB}, Q_L, Q_S	activation energies for grain-boundary, lattice and surface diffusion
r	radius of curvature at the surface

r_p	pore radius
r_1, r_2	principal radii of curvature
R	universal gas constant
$RMSS$	root mean square strain
S_0	initial specific surface area
S_M	specific surface area
ΔS	change of the specific surface area
t	time
T	temperature
T_c	ferroelectric Curie temperature
T_H^S	homologous (or relative) sintering temperature
$tan\delta$	dielectric losses
v_b	grain-boundary velocity
v_p	pore velocity
V_m	molar volume
x	neck radius
γ	specific surface-area reduction exponent
γ_{GB}	specific grain-boundary energy
γ_{SV}	specific surface energy of the particles
δ_S, δ_{GB}	grain-boundary width (thickness for surface and grain boundary diffusion)
ε_0	dielectric permittivity of vacuum
ε_r	relative dielectric permittivity
ε^*	complex dielectric permittivity
ε'	real part of the complex dielectric permittivity
ε''	imaginary part of the complex dielectric permittivity
η	viscosity
ρ_{abs}^t	absolute theoretical density
ρ_{rel}^{GR}	relative green density
ρ_{rel}	relative density
χ_e	electric susceptibility
ψ_A/ψ_V	particle shape factor ratio
Ω	atomic volume

1 Introduction

The Introduction chapter is divided into three parts in order to provide an overview of the topics of this thesis. The first section covers the basic definitions of dielectric, piezoelectric, ferroelectric and antiferroelectric materials, while the second section is focused on the sintering process of ceramic materials. The last section introduces the antiferroelectric material sodium niobate, which is the material investigated in this work.

1.1 General Overview of Polar Oxides

1.1.1 Dielectric, Piezoelectric, and Ferroelectric Materials

A dielectric is an electrically insulating material that can be polarized by an applied external electric field. In a pure dielectric material the dielectric polarization (P) disappears once the electric field (E) is removed and the relationship is linear:

$$P = \varepsilon_0 \chi_e E \tag{1.1}$$

where ε_0 is the dielectric permittivity of vacuum and χ_e is the dielectric susceptibility. The latter is a measure of how easily the material is polarized in response to the electric field, and is related to the relative dielectric permittivity (ε_r) by:

$$\chi_e = \varepsilon_r - 1 \tag{1.2}$$

It is important to note that the equations above are only valid for small electric fields. The relative permittivity characterizes a material's ability to store charge. If an alternating voltage is applied, the charge stored in a dielectric has both real (in-phase; ε') and imaginary (out-of-phase; ε'') components, and thus the relative permittivity can be expressed in a complex form:

$$\varepsilon^* = \varepsilon' + i\varepsilon'' \tag{1.3}$$

The dielectric losses are usually expressed by the loss tangent ($\tan\delta$), which is the ratio of the out-of-phase component to the in-phase component (Waser et al., 2005):

$$\tan\delta = \frac{\varepsilon''}{\varepsilon'} \tag{1.4}$$

In some materials the electric charge is developed by applying an external mechanical stress (direct piezoelectric effect), while the application of an external electric field causes an elastic strain (inverse piezoelectric effect). The coupling between the mechanical and electrical energies is, in both cases, linear and the proportionality constant is the piezoelectric constant. It was found that the piezoelectric effect occurs in 20 out of the 32 crystal classes that do not possess a centre of symmetry and are therefore referred to as non-centrosymmetric. Among these 20 crystal classes, there are 10 that spontaneously

develop a change of polarization as a result of a temperature change. These are pyroelectrics.

Some of the pyroelectric materials possess another significant property, i.e., their dipoles can be reversed by the application of an external electric field. These materials are ferroelectrics. Since the origin of ferroelectric properties lies in the crystal structure, they are categorized by their unit-cell structure: the tungsten-bronze group, the perovskite or the oxygen octahedral group, the pyrochlore group, and the bismuth-layer structure group. The perovskite group with the ABO_3 unit cell is the most important and most widely used group (Jaffe et al., 1971). $BaTiO_3$ is its prototype representative (Kay and Vousden, 1949). Above 130 °C the material is cubic, the Ti^{4+} ion is positioned in the centre of the unit cell and there is no dipole (**Figure 1.1**).

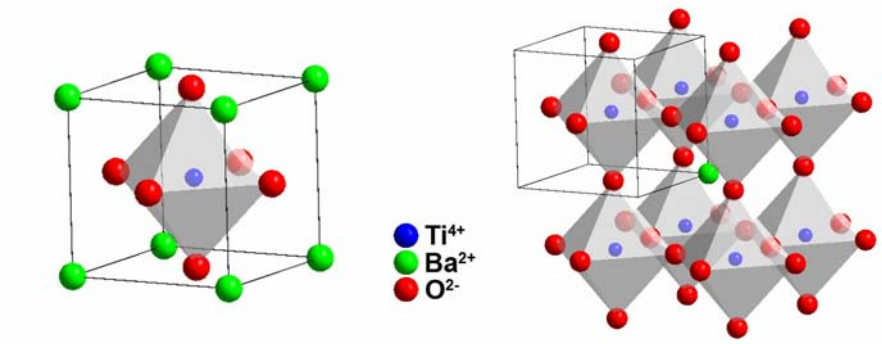

Figure 1.1: Schematic representation of the cubic $BaTiO_3$ unit cell (left) and the network of the oxygen octahedra (right) (after (Kay and Vousden, 1949)).

If the temperature is decreased to below 130 °C a tetragonal lattice distortion occurs, which results in the appearance of the spontaneous polarization. The temperature at which a ferroelectric material undergoes a structural phase transition to a state where the spontaneous polarization vanishes is defined as the ferroelectric Curie point T_c. Upon further cooling $BaTiO_3$ undergoes further phase transitions to the orthorhombic phase at 0 °C and to the rhombohedral phase at -90 °C. Both low-temperature phases are non-centrosymmetric and ferroelectric. These structural changes are observed as changes in the dielectric permittivity, as shown in **Figure 1.2**. In general, the dielectric permittivity and the piezoelectric coefficients are the highest at the Curie point (Jaffe et al., 1971).

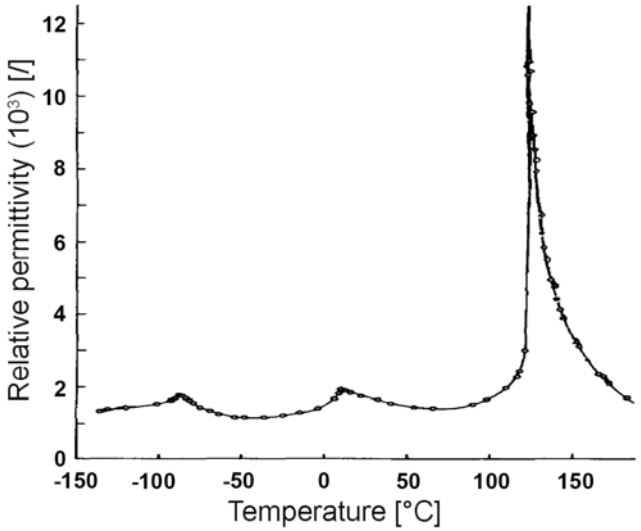

Figure 1.2: Temperature dependence of the relative permittivity of $BaTiO_3$ ceramics (average grain size 53 µm, measured at 1 kHz; after (Kinoshita and Yamaji, 1976)).

The unique properties of ferroelectrics make them suitable for several applications, such as capacitors (due to their high dielectric coefficients over a wide temperature and frequency range), sensors, actuators, and transducers (due to their large piezoelectric effect), temperature sensors (due to their high pyroelectric coefficient), memory applications (due to the switchability of the spontaneous polarization), and many others (Uchino, 2000).

1.1.2 Antiferroelectric Materials

Antiferroelectrics exhibit no macroscopic polarization, despite the fact that switchable dipole moments are present in the crystal structure. This behaviour is the result of an antiparallel alignment of the dipoles, which leads to a net zero polarization, the centre of symmetry in the unit cell, and a lack of piezoelectricity (Kittel, 1951). $PbZrO_3$ is a prototype representative (**Figure 1.3**).

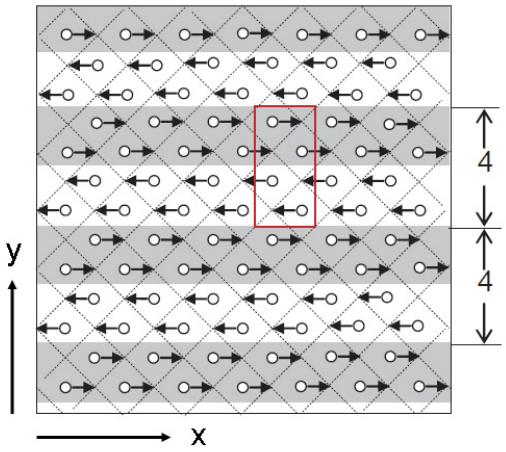

Figure 1.3: Schematic model of the antiferroelectric $PbZrO_3$ structure showing the antiparallel arrangement of the dipoles (Sawaguchi et al., 1951, Tan et al., 2011). The red box marks the orthorhombic unit cell.

The antiparallel arrangement of the dipoles in antiferroelectric materials is the origin of

their unique electrical properties. In many cases a ferroelectric phase with a comparable free energy to the antiferroelectric phase exists and it can be induced by the application of an external electric field of sufficient magnitude. The dependence of the polarization on the electric field in dielectrics, ferroelectric, and antiferroelectrics is represented in **Figure 1.4**. Dielectric materials show a linear behaviour, while in ferroelectrics we can observe typical hysteresis loops. The response of the antiferroelectrics is linear until a threshold electric field (E_F) is reached and a ferroelectric loop is induced. This transition is reversible since the ferroelectric state disappears upon removal of the electric field and the material returns to its antiferroelectric state.

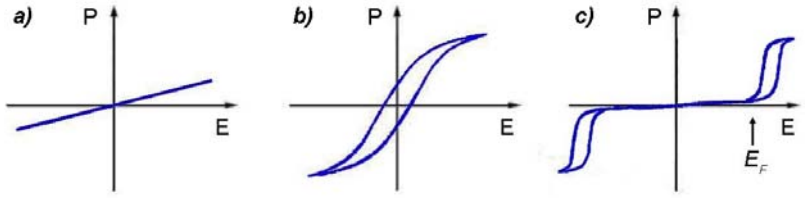

Figure 1.4: Schematic representation of the polarization versus applied electric field in dielectrics (a), ferroelectrics (b), and antiferroelectrics (c). The threshold electric field for the antiferroelectric-ferroelectric phase transition is marked with E_F.

It is important to note that the temperature has a strong influence on the threshold electric field. Sawaguchi and Kittaka found a linear drop in the magnitude of the threshold electric field in $PbZrO_3$ when they approached the Curie temperature at 230 °C (**Figure 1.5**) (Sawaguchi and Kittaka, 1952). This also explains why double hysteresis loops in $PbZrO_3$ were only observed slightly below the Curie temperature. A linear extrapolation of the threshold electric field to room temperature reveals that an electric field of about 360 kV/cm would be needed to induce the double hysteresis loop in $PbZrO_3$ at room temperature – a value that far exceeds the dielectric breakdown strength of conventional $PbZrO_3$ ceramics.

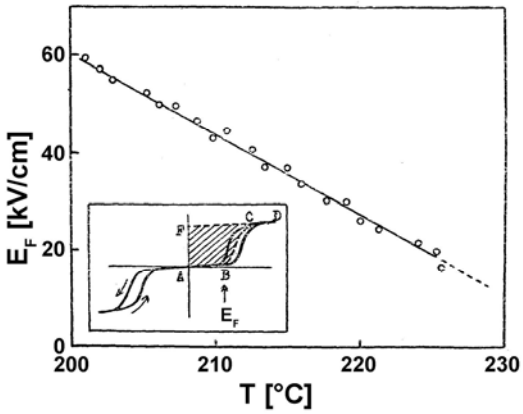

Figure 1.5: Temperature dependence of the threshold electric field for the antiferroelectric-ferroelectric phase transition in $PbZrO_3$. The inset shows the definition of the threshold electric field (Sawaguchi and Kittaka, 1952).

1.2 Sintering of Ceramic Materials

1.2.1 Solid-State Sintering Fundamentals

Sintering is a processing technique for consolidating powder compacts using thermal energy and is widely used to fabricate bulk ceramic components and powder metallurgy parts. It can be described as a thermodynamic process in which the system tends to minimize its free energy. The main driving force for sintering is the reduction of the surface free energy E_S of an ensemble of particles:

$$E_S = \frac{3\gamma_{SV} V_m}{a} \tag{1.5}$$

where γ_{SV} is the specific surface energy of the particles, V_m is the molar volume and a is the particle radius. Since small particles have high surface areas and more energy per unit volume, the sintering process should be faster than with large particles. Therefore, much of ceramic technology is based on the use of fine-particle materials. In addition to the particle curvature, further contributions to the driving force for sintering include the application of an external pressure or a chemical reaction (Rahaman, 2003).

Depending on the changes in the grain size and shape, and in the pore size and shape, and related densification kinetics, the sintering process is divided into three overlapping stages (**Figure 1.6**). The as-formed powder compact consists of individual particles and ≈ 25–60 vol. % porosity. During the initial sintering stage the surface roughness of the particles decreases and the particles are connected with "necks". A porous network of bonded particles with a relative density of approximately 70 % is obtained.

During the intermediate stage the densification rate increases – on the macroscopic scale this is observed as the rapid shrinkage. The pores gradually diminish, the connections between them disappear and the "closed porosity" state is obtained. This usually happens at relative densities between 92 % and 95 %. In the final sintering stage the densification rate dramatically decreases. The isolated pores may shrink and disappear or merge, and thus grow. Grain growth occurs and usually the pores, which are captured on the grain boundaries, impede this process. If the grain-boundary mobility is high enough, the grain boundaries can detach and the pores become isolated within the grains. In such a situation the material transport via grain boundaries is hindered and the atoms diffuse from the grain boundaries towards the isolated pores through the lattice. In addition, rapid (abnormal) grain growth occurs, resulting in an increase of the diffusion paths between the grain boundaries and the pores. All these effects critically impede the material transport towards the entrapped pores, which cannot shrink anymore and so the densification process is stopped (Kang, 2005).

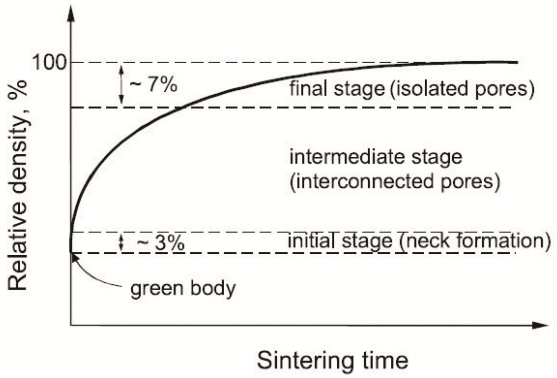

Figure 1.6: The densification curve of a powder compact and the three sintering stages (Kang, 2005).

As sintering is the interplay of densification and grain growth it is convenient to track the process using microstructure-development trajectories, also referred to as grain-size/density diagrams. For many single-oxides such a trajectory is an exponential function, which describes a rapid densification and a negligible grain growth during the intermediate sintering stage and a considerable grain growth once the critical density is reached. Such an example is presented in **Figure 1.7** for the conventional sintering of pure and doped Al_2O_3 (Wang and Raj, 1990), and similar trajectories were also reported for the sintering of nanosized ZrO_2 (Srdić et al., 2000), $BaTiO_3$ (Polotai et al., 2005) and others. Kanters et al. performed a simulation of the microstructure-development trajectories for initial particle sizes between 10 nm and 250 nm assuming different densification and grain-growth mechanisms (Kanters et al., 2000). In all cases the observed trajectories were flat at low densities while grain growth was observed only in the last 5 % of densification, just before reaching the final density. However, coarsening during the initial sintering stage was observed in the case of agglomerated starting powders, which limited the sintering density and therefore changed the shape of the microstructure-development trajectory (Lange, 1984).

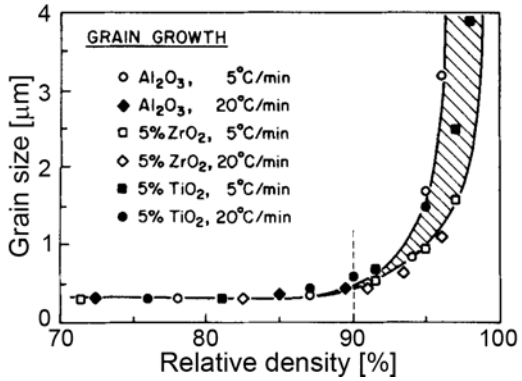

Figure 1.7: Microstructure-development trajectory for the sintering of pure and doped Al_2O_3 (Wang and Raj, 1990). The dashed vertical line marks the critical density for significant grain growth.

The sintering temperature is among the most important sintering parameters, and it mostly depends on the material and the particle size. In order to compare the sintering processes of different materials, the homologous sintering temperature T_H^S (or relative sintering temperature), which is the ratio between the absolute sintering temperature and the absolute melting temperature, has been introduced. The sintering of most materials occurs at homologous temperatures of approximately 0.5 and 0.8; however, it was

reported that materials with a high chemical stability require higher homologous sintering temperatures (Bron, 1964).

1.2.2 Material Transport Mechanisms

During the sintering process individual particles form contacts through necks, which upon further growth create grain boundaries, i.e., solid-solid interfaces, and the latter replace the initial solid-vapour interfaces. Such processes require material transport across the microstructure. The three main material transport mechanisms are lattice diffusion, grain-boundary diffusion, and surface diffusion. In addition, material transport may occur via evaporation/condensation or viscous flow; however, the latter is mainly activated in glass. The material transport mechanisms are schematically presented in **Figure 1.8**. While all promote neck growth, only some contribute to densification, since they transfer the mass from the particle interior, and are therefore referred to as the densifying mechanisms. These are the lattice diffusion from the grain boundary to the neck, grain-boundary diffusion and viscous flow (1, 2, and 3 in **Figure 1.8**). In analogy, surface diffusion, lattice diffusion from the surface to the neck and evaporation/condensation (4, 5, and 6 in **Figure 1.8**) are referred to as the non-densifying mechanisms (Kingery et al., 1976).

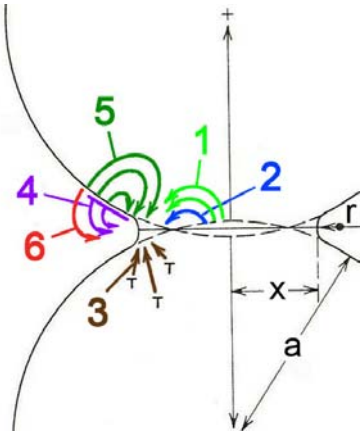

Figure 1.8: Material transport mechanisms during solid-state sintering: lattice diffusion from the grain boundary (1) and from the surface (5) to the neck, grain-boundary diffusion (2), viscous flow (3), surface diffusion (4), and evaporation/condensation (6) (*a* is the radius of the particle, *x* is the radius of the neck, and *r* is the radius of the curvature at the surface). (Kingery et al., 1976)

The path of the material transport via diffusion is determined by the different types of defects that are present in polycrystalline materials. The free surface of crystalline solids contains several defects and the main mechanism of surface diffusion is typically the migration of vacancies and the movement of adatoms, which is confined to the thin surface layer of about 0.5–1.0 nm. Since the atoms at the surface have fewer neighbours, the activation energy for this mass-transport mechanism (Q_S) is expected to be the lowest.

The grain boundaries are the regions of lattice mismatch and disorder between adjacent grains with widths of about 0.5–1.0 nm. They are formed during the sintering process and allow a mass flow with the activation energy (Q_{GB}), which should be higher than the one for surface diffusion. It is important to note that the fraction of the solid occupied by grain boundaries increases with decreasing grain size, so the contribution of the grain-boundary diffusion is dependent on the grain size.

The lattice diffusion involves the motion of point defects, either vacancies or interstitials, from the neck surface or grain-boundary area through the lattice, and the flow of atoms in the opposite direction. An atom can only jump to a vacancy, which is located

on an adjacent lattice site; however, the vacancy can jump to any of the nearest-neighbouring sites. The diffusion coefficients of the two species are not equal; however, the flux of vacancies should be compensated by the opposite and equal flux of atoms. The lattice diffusion has got the highest activation energy (Q_L) and is therefore active at higher temperatures; however, it is often not the dominant mass-transport mechanism during sintering, especially for small particle sizes where the interfacial diffusion processes (surface and grain-boundary diffusion) are more active (Rahaman, 2003).

Although the above-described relationships between the activation energies of different diffusion mechanisms, i.e., $Q_L > Q_{GB} > Q_S$, have been reported in most sintering text books (German, 1996, Kang, 2005, Kingery et al., 1976, Rahaman, 2003), they need to be considered with care. Most of the experimental studies that report the measured values of different activation energies, revealed higher values for the activation energies for the surface diffusion, as compared to the activation energies for the grain-boundary diffusion. The values of the activation energies for different diffusional mechanisms in some simple materials are collected in **Table 1.1** (German, 1996). Although the activation energies for grain-boundary diffusion are the lowest, this mechanism will not be activated first, since during the early stage of sintering the amount of grain boundaries, which are the diffusion paths in this case, is very low. Therefore, it is more likely that the surface diffusion is indeed activated at lower temperatures.

Table 1.1: Activation energies for diffusional material transport mechanisms in different materials (German, 1996).

Material	Q_S [kJ/mol]	Q_{GB} [kJ/mol]	Q_L [kJ/mol]
Al_2O_3	536	477	636
MgO	460	230	460
UO_2	452	293	452
SiC	696	557	696
Cu	205	107	213

In addition to the diffusion mechanisms described above, mass transport during sintering can also occur via evaporation/condensation, as schematically presented in **Figure 1.9**. The vapour pressure over a positive curvature at the surface of the particle is larger than above the neck with a negative radius of curvature. The pressure difference promotes the transfer of the material from the particle surface into the neck area. The vapour pressure over a curved surface is described by the Kelvin equation:

$$\ln\left(\frac{p_1}{p_0}\right) = \frac{\gamma_{SV} V_m}{RT}\left(\frac{1}{r_1} + \frac{1}{r_2}\right) \tag{1.6}$$

where p_1 and p_0 are the vapour pressures over a curved and over a flat surface, respectively, R is the universal gas constant, T is the temperature, and r_1 and r_2 are the principal radii of the curvature. It is important to note that the vapour pressure, and thus material transport via evaporation/condensation, exponentially increases with the increasing curvature of the particles, i.e., a decreasing particle size (Kingery et al., 1976).

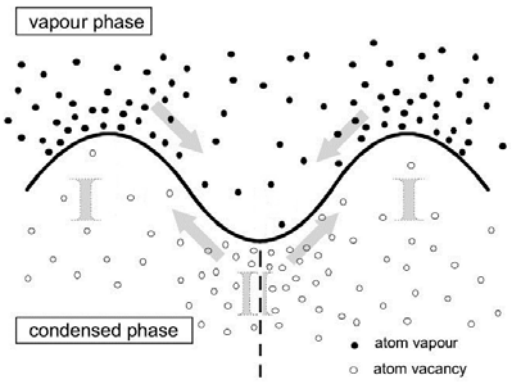

Figure 1.9: Distribution of vacancies and atoms near a curved surface. (Kang, 2005)

1.2.3 Analytical Sintering Models

Researchers have attempted to develop various theoretical models to predict the sintering behaviour of powder compacts. However, the complexity of the process soon became evident and therefore up to now no general sintering theory exists. The authors focused on individual sintering stages, as described in Section 1.2.1. They are distinguished by their geometrical structures, e.g., grain size and shape, porosity network, and therefore analytical models, assuming simple and idealized geometries, could be established for each of the three sintering stages. The mass-transport equations could be analytically solved and provided equations for the sintering kinetics. The disadvantages of such analytical models are the necessary simplifications, such as the assumed uniform packing, monosized spherical particles, occurrence of a single mass-transport mechanism and others. The simplifications often hinder quantitative predictions of the sintering behaviour of real powder systems; nevertheless, the models are useful for a qualitative understanding of the complex sintering process. The following sections describe some basic analytical models for the three sintering stages.

1.2.3.1 Initial Sintering Stage

The initial sintering stage was described using a system of two spherical particles of the same size, schematically presented in **Figure 1.10** (Frenkel, 1945, Kuczynski, 1949a). The progress of the sintering process is tracked by the neck growth, i.e., the *x/a* ratio, where *x* is the radius of the neck. The mass flow, which occurs by any of the mechanisms described in Section 1.2.2, is driven by the curvature gradient and the deposited or removed atoms change the neck size and shape. In **Figure 1.10a** the distance between the particles remains constant during sintering, but the neck size increases with an increase of the sintering time. Such a situation occurs when the non-densifying material transport mechanisms, such as surface diffusion, lattice diffusion from the surface to the neck, and evaporation/condensation, are active (numbers 4, 5, and 6 in **Figure 1.8**). On the other hand, grain-boundary diffusion, lattice diffusion from the grain boundary to the neck, and viscous flow (numbers 1, 2, and 3 in **Figure 1.8**) result in the neck growth as well as in the densification, and are therefore referred to as the densifying mechanisms (**Figure 1.10**). Although the non-densifying mechanisms do not result in macroscopic shrinkage, they need to be taken into account since they reduce the curvature of the neck, i.e., the driving force for sintering, and therefore reduce the contribution of the densifying mechanism.

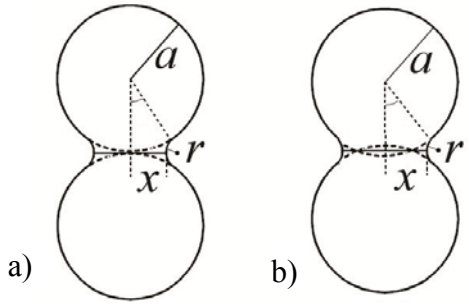

Figure 1.10: Geometrical models for the initial sintering stage of two spherical particles: a) without shrinkage, b) with shrinkage (*a* is the radius of the particle, *x* is the radius of the neck, and *r* is the radius of the curvature at the surface). (Kuczynski, 1949a)

The equations for the neck growth and the shrinkage during the initial stage of isothermal sintering were derived by Kuczynski (Kuczynski, 1949a), Kingery and Berg (Kingery and Berg, 1955), Coble (Coble, 1958), and Johnson and Cutler (Johnson and Cutler, 1963), and are expressed in a general form as follows:

$$\left(\frac{x}{a}\right)^n = \frac{H}{a^m} t \tag{1.7}$$

$$\left(\frac{\Delta l}{l}\right)^{n/2} = \frac{H}{2^n a^m} t \tag{1.8}$$

where n and m are numerical exponents that depend on the mechanism of sintering, t is the sintering time, H is a term that includes the material and geometric constants of the powder system, and the $\Delta l/l$ is the shrinkage (compact length change divided by the initial length). **Table 1.2** collects the estimated values for n, m, and H for different material-transport mechanisms during the initial sintering stage (Coblenz et al., 1980).

Table 1.2: Estimated values for the numerical exponents n and m and the numerical constant H from **Equation 1.7** and **1.8** for different sintering mechanisms during the initial stage of sintering (Coblenz et al., 1980).

Mechanism	n	m	H	Label in **Figure 1.8**
Viscous flow	2	1	$\frac{3\gamma_{SV}}{2\eta}$	3
Evaporation/ condensation	3	2	$\frac{3p_0\gamma_{SV}\Omega}{kT\sqrt{2\pi m_A kT}}$	6
Lattice diffusion from the surface	4	3	$\frac{20D_L\gamma_{SV}\Omega}{kT}$	5
Lattice diffusion from the grain boundary	5	3	$\frac{80\pi D_L\gamma_{SV}\Omega}{kT}$	1
Grain-boundary diffusion	6	4	$\frac{96D_{GB}\delta_{GB}\gamma_{SV}\Omega}{kT}$	2
Surface diffusion	7	4	$\frac{56D_S\delta_S\gamma_{SV}\Omega}{kT}$	4

Symbols: η – viscosity, Ω – atomic volume, m_A – mass of the atom, δ_S, δ_{GB} – thickness for surface and grain-boundary diffusion, D_L, D_{GB}, D_S – diffusion coefficients for lattice, grain-boundary and

surface diffusion.

The simplified models given by **Equation 1.7** and **Table 1.2** give rough approximations of the sintering behaviour up to the neck-size ratio of 0.3. Nevertheless, they illustrate some key processing factors in sintering:

- A small particle size will result in more rapid sintering (the most sensitive mechanisms are surface and grain-boundary diffusion).
- Small changes in the temperature will have a large effect, since the temperature appears in the exponential term in the diffusion equations and directly increases the vapour pressure of the material.
- The sintering rate will increase with increasing sintering time; however, its effect is less important than that of the temperature and the particle size.

In order to validate the analytical models, researchers have normally used two types of experiments: measurements of the neck growth in simple systems (two spheres, a sphere on a plate, two wires etc.) or measurements of the shrinkage in a compacted mass of spherical particles. The models have been proven useful for predicting the material transport mechanisms in different systems, such as glass (Kuczynski, 1949b), NaCl, Cu (Kingery and Berg, 1955), Al_2O_3, Fe_2O_3 (Coble, 1958), B, TiO_2 (German and Munir, 1976), ZnO (Stevanovic et al., 2007) and others, provided that the basic assumption of a single dominant mass-transport mechanism was satisfied. Therefore, it is very important that the analysis of the material transport mechanisms combines different experimental observations, which can support the results obtained from the analytical models.

1.2.3.2 Intermediate Sintering Stage

During the initial sintering stage the particles become connected and the neck size increases. With a further increase of the sintering time the system enters the intermediate sintering stage, where the pores form interconnected channels along three-grain edges and the equal shrinkage of pores in the radial direction is assumed. The analytical description for this stage is given by the channel-pore model proposed by Coble (Coble, 1961).

In the geometrical model the powder system is idealized by considering bcc-packed tetrakaidecahedral grains (note: tetrakaidecahedron is a truncated octahedron), while the complex-shaped pore phase is approximated by connected, continuous cylinders with the axes coinciding with the grain edges. This geometry is schematically presented in **Figure 1.11**. During the intermediate sintering stage the cylindrical pore is assumed to simply shrink and the pore geometry is uniform. The chemical potential is therefore the same everywhere on the pore surface, which disables the operation of the non-densifying mechanisms. Since a viscous flow is not expected in ceramic systems, the only possible material transport mechanisms according to this model are lattice and grain-boundary diffusion.

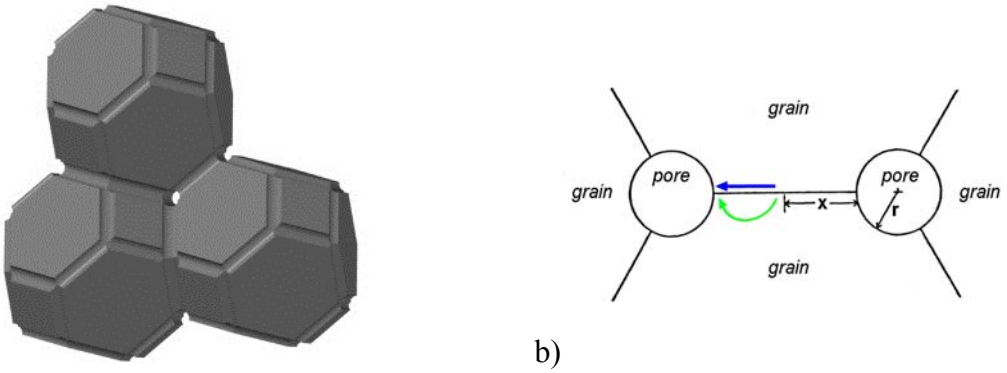

Figure 1.11: a) Schematic representation of the geometrical model for the intermediate sintering stage consisting of tetrakaidecahedral grains and connected continuous cylindrical pores. b) Cross-section of the neck and two cylindrical pores showing the lattice (green arrow) and grain-boundary (blue arrow) diffusion paths (Coble, 1961).

The pores are considered as the vacancy sources and the grain boundaries as the vacancy sinks, while the atoms diffuse towards the cylindrical pores (**Figure 1.11b**). The densification rate $d\rho/dt$ for the case of lattice and grain-boundary diffusion can be expressed with **Equations 1.9** and **1.10**, respectively.

$$\frac{d\rho}{dt} = \frac{336 D_L \gamma_{SV} \Omega}{kTG^3} \tag{1.9}$$

$$\frac{d\rho}{dt} = \frac{854 D_{GB} \delta_{GB} \gamma_{SV} \Omega}{kTG^4} \sqrt{\frac{1}{P_v}} \tag{1.10}$$

Here, G is the grain diameter, and P_v is the porosity. In addition, it should be noted that in reality some grain growth also usually takes place during this stage, and therefore growth equations must be taken into consideration as well.

1.2.3.3 Final Sintering Stage

For the final sintering stage Coble proposed the isolated pore model, where the system is idealized in terms of an array of equal-sized tetrakaidecahedral grains with equal-sized spherical pores at the corners (Coble, 1961). This geometry is schematically presented in **Figure 1.12**.

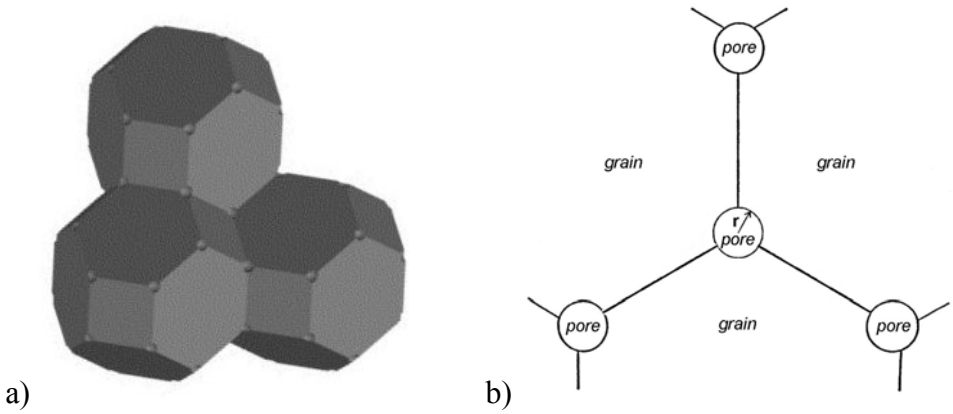

Figure 1.12: a) Schematic representation of the geometrical model for the final sintering stage consisting of tetraidecahedral grains with spherical pores at the corners. b) Cross-section of a spherical pore with the surrounding grains.

Coble suggested the concentric sphere diffusion of atoms towards the pore surface; however, this model does not take into account the grain boundary as the atom source for densification and it predicts a constant material flux towards the surface, irrespective of the pore size. This was corrected by including the effect of the surface area of the pore on the material flux from the grain boundary to the pore. The derivation of the densification rate for lattice and grain-boundary diffusion, considering these effects, was made by Kang and Jung (Kang and Jung, 2004):

$$\frac{d\rho}{dt} = \frac{441 D_L \gamma_{SV} \Omega}{kTG^3} \sqrt[3]{1-\rho} \tag{1.11}$$

$$\frac{d\rho}{dt} = \frac{735 D_{GB} \delta_{GB} \gamma_{SV} \Omega}{kTG^4} \tag{1.12}$$

In the case of Al_2O_3 it was shown that the contribution of grain-boundary diffusion to the densification dominates the lattice diffusion for the fine initial particle sizes (0.8 μm) and vice versa for the coarse particle sizes (4 μm) (Kang and Jung, 2004). A reduction of scale therefore enhances the relative contribution of grain-boundary diffusion over the lattice diffusion.

During the final sintering stage the densification is strongly interrelated with the grain growth in the presence of pores. The process of grain growth will be discussed in Section 1.2.4 With increasing the grain size and the sintering time the densification rate decreases and therefore the understanding and the control of grain-growth processes is very important for achieving high-density ceramics. In addition, in the final sintering stage the atmospheric gas is entrapped within the pores as they are isolated and hence the final densification is strongly affected by the sintering atmosphere. Full densification is thus only possible in the case of rapidly diffusing gases, unless a high external pressure is applied (German, 1996).

1.2.4 Grain Growth

The sintering process is described as a combination of densification and grain growth, which form the final microstructure of the ceramic. The following sections are focused on the process of grain growth in ceramics.

1.2.4.1 Normal Grain Growth

Normal grain growth is the process upon which the average grain size of the material increases continuously during heating, without any change in the grain size distribution. The average increase of the grain size results in a decrease of the grain boundary area and the total boundary energy. This energy change corresponds to about 0.4–2.0 J/g for the change from a 1 μm to a 1 cm grain size (Kingery et al., 1976).

The grain boundary is a region of disorder between two crystallites and the grain growth occurs when atoms diffuse from one side of the grain boundary to a new position on the other side. The driving force for the diffusion is the free-energy difference across the curved grain boundary (**Equation 1.13**) and the result is the movement of the grain boundary towards its centre of curvature (**Figure 1.13a**).

$$\Delta G = \gamma_{GB} V_m \left(\frac{1}{r_1} + \frac{1}{r_2} \right) \tag{1.13}$$

Here, γ_{GB} is the specific grain-boundary energy. If the grain-boundary energy is isotropic,

the balance of the grain-boundary tensions requires that the edges meet at 120°. A hexagon will therefore have straight sides; in polygons with more than six sides the boundaries will be concave; while in polygons with fewer than six sides the boundaries will be convex. Since grain boundaries migrate towards their centre of curvature, the grains with fewer than six sides tend to shrink, while grains with more than six sides tend to grow (**Figure 1.13b**) (Burke, 1989).

a) 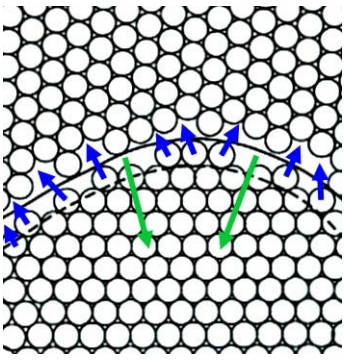

b) 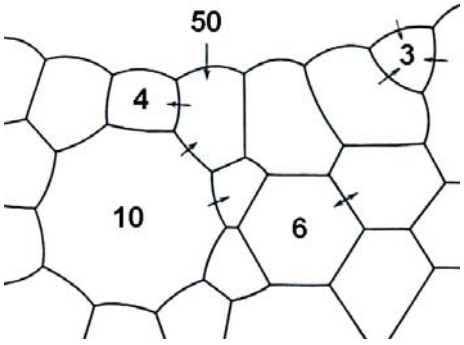

Figure 1.13: a) Diffusion of atoms across a curved grain boundary (blue arrows) and the movement of the grain boundary towards its centre of curvature (green arrows); b) schematic drawing of a polycrystalline ceramic including grains with a different number of sides (black arrows denote the movement of the grain boundary). (Burke, 1989)

One of the first theoretical analyses of normal grain growth was performed by Burke and Turnbull (Burke and Turnbull, 1952). They considered an isolated part of the grain boundary and assumed an isotropic grain-boundary energy. The obtained parabolic grain growth law is written as:

$$G^2 - G_0^2 = Kt \tag{1.14}$$

where G_o is the initial grain size and K is a growth factor that includes the grain-boundary energy, mobility and the geometrical constants, and has the Arrhenius dependence of the temperature.

1.2.4.2 Abnormal Grain Growth

Abnormal grain growth occurs when a small fraction of the grains grow unusually quickly to a large size in a matrix of fine grains, which grow with a slow rate. Many different causes for this abnormal grain growth were identified in different systems; however, this phenomenon is mostly related to specific local conditions, such as an anisotropic grain-boundary energy (Rollett et al., 1989), the preferential segregation of dopants and impurities (Horn and Messing, 1995), second-phase particles or pores, all of which effect the boundary mobility. In addition, the presence of a liquid phase (Bateman et al., 1989) or non-uniform particle/grain size distribution is also often stated as a cause for abnormal grain growth (Rahaman, 2003).

The rapid growth of an abnormal grain is explained by the fact that the number of sides of such large grains is much higher, compared to the smaller grains, and thus also the curvature of each side of the large grain is accordingly larger, resulting in its rapid growth (Rahaman, 2003).

1.2.4.3 Grain Growth in the Presence of Pores

In real systems the grain-boundary mobility is often affected by various factors and therefore deviates from the intrinsic boundary mobility. Porosity is by far the most

common factor affecting the grain-boundary mobility of single-phase systems. Grain growth in porous ceramics is described in a similar way as in the previous chapters as normal and abnormal; however, the interaction of the pores with the grains needs to be taken into account. In general, the normal grain growth is characterized by the pores, remaining at the grain boundaries, while the abnormal grain growth occurs when the boundaries break away from the pores that remain trapped inside the grains.

As sintering proceeds, the density and the grain size increase. At the final sintering stage the pores are present mostly at the triple junctions and at the grain boundaries. The grain boundary, which moves under the influence of its curvature, applies a force on the pore situated at the boundary, resulting in a change of the pore shape (**Figure 1.14**) (Hsueh et al., 1982). Different curvatures of the leading and trailing surfaces of the pore create a chemical-potential difference, which drives the atom flux towards the trailing surface. Material transport occurs via surface diffusion, lattice diffusion or evaporation/condensation. The transport mechanisms are simultaneously operative and the dominant mechanism can vary with the experimental conditions, for example, the contribution of the surface diffusion increases as the pore size decreases (Rahaman, 2003).

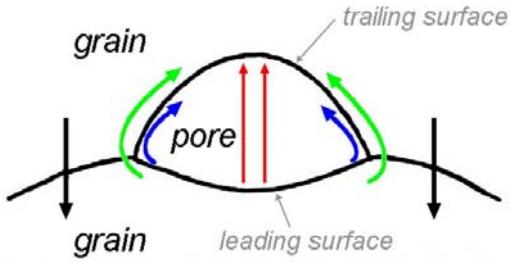

Figure 1.14: Schematic representation of a pore moving with the grain boundary and the possible material transport mechanisms: surface diffusion (blue), lattice diffusion (green), and evaporation/condensation (red). The black arrows show the migration direction. (Rahaman, 2003)

In the above-described case the pore moves together with the grain boundary and inhibits the grain growth. The pore velocity is therefore described as:

$$v_p = M_p F_p \tag{1.15}$$

where M_p is the pore mobility, which depends on the mechanism of the pore migration, and F_p is the inhibiting force of the pore against the boundary movement, which depends on the size of the pore and the boundary energy.

The driving force of the grain-boundary migration, for the case of a system with pores present at the grain boundary, is the difference between the driving force for a pore-less boundary and the inhibition force of the pores against the boundary migration. The grain boundary velocity v_b is thus expressed as (Nichols, 1968):

$$v_b = M_b\left(F_b - NF_p\right) = \frac{M_b}{1 + N\left(\frac{M_b}{M_p}\right)} F_b \tag{1.16}$$

where M_b is the boundary mobility, F_b is the driving force of the grain-boundary migration, and N is the number of pores per unit grain-boundary area. Two extreme cases can be imagined when considering **Equation 1.16**. If the system contains many pores with a low mobility ($NM_b >> M_p$) the grain-boundary migration will be controlled by the

pore mobility. In the second extreme case, where there is a small number of pores with a high mobility ($NM_b << M_p$), the migration of the boundary will be controlled by the intrinsic boundary mobility and the pores will not affect the boundary migration. For any pore-migration mechanism we can also calculate the condition of equal mobility, where the boundary mobility is the same as the pore mobility. Such conditions are schematically represented in **Figure 1.15** (Brook, 1969).

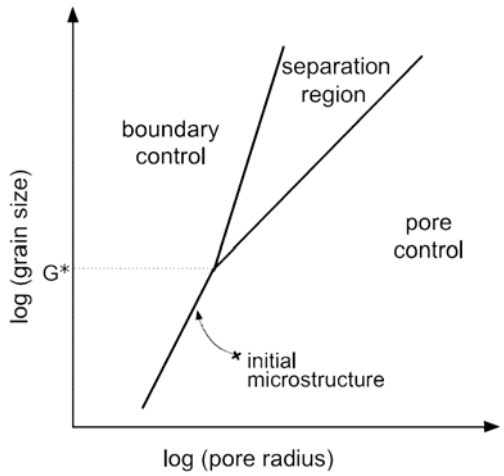

Figure 1.15: Dependence of the type of pore-boundary interaction on the microstructural parameters. G^* corresponds to the minimum grain size for the pore/boundary separation. (Brook, 1969)

When the boundary-migration velocity becomes higher than the pore-migration velocity, the pore/boundary separation will occur. Since such entrapped pores are difficult to eliminate, these separation conditions typically represent the limit of densification in sintering.

1.3 Sodium Niobate ($NaNbO_3$)

Sodium niobate ($NaNbO_3$) was discovered in 1949 (Matthias, 1949) and has ever since claimed the attention of researchers due to its complex structure and unique physical properties. During the first decades after its discovery the majority of the research was focused on the crystal structure and the phase transitions, since $NaNbO_3$ exhibits the largest number of phase transitions among all oxygen perovskites (Lefkowitz et al., 1966, Megaw, 1974, Wood, 1951). The material again gained considerable interest in 1990s due to increased environmental awareness. Namely, $NaNbO_3$ is an end member of several alkaline niobate-based solid solutions, such as $K_{0.5}Na_{0.5}NbO_3$ (Jaffe et al., 1971), $(K_{0.44}Na_{0.52}Li_{0.04})(Nb_{0.86}Ta_{0.10}Sb_{0.04})O_3$ (Saito et al., 2004) and others, which represent an important group of environmentally friendly, lead-free piezoceramics (Rödel et al., 2009). Finally, the recent increase in the use of antiferroelectric materials in energy storage and high-strain actuator applications (Fletcher et al., 1996, Hao et al., 2011, Liu and Dkhil, 2011) has once again increased the interest in $NaNbO_3$, one of the prototype antiferroelectric systems. The following sections review the key processing issues and the properties of $NaNbO_3$.

1.3.1 Processing of $NaNbO_3$ Ceramics

1.3.1.1 Synthesis of $NaNbO_3$ Powders

Egerton and Dillon were among the first to describe the preparation of $NaNbO_3$ powders and ceramics in 1959 (Egerton and Dillon, 1959). The dried sodium carbonate (Na_2CO_3) and niobium pentoxide (Nb_2O_5) were mixed in the proper ratio and 0.1 mol. % excess of the carbonate was added in order to ensure the stoichiometry. The components were ball milled in ethanol and calcined in Pt crucibles at temperatures between 750 °C and 1000 °C for 16 h. The obtained powders were leached several times, filtered, dried and pressed into disks. These disks were subsequently sintered at temperatures between 1050 °C and 1325 °C, which resulted in relative densities of approximately 94–97 %. Later researchers report similar processing conditions, only without the leaching step (Dungan and Golding, 1964, Jimenez et al., 2004, Reznitchenko et al., 2001). Some researchers used the commercially available $NaNbO_3$ powder (Alfa, a Johnson Matthey company) without any reported synthesis details (Darlington and Knight, 1999, Wang et al., 1996).

In order to improve the sintering of $NaNbO_3$, the researchers were striving for powders with finer particle sizes, as obtained by solid-state synthesis. Therefore, new synthesis methods were utilized to produce $NaNbO_3$ nanopowders. Nobre et al. used the Pechini route and subsequent calcination of the precursor at 700 °C for 5 h to obtain particle sizes of approximately 60 nm (Nobre et al., 1996). Lanfredi et al. prepared 85-nm-sized $NaNbO_3$ particles by calcining the precursor, obtained from the solution of an niobium-oxalato complex, sodium nitrate, oxalic acid, and ammonium hydroxide (Lanfredi et al., 2000). In both cases, dense $NaNbO_3$ ceramics were obtained after sintering at lower temperatures than usually needed for the solid-state synthesized powder, which was connected to the small particle size and to a high concentration of defects, such as oxygen vacancies. The latter were presumably created due to the incomplete oxidation of organic precursors. In 2005, Pithan et al. introduced the microemulsion-mediated hydrolytic decomposition of a mixed-alkoxide solution, followed by the Soxhlet extraction, and subsequent calcining at 400 °C to prepare particles of a few 10 nm in size (Pithan et al., 2005). Despite the reported successes in obtaining nanosized powders it should be noted that solution-based chemical routes also suffer various deficiencies, such as complicated processing, a small product yield, difficult upscaling, and sometimes the incomplete removal of residual carbon.

An alternative approach was introduced by Rojac et al., who prepared $NaNbO_3$ nanopowder by mechanochemical synthesis (Rojac et al., 2005). After 40 h of high-energy milling of Na_2CO_3 and Nb_2O_5 in a planetary mill, the product consisted of agglomerates of 100–300 nm in size, while the crystallites were in the range 10–20 nm. The process, however, introduced impurities into the powder due to wear of the ZrO_2 milling vial and balls.

1.3.1.2 Sintering of $NaNbO_3$

The sintering step is one of the key issues in the processing of $NaNbO_3$, and also alkaline niobates in general. The reported problems are mostly related to difficulties in obtaining a high density, deviations from the stoichiometry due to volatilization of the alkali component at high temperatures and, subsequently, the formation of secondary phases, and difficulties in obtaining a fine-grained microstructure (Egerton and Dillon, 1959, Jenko et al., 2005). In order to overcome these problems, many solutions have been introduced: hot pressing (Jaeger and Egerton, 1962), spark-plasma sintering (Wada et al., 2003), or the use of ultra-fine starting materials (Lanfredi et al., 2000, Nobre et al., 1996).

Nevertheless, conventional sintering techniques still represent the most cost-efficient route for the production of alkaline niobate ceramics.

Despite over 60 years of investigation, not much is known about the basic mechanisms that take place at the microscopic level during the sintering of alkaline niobates, for example, material-transport mechanisms, grain-boundary and pore migration or grain growth mechanisms. Nobre et al. (Nobre et al., 1996) and Lanfredi et al. (Lanfredi et al., 2000) measured the shrinkage curves of $NaNbO_3$ compacts prepared from nanosized powders and observed different densification behaviours A detailed microscopic study of pure and Li or $BaTiO_3$ doped $(K_{0.5}Na_{0.5})NbO_3$ ceramics was performed by Ahn et al. (Ahn et al., 2009). They identified three sintering stages and related the observed rapid grain growth to the presence of a liquid phase. The effect of the alkaline and niobium excess on the sintering behaviour of $(K_{0.5}Na_{0.5})NbO_3$ was studied by Acker et al. (Acker et al., 2010). A strong dependence of the final microstructure on the composition was observed, due to the presence of the liquid phase. The densification and grain growth were proposed to be controlled by the secondary-phase formation and different types of diffusion, as assumed from the observed differences in the sintering behaviour and the microstructures. However, many results remain without a proper explanation and the mechanisms that are active during sintering remain unclear.

1.3.2 Polymorphism of $NaNbO_3$

Upon discovery the room-temperature phase of $NaNbO_3$ was reported to be ferroelectric (Matthias, 1949); however, it was soon found to be actually macroscopically non-polar and antiferroelectric (Cross and Nicholson, 1955, Vousden, 1951). More detailed structural analyses and studies of the phase transitions by XRD were performed by the Cambridge Crystallographic Laboratory between 1966 and 1973 (Ahtee et al., 1972, Darlington and Megaw, 1973, Glazer and Megaw, 1972, Glazer and Megaw, 1973, Lefkowitz et al., 1966, Sakowski-Cowley et al., 1969) and the work was summarized in the paper by Megaw in 1974, which became the main reference for later studies (Megaw, 1974). It should be noted that these studies were performed on $NaNbO_3$ single crystals.

1.3.2.1 Room-Temperature Structure

At room temperature (RT), $NaNbO_3$ is usually reported to possess an orthorhombic unit cell with the space group *Pbcm* (SG No. 57) – this polymorph is also referred to as the *P* phase and belongs to the centrosymmetric *mmm* point group. The structure, which has 8 perovskite formulas per unit cell, consists of a network of corner-shared NbO_6 octahedra with Na^+ ions occupying the interstices (**Figure 1.16**). The octahedra are slightly tilted, and the Nb^{5+} ions are displaced along the *a* axis. The Nb^{5+} displacements are antiparallel in successive pairs of layers, which is the origin of the antiferroelectric characteristics. The dipole moments are completely cancelled within the unit cell and thus the phase is macroscopically non-polar (Sakowski-Cowley et al., 1969).

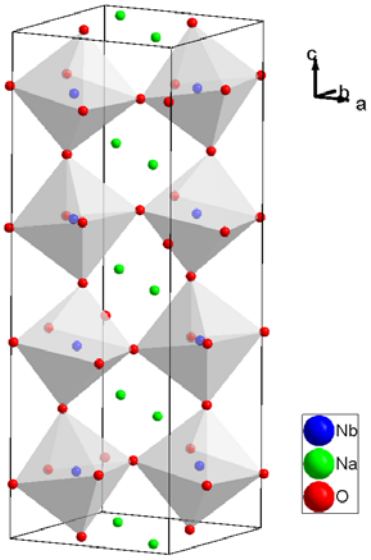

Figure 1.16: The unit cell of the antiferroelectric RT *P* phase of $NaNbO_3$ (after (Sakowski-Cowley et al., 1969)).

1.3.2.2 Temperature-Induced Phase Transitions

Upon heating $NaNbO_3$ undergoes a complex sequence of displacive phase transitions (Megaw, 1974) until it finally reaches the melting point around 1412 °C. The differences between the phases can be described in terms of two factors:

The displacement of the Nb^{5+} cations from the centre of the oxygen octahedra in three directions, which originates in the interactions of the strong Nb–O bonds holding the octahedra together and the O–O repulsion in its edges. This off-centring creates the dipoles.

Tilting of the oxygen octahedra, which behave as rigid bodies and remain linked to each other through the shared corners. The tilting is prohibited if the cation is large enough to fill the 12-coordinated cavity of the ideal perovskite structure, as is the K in $KNbO_3$, while the Na in $NaNbO_3$ is small enough to allow tilting.

The low-temperature rhombohedral *N* phase has the lowest symmetry (space group *F3c*), the Nb^{5+} is displaced in three directions and three tilt components exist. Upon heating the displacement and the tilting components disappear and the material undergoes a sequence of phase transitions between the following phases: orthorhombic *P* phase (*Pbcm*, -100 °C to 360 °C), orthorhombic *R* phase (*Pnmm*, 360–480 °C), orthorhombic *S* phase (*Pnmm*, 480–520 °C), orthorhombic *T(1)* phase (*Ccmm*, 520–575 °C), tetragonal *T(2)* phase (*F4/mmb*, 575–640°C), and cubic *U* phase (*Pm3m*, above 640 °C). Note that the Nb^{5+} displacement disappears above 480 °C and the material transforms into the paraelectric state – this temperature is considered as the Curie temperature of $NaNbO_3$ (Ahtee et al., 1972).

Besides the generally recognized sequence of $NaNbO_3$ phase transitions presented above, the Raman spectroscopy of commercially available $NaNbO_3$ powder revealed another anomaly in the vicinity of 190 °C, which was related to a new phase transition, resulting in the formation of a new antiferroelectric orthorhombic *P'* phase, stable up to 376 °C (Wang et al., 1996). Unfortunately, no details about the powder preparation were given. Similarly, a weak anomaly was detected in the temperature dependence of the dielectric permittivity of single crystals in the vicinity of 150 °C and associated with a new phase transition (Raevskii et al., 2000). Indeed, this anomaly could be found in some

previous papers; however, it received no interpretation (Konieczny, 1999, Molak, 1987). Although this anomaly was reported by two authors, using different measuring techniques, it was not widely recognized as another phase transition of $NaNbO_3$, since most of the later papers keep referring to the sequence of phase transitions listed by Megaw (Megaw, 1974). Nevertheless, some took this suggested new transition into consideration (Bouziane et al., 2003, Raevski and Prosandeev, 2002), while in some cases this anomaly could be observed in the dielectric measurement curves, but did not receive any interpretation (Castro et al., 2004, Wada et al., 2003). A detailed re-examination of $NaNbO_3$ single crystals and sintered ceramics was performed by Raman spectroscopy, XRD, and dielectric measurements. The authors proposed the following sequence: monoclinic phase P_m between -23 °C and 137 °C, an incommensurate phase exhibiting an invar effect between 137 °C and 187 °C, and an orthorhombic phase P_o between 187 °C and 360 °C (Yuzyuk et al., 2005). As evident from large inconsistencies between different studies the origin and the nature of the anomaly in the vicinity of 150–190 °C remain unclear.

1.3.2.3 Electric-Field-Induced Phase Transitions

In 1955, Cross and Nicholson demonstrated the existence of another room-temperature polymorph, which appeared when the $NaNbO_3$ was subjected to a large external electric field (Cross and Nicholson, 1955). Interestingly, this new phase, also referred to as the *Q* phase, was found to be ferroelectric. In 1964, Dungan and Golding reported that the phase was induced by the application of electric fields above 50 kV/cm and temperatures above 100–150 °C. Once induced, the ferroelectric phase remained stable for (at least) several years, as observed from the aging studies carried out at RT without any electric field (Dungan and Golding, 1964). However, the transitions of the *Q* phase upon heating are still not clearly defined and different transition temperatures, between 270 °C and 333 °C, can be found in the literature (Dungan and Golding, 1964, Konieczny, 1999, Shiratori et al., 2007, Wada et al., 2003).

The crystal structure of the *Q* phase was investigated in detail only in 1993 by Shuvaeva et al. (Shuvaeva et al., 1993). The structure is orthorhombic with the space group $P2_1ma$ (SG No. 26; centrosymmetric *mm2* point group) and the cell dimensions are identical to the *P* phase, except that the cell parameter *c* is half the original value. Nb^{5+} atoms are displaced from the centres of the oxygen octahedra in the (001) planes towards the midpoints of their edges. The important difference from the antiferroelectric *P* phase is that in the *Q* phase all the x-components of the dipoles are parallel in successive pairs of layers, resulting in the polar order and ferroelectricity.

1.3.2.4 Size-Induced Phase Transitions

According to the reports by Shiratori et al. the phase transition of $NaNbO_3$ may also be induced by the particle size, although the exact mechanism is not clearly understood (Shiratori et al., 2005). The powder was obtained by microemulsion-mediated synthesis with subsequent annealing and the authors reported that the O_1 phase (analogous to the antiferroelectric *P* phase) is stable in coarse powder with particles larger than about 600 nm, the O_2 phase (analogous to the ferroelectric *Q* phase) in the powder with the particle size between 200 and 600 nm, and the O_3 phase in the nanopowders with the particle size below 70 nm. In a more recent study, they also reported that the O_2 phase (analogous to the *Q* phase) undergoes a phase transition towards the coarse phase in the temperature range between 285 °C and 333 °C, possibly through the coexistence of both phases (Shiratori et al., 2007).

The authors also used these powders to prepare $NaNbO_3$ ceramics and observed that

the samples with average grain sizes from 360 nm to 1.1 μm consisted of a phase mixture of the *P* and *Q* phases (Pithan et al., 2006). These samples were investigated by XRD and Raman spectroscopy; however, no clear distinction could be drawn between the two phases and no electrical characterization was performed to support the claimed antiferroelectric and ferroelectric nature of the selected phases.

The ferroelectric *Q* phase was found in some $NaNbO_3$ epitaxial thin films deposited on different substrates by radiofrequency magnetron sputtering (Takuya et al., 2007) and pulsed-laser deposition (Saito et al., 2005, Yuzyuk et al., 2010). Although these results are not comparable to the results obtained in bulk ceramics, it is interesting to note that the stresses, which develop in the films, affect the phase stability of $NaNbO_3$.

Figure 1.17 summarizes the phase transitions observed in $NaNbO_3$, induced by the temperature, electric field, particle size and stresses in epitaxial films.

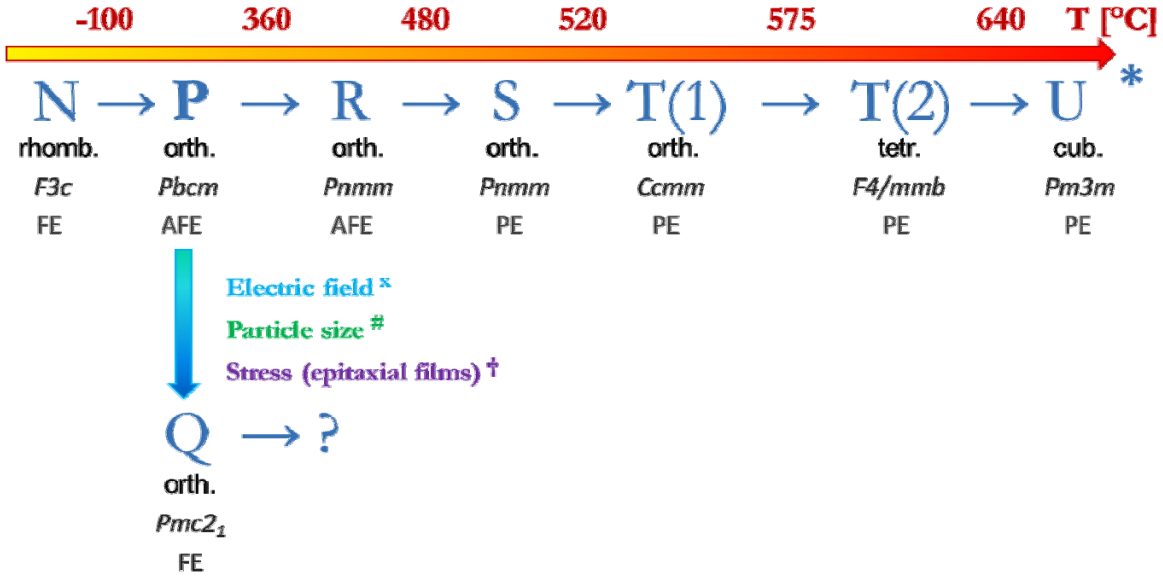

Figure 1.17: Phase transitions of $NaNbO_3$. The blue letters denote the known polymorphs; the crystal system, space group, and electrical state are listed below (FE-ferroelectric, AFE-antiferroelectric, PE-paraelectric). (* (Megaw, 1974), [x] (Cross and Nicholson, 1955, Shuvaeva et al., 1993), [#] (Shiratori et al., 2005), [†] (Saito et al., 2005, Takuya et al., 2007))

1.3.3 Electrical Properties of $NaNbO_3$

The electrical characterization of $NaNbO_3$ started together with its discovery in 1949, when Matthias determined the dielectric properties of $NaNbO_3$ single crystals and proposed that it was ferroelectric (Matthias, 1949). The ferroelectricity was disproved by the structural study of Vousden in 1951 (Vousden, 1951). Note that the concept of antiferroelectricity was established only in 1951 (Kittel, 1951). A detailed electrical characterization of $NaNbO_3$ single crystals was performed by Cross and Nicholson in 1955, who also measured the high-field properties (Cross and Nicholson, 1955). The application of the electric field up to ~87 kV/cm resulted in a linear hysteretic response of the polarization (**Figure 1.18a**). However, if the electric field was increased above this critical value, two different responses were observed:

If the applied field was parallel to the *c* axis, only linear hysteresis loops were observed up to the breakdown field at around 100 kV/cm (**Figure 1.18a**).

If the applied field was perpendicular to the *c* axis they observed double hysteresis

loops (**Figure 1.18b**). In this case the value of the required critical field for the initiation of the double loops increased with the decrease of the temperature. The antiferroelectricity at high temperatures could not be confirmed due to the increased conductivity.

It is important to note that to the best of our knowledge the double hysteresis loop in **Figure 1.18b** is the only double hysteresis loop ever reported in $NaNbO_3$. In addition, the authors reported the existence of a ferroelectric low-temperature phase, which was later denoted as the *N* phase (Darlington and Megaw, 1973).

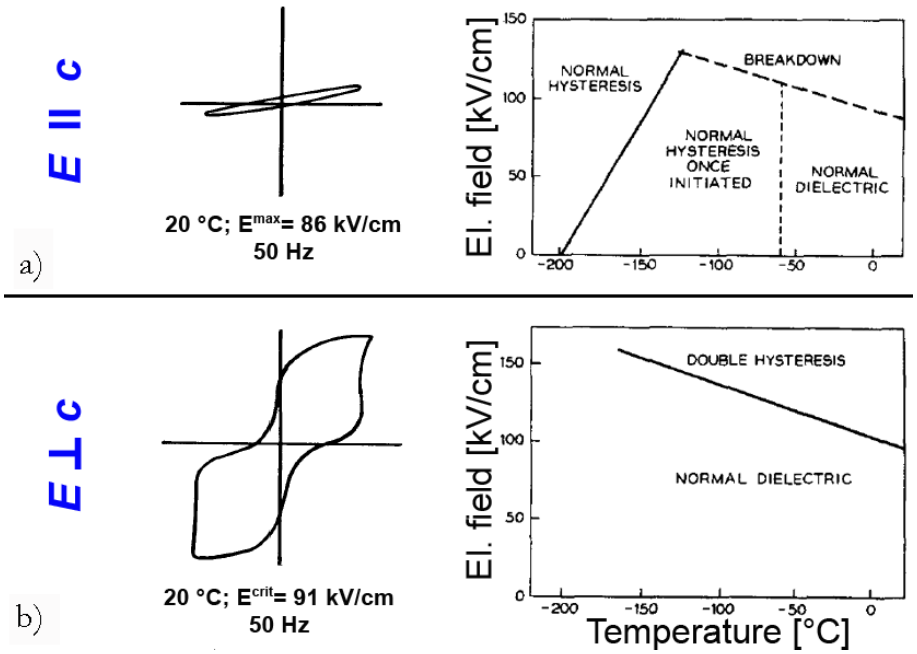

Figure 1.18: Electric hysteresis of $NaNbO_3$ single crystals for fields applied parallel (a) or perpendicular (b) to the c axis. The diagrams on the right side show the temperature dependence of the dielectric properties at large electric fields. (after (Cross and Nicholson, 1955))

Dungan and Golding were among the first to study the effect of high electric fields on $NaNbO_3$ ceramics (Dungan and Golding, 1964). At temperatures below 100 °C only a linear response of the polarization was observed for any field smaller than the electrical breakdown field. However, when the temperature was increased, ferroelectric loops were obtained if the electric field was greater than 50 kV/cm. Once the ferroelectric state was induced, it remained stable for a long period of time (years) and for temperatures up to 270 °C. The observed remanent polarization values of ~30 $\mu C/cm^2$ were considerably higher than the 2–18 $\mu C/cm^2$ previously observed in single crystals. In addition, the authors noted that the electrical properties seemed to be quite sensitive to variations in the raw materials and processing techniques, which could explain some of the discrepancies in the reported literature. Similar values were obtained by Wada et al., who reported a remanent polarization of 27 $\mu C/cm^2$ and a coercive field of 16 kV/cm for poled $NaNbO_3$ ceramics (Wada et al., 2003).

A detailed characterization of the piezoelectric properties of the ferroelectric $NaNbO_3$ ceramics was performed by Reznitchenko et al. in 2001 (Reznitchenko et al., 2001). In order to induce the ferroelectric state, the samples were heated to 140 °C, a field of 50 kV/cm was applied for 20–25 minutes and the samples were cooled down under the field to 60 °C. The measured values of the piezoelectric coefficient d_{33} were 25–50 pC/N, the thickness electromechanical coupling factor K_t was approximately 0.26–0.31, while the values for the planar electromechanical coupling factor K_p were around 0.1.

2 Aims and Hypothesis

$NaNbO_3$ has attracted the attention of researchers from various fields, mainly due to its difficult processing and the complex phase-transition behaviour (see Section 1.3). The present work is divided into three main parts, which are aimed to answer some of the open questions and contribute to a general understanding of this complex material.

The first part of the thesis deals with the preparation of $NaNbO_3$ powders with different particle sizes: submicron- and nano-sized. The submicron-sized powders are usually produced by solid-state synthesis, while for the preparation of nano-sized powders less-conventional synthesis routes, such as solution-based chemical routes or mechanochemical methods, were reported. The aim was to establish an alternative processing route for the preparation of nanopowders using conventional and well-established ceramic processing techniques, which could be upscaled. Our hypothesis was that the high-energy agitator bead milling can be used for the preparation of $NaNbO_3$ powders with nano-sized particles and a narrow particle size distribution from the submicron-sized $NaNbO_3$ powders prepared by solid-state synthesis. Furthermore, the powder compacts prepared from these nanopowders were expected to have high relative densities and narrow pore-size distributions with average pore sizes in the nano-range, which would be beneficial for the sintering process.

The second part of this work is focused on the second major step of the preparation of $NaNbO_3$ ceramics – the sintering process. The densification and obtaining of fine-grain microstructures have been reported as the major problems in the preparation of alkaline-niobate ceramics. Our hypothesis was that these problems are related to the activation of non-densifying material-transport mechanisms, which result in grain-coarsening and hinder the densifying mechanisms. Dense and fine-grained $NaNbO_3$ ceramics could possibly be prepared by using high heating rates that would surpass the low-activation energy mechanisms and enhance the densification, which is typically observed during later sintering stages. Our aim was therefore to determine the material-transport mechanism during individual sintering stages and further-on to use this knowledge to select an alternative sintering technique and prepare dense and fine-grained $NaNbO_3$ ceramics.

The third part of the thesis is dedicated to a study of the complex phase-transition behaviour of $NaNbO_3$ powders and ceramics, which were obtained in the first two sections. The temperature-induced phase transitions were extensively studied over the past 60 years; however, some controversy still remains. The first aim was therefore to re-examine the temperature-induced phase transitions of the antiferroelectric phase in order to establish a reference point for further phase-transition studies. Our hypothesis was that the coarse-grained $NaNbO_3$ ceramics undergo the same phase-transition sequence as previously reported by Megaw for the $NaNbO_3$ single crystals (Megaw, 1974). Furthermore, the aim was to investigate the influence of the grain size on the phase-transition behaviour of $NaNbO_3$ ceramics. The reduction of the grain size was predicted to result in the stabilization of the ferroelectric phase, as previously observed in the $NaNbO_3$ powders (Shiratori et al., 2005). Finally, our aim was to study the effect of the external electric field on the phase-transition behaviour of $NaNbO_3$ ceramics and to determine the critical conditions for the transitions, whereby the external-electric-field-

induced antiferroelectric-to-ferroelectric transition was expected to be irreversible.

3 Materials and Methods

3.1 Preparation of the $NaNbO_3$ Powders

3.1.1 Solid-State Synthesis of the Submicron-Sized $NaNbO_3$ Powder

The submicron-sized $NaNbO_3$ powder (submicron-NN) was prepared by solid-state synthesis from high-purity Nb_2O_5 (99.9 %, Sigma-Aldrich, Taufkirchen, Germany) and mechanically activated Na_2CO_3 (anhydrous 99.9+ %, Chempur, Karlsruhe, Germany). Activation of the carbonate was achieved by dry high-energy ball milling in a planetary ball mill (Pulverisette 4 Vaio-Mill, Fritsch, Idar-Oberstein, Germany) for 4 h using a tungsten carbide vial and balls. The submicron-sized starting powders were dried at 200 °C, mixed in a stoichiometric ratio and homogenized in a planetary mill for 4 h using acetone (p. A., AppliChem, Darmstadt, Germany) as the liquid medium. After drying the powder mixture was pressed into pellets and calcined twice in a closed alumina crucible in a chamber furnace at 700 °C for 4 h with intermediate milling. The final product was crushed in an agate mortar, milled in a planetary mill for 4 h in acetone, dried at 200 °C and finally sieved through a mesh 55 sieve.

3.1.2 Preparation of the Nano-Sized $NaNbO_3$ Powder

The nano-sized $NaNbO_3$ powders (nano-NN) were prepared by top-down processing combining the solid-state synthesis, described in the previous section, and subsequent bead-milling. A suspension of the submicron-NN powder and isopropyl alcohol (p. A., AppliChem, Darmstadt, Germany) was prepared using an ultrasonic bath and pumped through the MiniCer agitator bead mill (Netzsch Feinmahltechnik, Selb, Germany) using a peristaltic hose pump (**Figure 3.1**). Fine zirconia beads with a diameter of 0.5 mm were used as the grinding medium (Tosoh Corporation, Tokyo, Japan) and different rotation speeds of the agitator shaft were tested in order to determine the optimal comminution conditions.

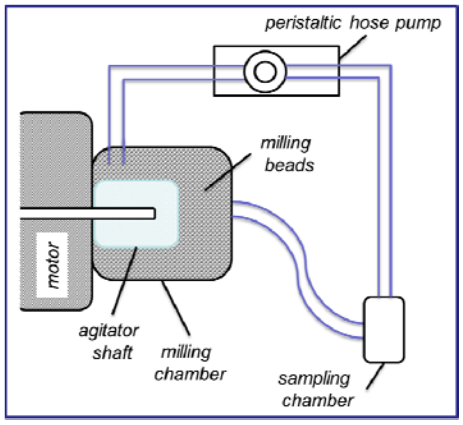

Figure 3.1: Schematic representation of the MiniCer agitator bead mill used for the preparation of the nano-sized $NaNbO_3$ powders.

3.1.3 Powder-Characterization Methods

The particle sizes and size distributions of the obtained submicron-NN and nano-NN powders were investigated with a static, light-scattering granulometer (Microtrac S3500 Particle Size Analyzer, Montgomeryville, PA, USA). The particle size area distributions from these measurements are described with the 90 % particle size limit (d_{90}), 50 % particle size limit (d_{50}, median value), and 10 % particle size limit (d_{10}).

The powder morphology was investigated using a field-emission scanning electron microscope (FE-SEM JSM-7600F, Jeol, Tokyo, Japan) with an operating voltage of 5 kV. Prior to imaging the powders were coated with a thin conductive layer of carbon (SCD 050, Balzers AG, Balzers, Liechtenstein).

The specific surface areas of the powders were measured using the N_2 adsorption BET method (NOVA 2200E Quantachrome Instruments, Boynton Beach, FL, USA). Prior to the measurements the powder samples were degassed in vacuum at 200 °C for 2 h in order to remove the adsorbed gases from the particle surfaces. The BET equivalent particle diameters (d_{BET}) were calculated using the following equation:

$$d_{BET} = \frac{\psi_A / \psi_V}{S_M \cdot \rho_{abs}^t} \tag{3.1}$$

where S_M is the specific surface area, $\rho_{abs}{}^t$ is the theoretical density of $NaNbO_3$ (4.55 g/cm^3; 01-082-0606 (PDF-ICDD, 2011)), and ψ_A/ψ_V is the shape-factor ratio, for which a value of 6 was assumed (Reed, 1995).

The crystallite sizes and the microstrain values were obtained from the X-ray line-broadening analysis. The XRD patterns were collected using the X'Pert PRO MPD diffractometer equipped with a Ge(111) monochromator (PANalytical, Almelo, The Netherlands) within the angular 2θ range of 10° to 140°, using a 0.026° step and 100s/step. The diffractograms were fitted using the Rietveld refinement method (Rietveld, 1969) using the FullProf Suite software package (Rodriguez-Carvajal, 2011). The modified Thomson-Cox-Hastings-pseudo-Voigt function was used to describe the peak shapes, while the background was fitted using a 6-coefficient polynomial function. In order to subtract the instrumental contribution of the profile line broadening, the instrumental resolution function was measured beforehand using the line-profile standard reference material LaB_6. The results obtained from the line-broadening analysis are given

as the average apparent crystallite size and the average maximum (upper limit) microstrain (e_m), while the root mean square strain (*RMSS*) was calculated according to the following equation, assuming pure Gauss strain broadening (Snyder et al., 1999):

$$RMSS = \sqrt{\frac{2}{\pi}} \cdot e_m \tag{3.2}$$

3.1.4 Preparation and Characterization of Powder Compacts

In order to prepare the green powder compacts, the $NaNbO_3$ powders were first pressed with a uniaxial pressure of 100 MPa (PW10, Paul-Otto Weber Laborpresstechnik, Remshalden, Germany) and subsequently isostatically with pressures ranging from 200 MPa to 740 MPa (WIP 32260, Autoclave Engineers Inc., Erie, PA, USA or Indos, Ljubljana, Slovenia). The relative green densities were calculated from the dimensions and the masses of the samples.

The pore-size and size-distribution measurements of the powder compacts were performed using the N_2 sorption method. The samples were first dried at 250 °C for 4 h and subsequently degassed in vacuum at 200 °C for 2 h prior to the measurement. The pore size distributions were calculated from the desorption curves using the method proposed by Barrett, Joyner and Halenda (BJH method) (Barrett et al., 1951).

3.2 Sintering Experiments

3.2.1 Dynamic Sintering Curves and Microstructure Evolution

The dynamic sintering curves of the powder compacts were recorded upon heating with a heating rate of 10 K/min using an optical dilatometer (Leitz V. 1A, Leitz, Wetzlar, Germany). The dimensions of the samples were continuously measured from the digitalized images and the relative shrinkage ($\Delta l/l$) and the technical shrinkage ($(\Delta l/l)_{\text{tech.}}$) were calculated according to the following equations:

$$\left(\frac{\Delta l}{l}\right) = \frac{l_{RT} - l_T}{l_{RT}} \cdot 100 \tag{3.3}$$

$$\left(\frac{\Delta l}{l}\right)_{tech.} = \left(\frac{\Delta l}{l}\right) + CTE \cdot 100 \cdot (T - RT) \tag{3.4}$$

where l_{RT} is the initial dimension of the sample at RT, l_T is the dimension of the sample at the selected temperature, *CTE* is the linear coefficient of thermal expansion, *T* is the selected temperature and RT is room temperature. The relative densities of the green samples were measured from the dimensions and the mass of the samples, while the relative densities at elevated temperatures (ρ_{rel}) were calculated according to:

$$\rho_{rel} = \frac{\rho_{rel}^{GR}}{\left(1 - \frac{\left(\frac{\Delta l}{l}\right)_{tech.}}{100}\right)^3} \tag{3.5}$$

where ρ_{rel}^{GR} is the relative green density.

In order to track the evolution of the microstructure during sintering, a series of green samples was heated at selected temperatures and quenched in air in order to preserve the high-temperature state. The fracture surfaces of these samples were investigated using a field-emission scanning electron microscope. Prior to analysis the fracture surfaces were sputter-coated with a thin conductive layer of carbon (SCD 050, Balzers AG, Balzers, Liechtenstein). The grain sizes of these samples were estimated from the SEM images of the fracture surfaces (D_e^{FR}, where *e* marks the estimated value and *FR* the fracture surface). In some samples, however, this was not possible since the grain sizes were very small and the relative densities were below 60 %. In these cases the grain sizes were determined by the BET method, as described in Section 3.1.3, and are given as BET equivalent grain size diameters (D_e^{BET}). Note that this latter method gives slightly overestimated values of the grain sizes, since we only measure the surface area, which is accessible by the N_2 molecules, while the real specific area of the grains is larger. This approximation is justified only at very low relative densities, when the total grain-boundary area is very small compared to the total surface area of the grains.

3.2.2 Determination of the Sintering Mechanisms

The initial stage sintering mechanism was determined by the specific surface area reduction method (German and Munir, 1976). The $NaNbO_3$ powders were pressed into compacts with a diameter of 6 mm by applying a uniaxial pressure of 100 MPa and an isostatic pressure of 200 MPa. The specific surface areas of these green samples were measured by the N_2 adsorption BET method, as described in Section 3.1.3, and an average of 8 measurements was taken for the initial specific surface area value (S_0). These samples were then sintered isothermally at different temperatures between 500 °C and 600 °C for different times in an air atmosphere in a tube furnace. Small sample sizes and the rapid insertion of the samples into the furnace were used in order to achieve rapid sample heating, which is assumed in the calculation model. The specific surface area of the samples was measured again after the sintering step and an average of three measurements was taken for the latter calculation for each sintering temperature and sintering time. The isothermal experiment aimed at investigating the shrinkage of the sample during the initial sintering stage was performed using the same optical dilatometer as described in Section 3.2.1.

In order to investigate the sintering mechanisms that are active during the latter sintering stages, we prepared another series of $NaNbO_3$ green samples, as described in the previous Section. One of these samples was isothermally sintered at 1350 °C for 90 minutes in the optical dilatometer described in Section 3.2.1 in order to measure the shrinkage curve, while four samples were sintered isothermally at 1350 °C for different times in a tube furnace. All these sintering experiments were performed in an air atmosphere. The densities of the sintered samples were calculated from the measured dimensions and mass, while the grain sizes were determined from the FE-SEM images of the grinded, polished and thermally etched samples (D_m^{TE}, where *m* marks the measured value and *TE* the thermally etched sample). We used the SiC grinding papers with gradations 1200 (15 µm), 2400 (10 µm) and 4000 (5 µm) for grinding while 3-µm and 0.25-µm diamond pastes were used for the polishing (Struers, Ballerup, Denmark). The digitalized microstructures were processed with the Image Tool Software (Wilcox et al., 2002) to obtain areas with more than 400 grains per sample. The grain size values are given as the mean diameters, which were calculated from the measured area values (A_G):

$$D_m^{TE} = \sqrt{\frac{4 \cdot A_G}{\pi}} \tag{3.6}$$

The volatility of Na during the heating of $NaNbO_3$ was determined using a combination of Knudsen effusion mass spectrometry (KEMS) and thermodynamic calculations. The Na_2CO_3-Nb_2O_5 powder mixtures with different Na/Nb ratios were prepared and calcined, as described in Section 3.1.1. The obtained powders were loaded into an alumina Knudsen cell, evacuated and heated at 523 °C for 2 h in order to degas the powder sample. Subsequently, the temperature was increased to 727 °C, equilibrated and the Na current (I_{Na}), exiting the Knudsen cell, was analysed with a mass spectrometer. The vapour pressure of Na was obtained using the following equation:

$$p_{Na} = \left(\frac{\Sigma_i I_{Na}}{\Sigma_i I_{ref}}\right) \cdot \left(\frac{\sigma_{ref}}{\sigma_{Na}}\right) \cdot \left(\frac{\eta_{ref}}{\eta_{Na}}\right) \cdot p_{ref} \tag{3.7}$$

where I_{ref} is the ion current of the reference material, σ_{ref} and σ_{Na} are the ionisation cross-sections, η_{ref} and η_{Na} are the isotope-abundance factors of the reference and the investigated material, respectively, and p_{ref} is the vapour pressure of the reference material. The high-temperature vaporisation reaction is as follows (Shafer and Roy, 1959):

$$Na_2O(s) \Leftrightarrow Na_2O(g) \Leftrightarrow 2Na(g) + \frac{1}{2}O_2(g) \tag{3.8}$$

The activity of Na_2O in the system can therefore be calculated as:

$$a_{Na2O} = \frac{p_{Na2O(g)}}{p^*_{Na2O(g)}} = \left(\frac{p_{Na(g)}}{p^*_{Na(g)}}\right)^{5/2} \tag{3.9}$$

where the asterisk marks the vapour pressure over pure Na_2O. The obtained results were used to determine the standard thermodynamic functions of selected compounds in the Na_2O-Nb_2O_5 system. These data were incorporated into the IVTANTHERMO database (Database on Thermodynamic Properties of Individual Substances and Thermodynamic modelling Software, Glushko Thermocenter of RAS, Moscow, Russian Federation) to perform equilibrium calculations at different temperatures in an air atmosphere.

3.2.3 Pressure-Assisted Sintering

In order to prepare the green compacts for pressure-assisted sintering, the powder was compressed into pellets with a diameter of 6 mm and a height of about 10 mm by applying a uniaxial pressure of 100 MPa and an isostatic pressure of 740 MPa. The green samples were loaded into an alumina die with a diameter of 10 mm and the surrounding void was filled with the packing powder. The packing powder was prepared from $NaNbO_3$ pellets sintered by conventional means and subsequently crushed in an agate mortar to obtain coarse-grained $NaNbO_3$ powder. The heating rate was 10 K/min. During sintering a uniaxial pressure of about 24.5 MPa was applied through alumina rams. The experimental setup is schematically presented in **Figure 3.2**.

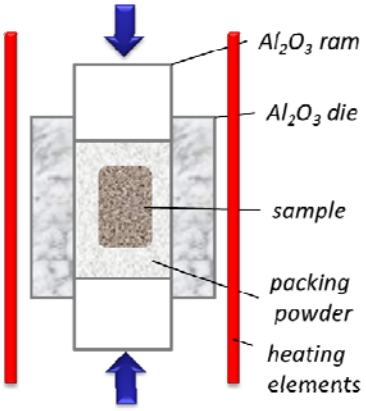

Figure 3.2: Schematic representation of the setup for the pressure-assisted sintering of $NaNbO_3$.

After the sintering the surfaces of the samples were slightly ground in order to remove the residual packing powder, while the relative densities were calculated from the measured dimensions and the mass of the sample or by the Archimedes method. The mean grain sizes and size distributions of the sintered samples were determined from FE-SEM images of the polished and thermally etched samples, as described in Section 3.2.2. For each sample a minimum of 150–200 grains was measured.

3.2.4 Abnormal Grain-Growth Studies

The samples for studying the abnormal grain growth were prepared by conventional sintering in an air atmosphere using a tube furnace. The preparation of the green compacts and the density measurements were the same as reported in Section 3.1.4.

The average grain sizes, grain size distributions and number of pores were measured from the digitalized images of the polished and thermally etched samples, as described in Section 3.2.2, to obtain the areas of more than 350 grains per sample.

3.3 Phase-Transition Studies

The studies of the phase-transition behaviour of $NaNbO_3$ were performed on three groups of samples:

Large-grained $NaNbO_3$ ceramics (ceramics with average grain sizes above 2 µm) were used to study the temperature-induced phase transitions (Section 4.3.1) and electric-field-induced phase transitions (Section 4.3.3).

Submicron-sized $NaNbO_3$ powder (submicron-NN; powder with a particle size around 0.07–0.17 µm) was used to study the occurrence of the size-induced phase transition (Section 4.3.2.1).

$NaNbO_3$ ceramics with a wide grain-size range (ceramics with average grain sizes between 0.15 µm and 50 µm) were used to study the effect of the grain size on the phase-transition behaviour (Section 4.3.2.3).

The preparation procedures for all these samples are described in Sections 3.1 and 3.2, while the different characterization methods used for the study of the phase transitions are described in the following sections.

3.3.1 Differential Scanning Calorimetry

The differential scanning calorimetry (DSC) curves were recorded on a Netzsch DSC 204 F1 high-temperature calorimeter (Netzsch-Gerätebau, Selb, Germany) in the temperature range between RT and 700 °C with a heating rate of 2 K/min. The sample, either powder or ceramic, with a mass of about 30–110 mg, was tightly packed in a Pt crucible with a pierced lid and loaded into the calorimeter. The instrumental baseline was determined prior to the measurement using an empty Pt crucible and the same temperature programme. The temperatures of the phase transitions will be reported either as the maxima or the onset of the DSC peaks.

3.3.2 Dielectric Spectroscopy

Disc-shaped samples for dielectric measurements were cut from the sintered samples using a diamond-wire saw, ground and polished (see Section 3.2.2) to obtain sample thicknesses between 0.3 and 0.5 mm. Subsequently, these pellets were annealed for 30 minutes at 700 °C in order to relax the stresses, which may occur during sample preparation, and cooled down with a slow cooling rate of 1 K/min. Thin gold electrodes with a diameter of 5 or 6 mm were magnetron-sputtered on the samples (Cinquepascal SRL, Trezzano, Italy) and the dielectric measurements were performed using an E4980A high-precision LCR meter (Agilent Technologies, Santa Clara, CA, USA) or a 4192A LF Impedance Analyzer (Hewlett Packard, Tokyo, Japan) equipped with a tube furnace. The investigated temperature range was between RT and 450 °C, the measuring step 1 °C, while the heating rate was 2 K/min.

3.3.3 X-ray Diffraction Measurements and Structure Calculations

The XRD patterns were recorded within the angular 2θ range of 10°–90°, using a 0.014° or 0.026° step and 100–130 s/step, on three different diffractometers: X'Pert PRO MPD (Cu $K_{\alpha 1}$ radiation; Ge(111) monochromator; PANalytical, Almelo, The Netherlands), X'Pert PRO (Cu $K_{\alpha 1}$/ $K_{\alpha 2}$ radiation; PANalytical, Almelo, The Netherlands), and D8 (Cu $K_{\alpha 1}$ radiation; Ge(111) monochromator; Bruker-AXS, Karlsruhe, Germany). The latter two were equipped with a high-temperature chamber and were therefore used for measuring the diffraction patterns at elevated temperatures.

The crystallographic cards from the ICDD-PDF database were used for the qualitative analysis (PDF-ICDD, 2011), while the crystal-structure analysis was performed with the Rietveld method (Rietveld, 1969) using the JANA2006 software package (Petricek and Dusek, 2006). The unit-cell parameters are reported either as the true unit-cell parameters or the reduced unit-cell parameters. The latter are used for an easier comparison of the structural parameters between different phases.

3.3.4 Ferroelectric and Piezoelectric Properties

The samples for electrical measurements under high electric fields were prepared as follows: the sintered pellets were cut, ground and polished to obtain discs with a diameter of 5–7 mm and a thickness of 0.3–0.5 mm. The pellets were annealed as described in Section 3.3.2, coated with silver paste and fired at 50 °C for 1 h, 200 °C for 2 h and finally at 400 °C for 2 h.

The polarization versus electric field loops were measured using a Sawyer-Tower circuit. An Agilent 33220A signal generator (Agilent Technologies, Santa Clara, CA, USA) was connected to a TREK 20/20C high-voltage amplifier (TREK Inc., Medina,

NY, USA) in order to create a sine-wave electric field, while the input and output signals were monitored with an Agilent 54624A oscilloscope (Agilent Technologies, Santa Clara, CA, USA). The longitudinal strain was measured using a linear variable differential transformer (LVDT). For high-temperature measurements the sample holder was immersed into a Proline P8 silicon-oil bath with a temperature control unit (Lauda Dr. R. Wobser, Lauda-Königshofen, Germany). In all the high-field experiments silicon oil (Wacker-Chemie, München, Germany) was used to avoid electric discharge.

The piezoelectric d_{33} coefficient was measured using a Berlincourt-type d_{33}-meter (Piezometer System PM10, Take Control, Birmingham, UK) and the measurement was performed about 24 h after poling.

4 Results and Discussion

4.1 Preparation and Characterization of $NaNbO_3$ Powders

The main goal of this section is to introduce a new processing route for $NaNbO_3$ nanopowders, to characterize the obtained products using different methods and to compare the result with other processing routes reported in the literature. The last part investigates the compaction behaviour and suitability of the prepared powders for the sintering studies discussed in subsequent sections.

4.1.1 Submicron-Sized $NaNbO_3$ Powder

Submicron-sized $NaNbO_3$ powder was prepared by solid-state synthesis and subsequent milling in a planetary mill, as described in Section 3.1.1, and will be further denoted as "submicron-NN". According to the XRD analysis (**Figure 4.1**) the obtained powder was single phase and all the peaks could be described with the crystallographic card of the orthorhombic $NaNbO_3$ (01-082-0606; space group $P2_1ma$ (PDF-ICDD, 2011)). A detailed crystal-structure analysis of this powder will be given in Section 4.3.2.

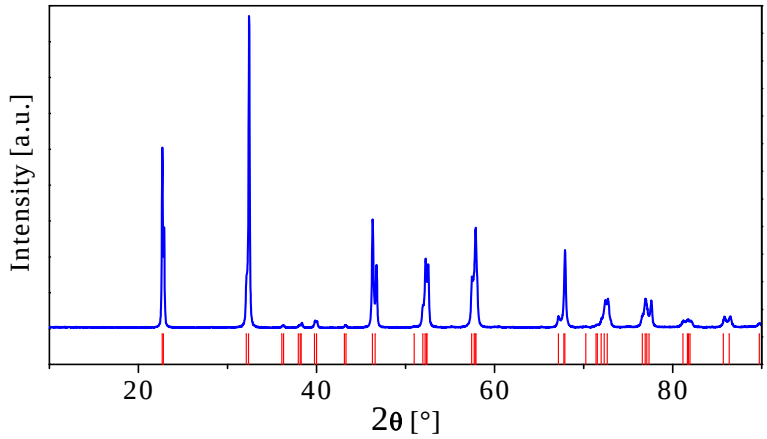

Figure 4.1: XRD pattern of the submicron-sized $NaNbO_3$ prepared by solid-state synthesis (blue line). All the peaks could be described with the crystallographic card of the orthorhombic $NaNbO_3$ (red tick marks; 01-082-0606 (PDF-ICDD, 2011)).

The FE-SEM images and the particle size distribution of the submicron-NN, as measured by laser granulometry, are presented in **Figure 4.2**. The powder consisted of primary particles with an estimated size of 70–170 nm and strong aggregates of 400–700 nm. Milling in the planetary mill after the calcination obviously failed to break all the aggregates that were created during the calcination process.

In addition, the submicron-NN powder was investigated using the N_2 adsorption BET method. The specific surface area was 5.81 m^2/g, which corresponds to a d_{BET} particle size of about 230 nm (**Equation 3.1**). The fact that the d_{BET} particle size is larger than

observed under the FE-SEM (70–170 nm), agrees with the proposed presence of strong aggregates that could not be penetrated by the N_2 molecules and thus the measured specific surface area was smaller.

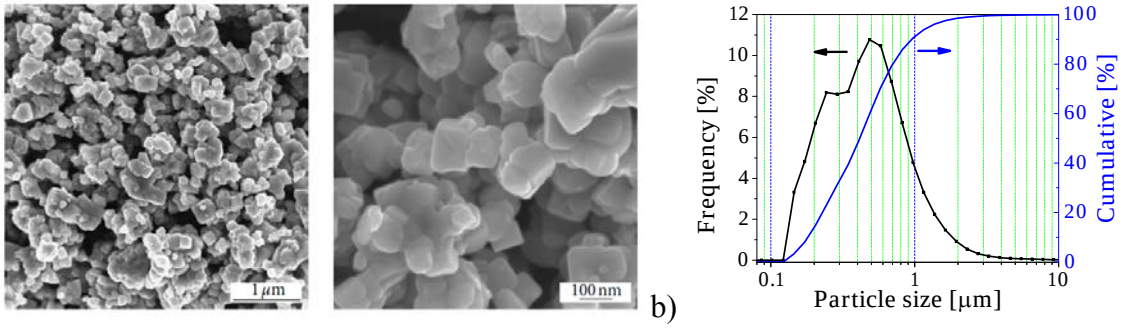

Figure 4.2: FE-SEM images (a) and particle size distribution obtained by granulometric analysis (b) of the submicron-NN prepared by solid-state synthesis.

4.1.2 Nano-Sized $NaNbO_3$ Powder

In order to prepare the nano-sized $NaNbO_3$ powder, the submicron-NN was milled in the agitator bead mill, as described in Section 3.1.2. The milling process was followed by measuring the particle size distributions by laser granulometry. However, as shown during the evaluation of the submicron-NN (**Figure 4.2**), this method does not always give the true size of the primary particles. Therefore, laser granulometry was only used for qualitative analysis during the milling process, while complementary analysis, such as FE-SEM imaging and specific surface area measurements using the BET method, were carried out on the final milling products and will be presented later on in this section. The results of the milling process with different rotation speeds of the agitator shaft for milling times up to 75 min are presented in **Figure 4.3**. The resulting milled powders are denoted as "nano-NN-1000", "nano-NN-1500", and "nano-NN-2000", whereby the number refers to the applied rotation speed of the agitator shaft in min^{-1}. We observed a considerable narrowing of the size distributions and a major decrease of the *d*-values during the first 30 min of the milling process, while the size reduction was negligible with any further increase of the milling time. The milling process was stopped after 75 min, since the particle size did not significantly decrease with a further increase in the milling time or in some cases even increased due to agglomeration. In addition, long milling times could cause contamination of the milled powder due to wear of the zirconia beads and should therefore be avoided. The optimum conditions for the milling, where we obtained the lowest *d*-values, were identified to be a rotation speed of 2000 min^{-1} and a milling time of around 75 min. The resulting nano-NN-2000 powder is presented in **Figure 4.4**. The primary particle size, as estimated from the FE-SEM images, is below 50 nm. The larger particle size values, obtained by granulometric measurements, are due to partial particle agglomeration.

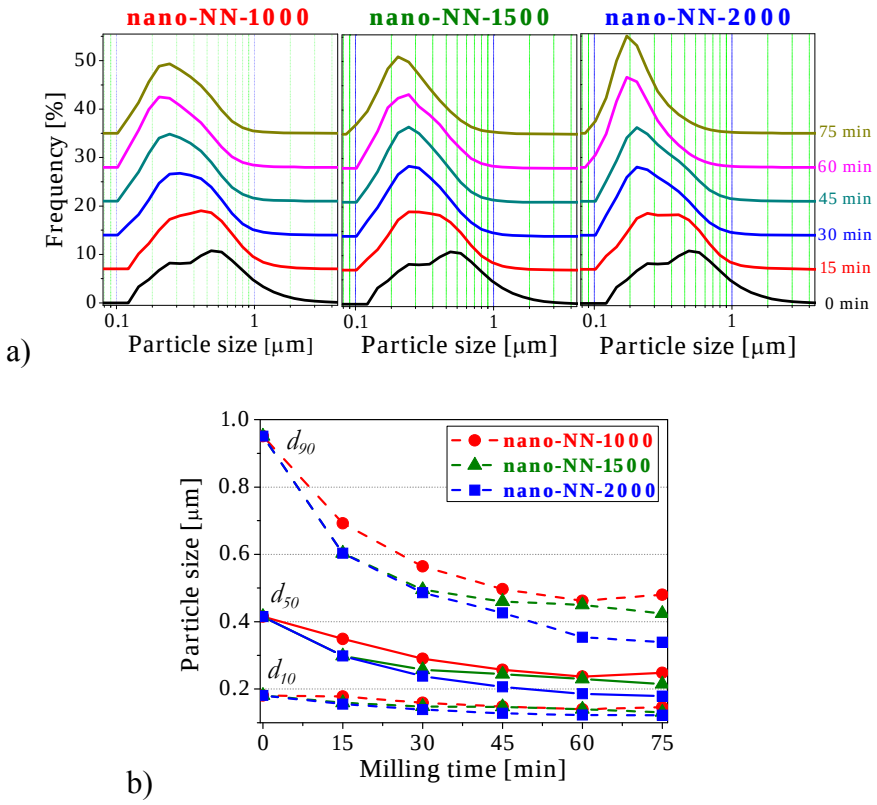

Figure 4.3: Particle size distributions (a) and characteristic particles sizes (b) during milling of $NaNbO_3$ with different rotation speeds of the agitator shaft: 1000 min^{-1} (nano-NN-1000), 1500 min^{-1} (nano-NN-1500), and 2000 min^{-1} (nano-NN-2000).

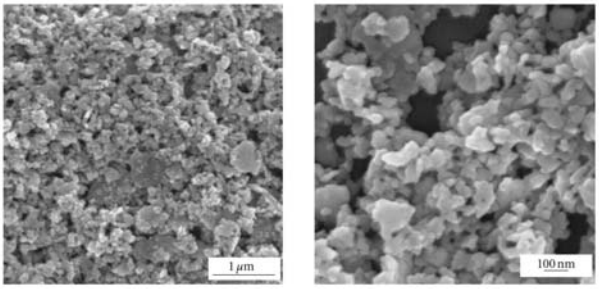

Figure 4.4: FE-SEM images of the nano-NN-2000 powder prepared by 75 min milling using a rotation speed of 2000 min^{-1}.

In order to additionally evaluate the milled powders, we measured their specific surface areas and compared them to the specific surface area of the submicron-NN (**Figure 4.5**). The milling with the optimized milling parameters (75 min, 2000 min^{-1}) resulted in an almost 10 times increased specific surface area: from the initial 5.8 m^2/g to the final 52.6 m^2/g. Consequently, the d_{BET} primary particle size also decreased from an initial 230 nm to 25 nm for the nano-NN-2000 powder. This result is in agreement with the FE-SEM observations (**Figure 4.4**). In contrast to the aggregates, observed in the submicron-NN, the presence of agglomerates, detected by the laser granulometer in nano-NN powders, did not seem to influence the BET measurement, which could indicate their loose packing.

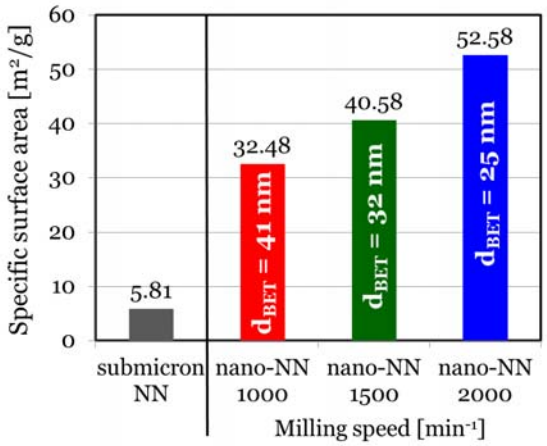

Figure 4.5: Specific surface areas of the nano-NN-1000, nano-NN-1500, and nano-NN-2000 powders, as measured by the BET method. The calculated d_{BET} values are included in the corresponding columns. The specific surface area of the submicron-NN is added for comparison.

The XRD patterns of the nano-NN powders are presented in **Figure 4.6**, where the submicron-NN is also added for comparison. All the nanopowders were single phase and no additional peaks were observed. We assume that the milling process did not introduce any significant contamination of the powders. This was additionally supported by the EDS/TEM investigations of the $NaNbO_3$ ceramics, which were produced from these powders, where no traces of zirconia were observed (Benčan A., private communication).

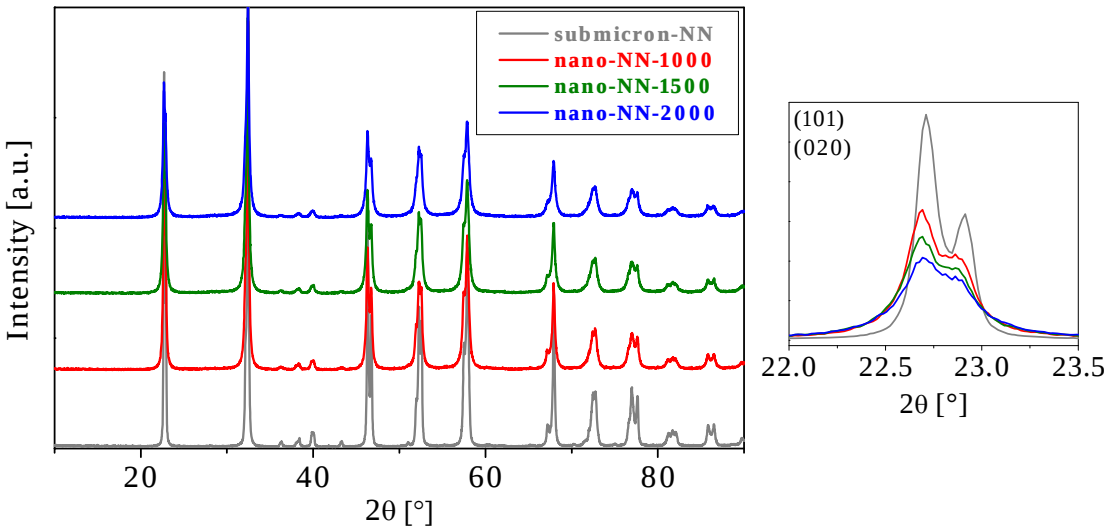

Figure 4.6: XRD diffractograms of the nano-NN-1000, nano-NN-1500, and nano-NN-2000 powders. The submicron-NN is added for comparison. The right-hand-side image shows the broadening of the diffraction peaks.

The diffractograms of the nanopowders also showed peak broadening, which was the consequence of a reduction of the particle size and the introduction of microstrains during the milling process (Snyder et al., 1999). In order to evaluate these effects, we performed an XRD line-broadening analysis using the Rietveld refinement method (Rietveld, 1969) (Section 3.1.3). The calculated average apparent crystallite size of the submicron-NN was 89 nm, while crystallite sizes of the nano-NN powders decreased with increasing milling speed from 1000 min^{-1} to 2000 min^{-1} (**Figure 4.7**). These results were in good agreement with the results obtained by the BET analysis (**Figure 4.5**). Note that, when using

laboratory monochromatic X-rays, the line broadening analysis is only accurate for small crystallite sizes up to about 90–190 nm (Snyder et al., 1999) and therefore the calculated values for the submicron-NN should be considered with care, since they are within the range of the analysis upper limit.

The calculated microstrains were similar for all the milled nano-NN powders and the root-mean-square strains (*RMSS*) reached a value of about 2.0–2.1 %, which was about 0.5 % higher than in the submicron-NN. This result indicated the inducement of defects during agitator bead milling; however, the method does not provide any information regarding the nature of these defects. The observed microstrain values were higher than the one reported for the $NaNbO_3$ nanopowders prepared by mechanochemical synthesis, where RMSS in the range of 1.3 % were reported for 20 h of dry milling in a planetary mill (Rojac et al., 2007). The reason for this difference could be the fact that crystallization processes, which occur during mechanochemical synthesis, could decrease the amount of defects and thus the amount of disorder inside the particles.

Vojisavljević et al. investigated the evolution of microstrains in ZnO nanoparticles during dry planetary ball-milling in air using 10 mm ZrO_2 milling balls and a rotation speed of 400 min^{-1} (Vojisavljević et al., 2008). After a milling time of 300 min the obtained RMSS in the ZnO nanoparticles, as calculated from the structural refinement of the XRD data, were around 1.5 % and the particle size was 15 nm. Due to the nature of the agitator bead mill (high milling-ball load) we expect that the forces acting on the particles are predominantly the shear forces, whereas in the case of planetary milling the particles are mostly exposed to impact forces. Therefore, we assume that the higher level of disorder and microstrains in our nano-NN samples could be related to the action of the shear forces.

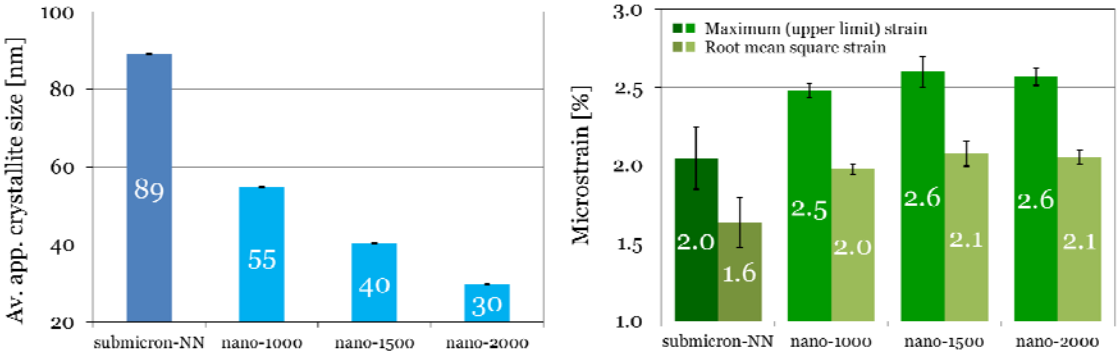

Figure 4.7: Average apparent crystallite sizes and microstrains of the submicron-NN and the nano-NN powders, as determined by the XRD line-broadening analysis.

The powder with the finest particle size was obtained when using the 2000 min^{-1} milling speed (nano-NN-2000 powder) and therefore this powder was used for further sintering studies. For the sake of simplicity this powder will be further denoted as "nano-NN".

4.1.3 Compaction Behaviour of $NaNbO_3$ Powders

The compaction behaviour of the submicron-NN and the nano-NN powders under isostatic pressure is presented in the form of a compaction-response diagram in **Figure 4.8** (Matsumoto, 1986). The density vs log-pressure curve of the submicron-NN has a constant slope throughout the whole investigated pressure range and reaches the highest relative density of about 69 % at a pressure of 790 MPa. Different compaction behaviour

was observed in the case of the nano-NN powder, where lower relative densities were measured in the pressure region up to 550 MPa, while a steeper slope, revealing a better compaction of this powder, resulted in higher relative densities at pressures above 550 MPa. The interpolated value of 64 % relative density at 450 MPa for the nano-NN powder is comparable to the value reported for the compaction of the solution-derived $NaNbO_3$ nanopowder (Lanfredi et al., 2000). However, the authors reported that this relative density was the limiting value, while in our case it seems to be higher, since the relative density increased up to a pressure of about 650 MPa, where a relative density of about 69.2 % was observed.

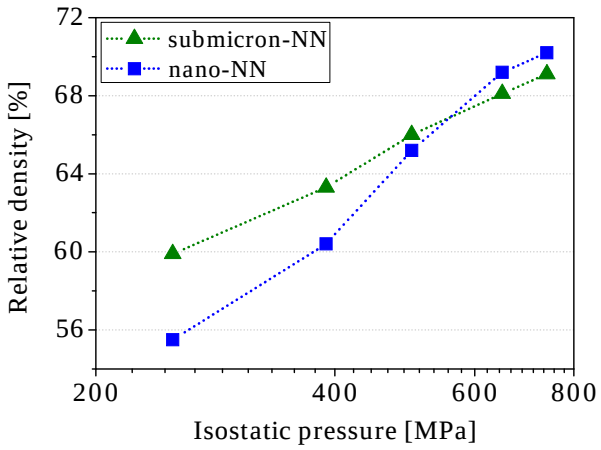

Figure 4.8: Compaction-response diagram of the submicron-NN and nano-NN powders. Note that the dotted lines are a guide for the eye only.

The compaction behaviour of the powders directly influences the pore size and size distribution within the green compact, which later on play an important role during the sintering process. A uniform pore size distribution, which is a reflection of a uniform packing of particles, should promote sintering and densification (Rahaman, 2003). The pore size distributions of the nano-NN green samples, compacted with different isostatic pressures, are presented in **Figure 4.9**, as measured using the N_2 desorption method (Section 3.1.4). The average pore radius is decreased by increasing the applied isostatic pressure and all the values are in agreement with the theoretical pore sizes radius of 3–7 nm, calculated for the interstitial sites in the case of close-packing of monodispersed spheres. Moreover, only one peak was observed in each distribution up to the detection limit of this method, which is at a pore diameter of 400 nm (Allen, 1997). This mono-modality of the distributions indicates the absence of agglomerates in the green samples. A similar analysis was performed for the submicron-NN green compacts, where the distributions were also monomodal; however, they were much broader and the average pore radius was approximately 20–30 nm.

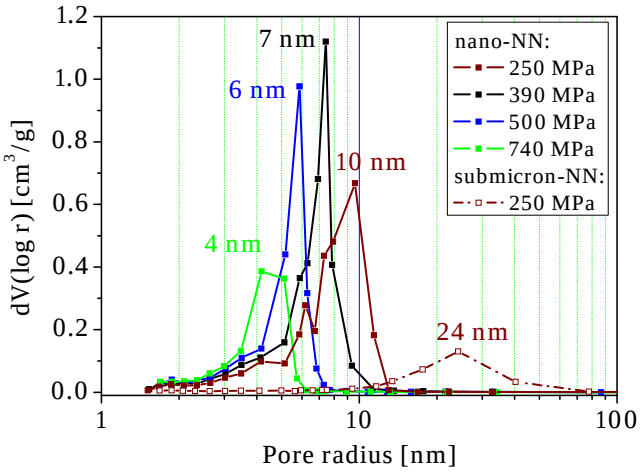

Figure 4.9: Pore-size distributions of the nano-NN and submicron-NN green samples, compacted with different isostatic pressures, as measured by the N_2 desorption method. The numbers above the curves represent the average pore radii.

4.1.4 Summary

Single-phase $NaNbO_3$ powder with an average primary particle size of 70–170 nm and an aggregate size of 400–700 nm was obtained by solid-state synthesis and subsequent milling in a planetary mill. This powder was further milled in an agitator bead mill to prepare $NaNbO_3$ nanopowder with an average particle size of approximately 25–30 nm, which is within the range reported for $NaNbO_3$ nanopowders prepared by other techniques, such as solution methods (Lanfredi et al., 2000, Nobre et al., 1996, Pithan et al., 2005) and mechanochemical synthesis (Rojac et al., 2005). In addition, microstrains of around 2 % were found in the nanopowders, which could indicate the presence of defects, created during the milling process.

The compaction behaviour of the powders was investigated in order to establish a suitable starting point for the investigation of the sintering process. The average pore radius in green compacts was about 4–10 nm and 20–30 nm for the nano-NN and submicron-NN powder, respectively. In all cases monomodal pore size distributions were observed, which indicated the absence of agglomerates in the green samples.

4.2 Sintering of $NaNbO_3$

The second main section of the thesis is focused on the major step in the preparation of $NaNbO_3$ ceramics – the sintering process. Only a few systematic reports on the sintering of alkali niobates can be found in the literature and therefore we first needed to investigate the microstructure evolution and understand the material transport mechanisms, which are active during individual sintering stages. This knowledge was further-on used to select a sintering technique to obtain dense $NaNbO_3$ ceramics in a wide grain-size range.

4.2.1 Microstructure Evolution During Constant-Rate Heating

The macroscopic behaviour of the submicron-NN compacts during heating was investigated by recording the dynamic sintering curves using an optical dilatometer (**Figure 4.10**). All the sintering experiments reported in this section were performed on samples compacted using an isostatic pressure of 200 MPa, which resulted in green densities of around 59 % and 54 % for the submicron-NN and nano-NN, respectively. Note that some experiments were also performed on samples with a higher green density; however, the resulting sintering behaviour was similar and thus these results are not presented here. An average linear thermal expansion coefficient of $16 \cdot 10^{-6}$ K^{-1}, as measured by contact dilatometry, was used to calculate the technical shrinkage (**Equation 3.4**). The submicron-NN powder compact started to shrink at around 1280 °C, where we observed a steep slope in the shrinkage curve and rapid densification, just before reaching the melting point of the material at 1412 °C. The shrinkage rate between 1280 °C and 1412 °C was 0.11 %/°C. This very narrow shrinkage interval is typical for alkaline niobates and was previously reported by several authors (Kosec and Kolar, 1975, Malič et al., 2008, Nobre et al., 1996).

The densification of the nano-NN compact during heating started at around 1180 °C, which is about 100 °C lower than the submicron-NN compact. In the temperature range between 1180 °C and 1340 °C, the sample was shrinking with a rate of 0.03 %/°C and a relative density of 64.5 % was obtained at 1340 °C. However, at this temperature a change of the slope was observed in the shrinkage curve and upon further heating the sample shrank with a much faster rate of about 0.20 %/°C. The melting point of this sample was at 1400 °C. The comparison of the densification curves upon heating (**Figure 4.10b**) revealed a greater similarity between the two samples – the nano-NN sample started to densify earlier; however, at around 1280 °C it reached the same relative density as the submicron-NN sample. Above this temperature the curves almost coincided, although the nano-NN curve was slightly shifted towards lower temperatures (5–10 °C). This may indicate that the differences in particle size between the submicron-NN and nano-NN, which were clearly seen in the powder state of the samples, disappeared before the samples entered the main densification stage of the sintering process.

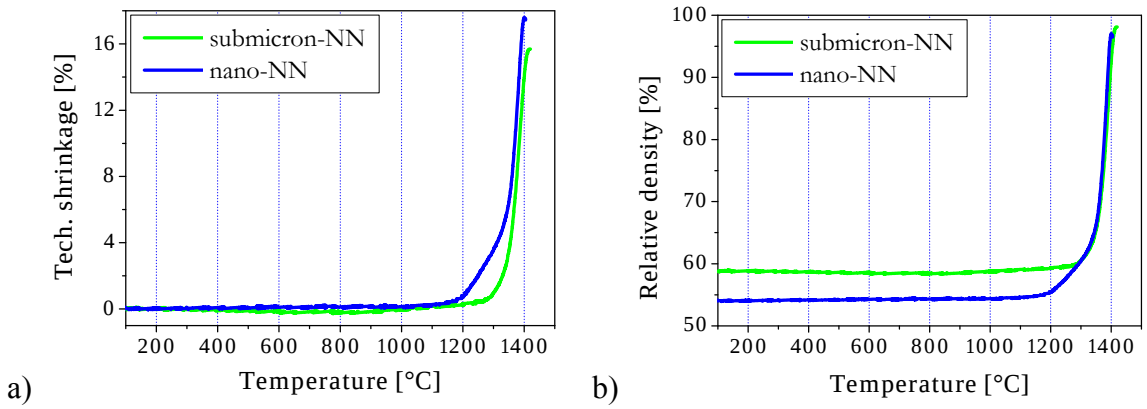

Figure 4.10: Shrinkage behaviour of the submicron-NN and nano-NN compacts during heating with a heating rate of 10 K/min. The relative green density of the samples was 58.8 % and 54 % for the submicron-NN and nano-NN, respectively.

The highest densification rates in both powder compacts were observed in the temperature region between 1340 °C and 1390 °C, which corresponds to homologous sintering temperatures (T_H^S; see Section 1.2.1) between 0.95 and 0.99. These values are considerably higher than in most single-oxide ceramic materials: Al_2O_3 (0.83), TiO_2 (0.76), MgO (0.61) or CaO (0.59) (Bron, 1964), or some typical perovskites: $BaTiO_3$ (0.77–0.85) or $SrTiO_3$ (~0.67) (Chang et al., 1995, Wang et al., 2006). Interestingly, also low-melting-point materials, such as K_2O (0.56), Na_2O (0.57) or Li_2O (0.58), have a much lower T_H^S. The T_H^S was reported to have an approximately linear dependence on the crystal-lattice energy, as presented in **Figure 4.11** (Bron, 1964). Although probably simplified, this relationship was claimed to be valid for any oxide and should enable an estimation of the sintering temperature, supposing that the lattice energy is known. The values for two typical perovskites, $SrTiO_3$ and $BaTiO_3$, are added to **Figure 4.11** for comparison (Akhtar et al., 1995, Lewis and Catlow, 1986). The reported calculated values of the lattice energy of $NaNbO_3$ are between 789 kJ/mol and 886 kJ/mol (Lehl, 1973). Therefore, according to Bron, the value of T_H^S should be around 0.55. The latter is significantly lower than the observed T_H^S between 0.95 and 0.99, see **Figure 4.11**. The observation indicates that the sintering behaviour of $NaNbO_3$ is different from the above-listed ceramic systems. Similar behaviour was also observed for $KNbO_3$, although the reported lattice energies (720–789 kJ/mol) and T_H^S (0.88–0.98) are slightly lower, as compared to $NaNbO_3$ (Kodaira et al., 1982, Lehl, 1973).

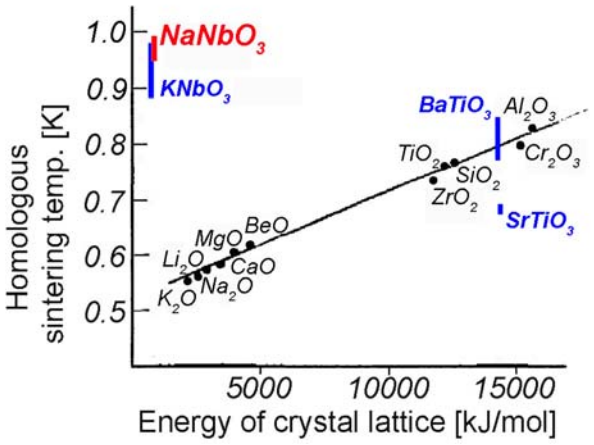

Figure 4.11: Dependence of the homologous sintering temperature on the crystal-lattice energy for different simple oxides (Bron, 1964) and perovskites (Akhtar et al., 1995, Chang et al., 1995, Kodaira et al., 1982, Lehl, 1973, Lewis and Catlow, 1986, Wang et al., 2006). The values for $NaNbO_3$ are added for comparison.

In order to investigate the microscopic behaviour of both powders upon sintering, we followed the microstructure development during the heating. Three compacts of each powder were heated at a rate of 10 K/min and quenched from the selected temperatures: 1100 °C, 1320 °C, and 1370 °C. The FE-SEM images of the fracture surfaces of the quenched samples are collected in **Figure 4.12**; the green sample is added as a reference. In both cases no densification was observed during the first heating stage between room temperature and 1100 °C and the relative density remained the same as in the green compacts. However, considerable coarsening occurs since the grains grow from an initial 0.17 µm to 0.29 µm in the case of the submicron-NN and from an initial 0.03 µm to 0.17 µm in the case of the nano-NN. Besides grain coarsening, this stage is characterized by the formation of necks between the individual particles. Upon further heating both materials start to densify according to the shrinkage curves presented in **Figure 4.10**. At 1320 °C both samples reach a relative density of about 62–64 %, while the grain size is 0.8 µm for the submicron-NN and 1.0 µm for the nano-NN. Upon further heating both samples densify more rapidly and reach a relative density of 72 % (submicron-NN) and 78 % (nano-NN) at 1370 °C. The slightly higher density of the nano-NN sample at this temperature can be explained by the shifted densification curve, which means that a similar microstructure state would be reached a few degrees lower in the case of the nano-NN. During this densification step considerable grain growth was also observed since the grain size of both samples was increased to around 1.7 µm.

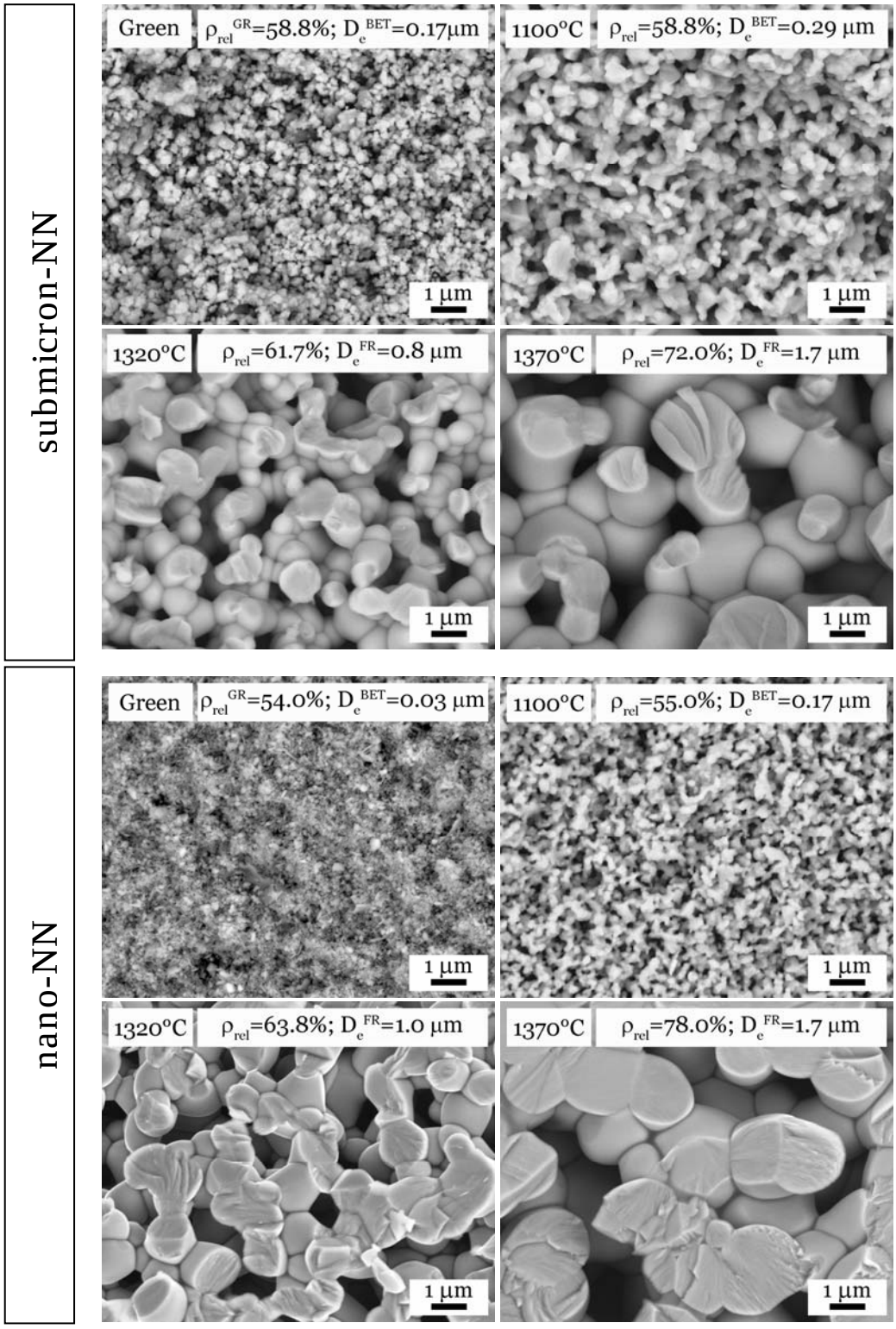

Figure 4.12: FE-SEM images of the fracture surfaces of submicron-NN and nano-NN samples heated at 10 K/min and quenched from 1100 °C, 1320 °C, and 1370 °C. The images of the green samples are added for comparison.

In order to track the competing effects of grain growth and densification during the sintering process, it is convenient to plot the above results in the form of the microstructure-development trajectories (Section 1.2.1), as presented in **Figure 4.13**. Even though both samples have strongly different initial particle sizes, these differences vanish when they reach the main densification stage and the trajectories of both samples

almost coincide with each other. This indicates the dominance of the grain growth processes during the initial sintering stage. By the time the densification processes get activated both samples already had similar grain sizes. It should be noted that here we present only the results for the heating rate of 10 K/min; however, similar results were also obtained for both 5 K/min and 15 K/min heating rates. A comprehensive discussion about the activation of different processes and the sintering mechanisms will be given in the next section.

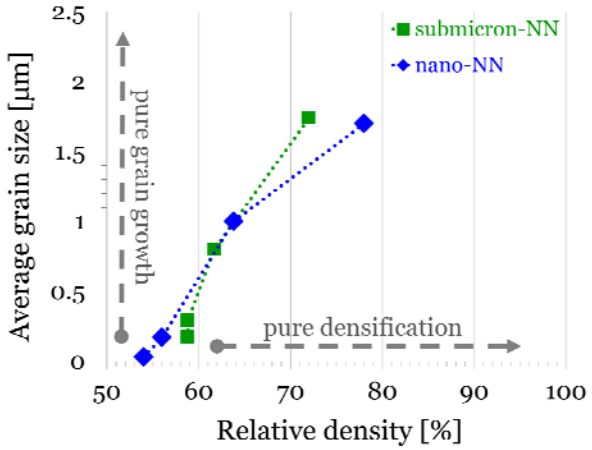

Figure 4.13: The grain size/density trajectories for the submicron-NN and nano-NN powder compacts during heating with a rate of 10 K/min. The dashed grey arrows indicate the trajectories for pure grain growth and pure densification.

In 1981, Harmer and Brook suggested that the grain growth of Al_2O_3 may be suppressed by the use of rapid heating rates (Harmer and Brook, 1981). This fast firing technique should enhance the densification mechanisms, which in many cases have higher activation energies and are therefore activated at higher temperatures, while bypassing grain growth mechanisms with typically lower activation energies. This technique was later successfully applied to the sintering of other materials, such as $BaTiO_3$ (Mostaghaci and Brook, 1981) and ZrO_2 (Kim and Kim, 1992). In order to investigate the effect of the heating rate on the microstructure-development of $NaNbO_3$ a series of nano-NN compacts was heated with different heating rates up to 1370 °C and subsequently quenched in air in order to preserve the high-temperature state. The applied heating rates were 10 K/min, 50 K/min, 100 K/min, and 200 K/min, and the corresponding FE-SEM images of the fracture surfaces are presented in **Figure 4.14**. The sample heated with 10 K/min had an average grain size of 1.7±0.5 µm and a relative density of 78 %. Upon increasing the heating rate a decrease of the average grain size was observed; however, in addition the relative density decreased. Plotting these results into the relative density vs. grain size diagram (**Figure 4.15**) reveals that although a smaller grain size is obtained when using the higher heating rates (100 or 200 K/min) the microstructure-development trajectory remains the same, meaning that the microstructure development is similar to the case of conventional heating with 10 K/min. Therefore, we can conclude that the heating rate does not influence the microstructure development of $NaNbO_3$ in the investigated region between 10 K/min and 200 K/min. Moreover, these results indicate that the activation energy for the grain growth processes is low. This will be further investigated and discussed in the following section.

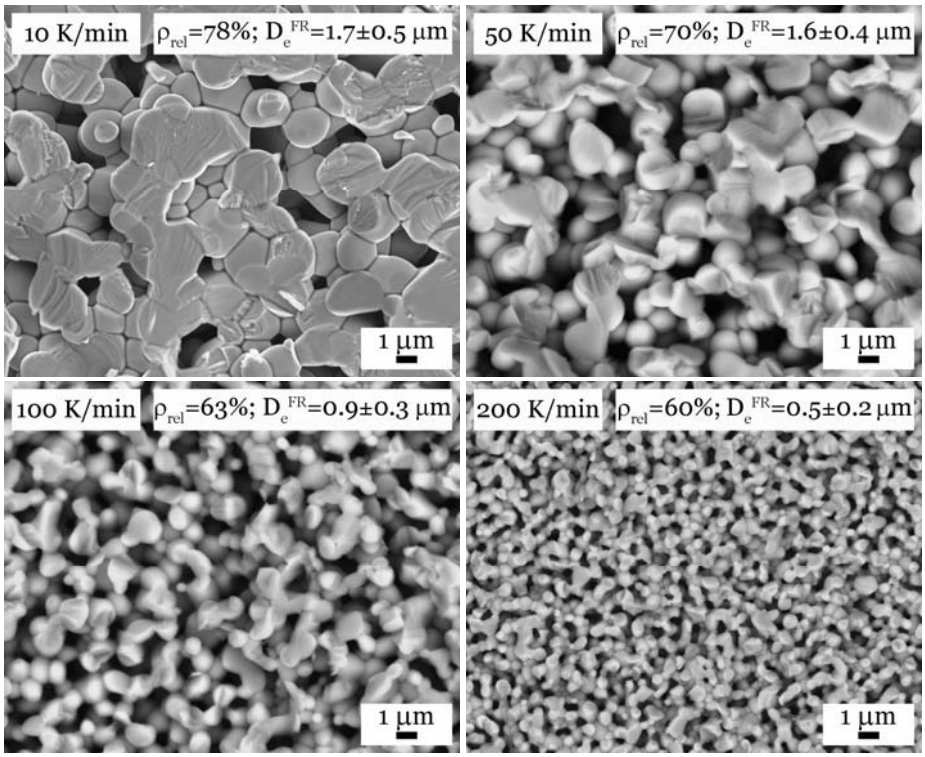

Figure 4.14: FE-SEM images of the fracture surfaces of nano-NN samples heated with different heating rates to 1370 °C and quenched in air.

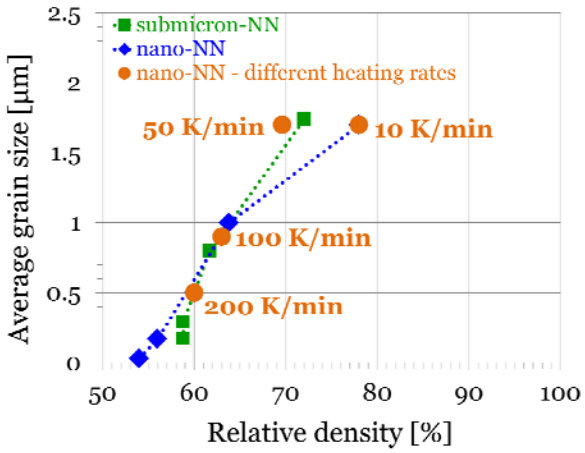

Figure 4.15: The grain size/density trajectory of the nano-NN powder compacts heated with different heating rates to 1370 °C (circles), as compared to the trajectories of the submicron-NN and nano-NN heated with 10 K/min (squares and diamonds).

4.2.2 Sintering Mechanisms

4.2.2.1 Initial Sintering Stage

The microstructure-development trajectories observed in ceramic systems are typically exponential functions with rapid densification and negligible grain growth during the intermediate sintering stages and considerable grain growth once a critical density is reached (Kanters et al., 2000, Polotai et al., 2005, Wang and Raj, 1990). However, in our case the microstructure-development trajectories for the $NaNbO_3$, presented in **Figure**

4.15, revealed a different behaviour as compared to the literature reports for other ceramic materials, such as, e.g., Al_2O_3 or $BaTiO_3$ (see Section 1.2.1). Note that agglomerates were not observed in the green samples (BET, FE-SEM) and therefore the initial-stage coarsening due to agglomeration, as suggested by Lange (Lange, 1984), could be excluded. The rapid grain growth during the initial sintering stages, well before the onset of densification, indicates the early activation of non-densifying sintering mechanisms, such as surface diffusion and/or evaporation-condensation (Sections 1.2.2 and 1.2.3.1). In order to exclude the presence of the densifying mechanisms, we performed an isothermal experiment, whereby a nano-NN compact was rapidly heated to 800 °C and isothermally sintered in an optical dilatometer for 1 h. The result is presented in **Figure 4.16**. Since no shrinkage of the sample was observed we can confirm the absence of the densifying material transport mechanisms in the temperature region between RT and 800 °C.

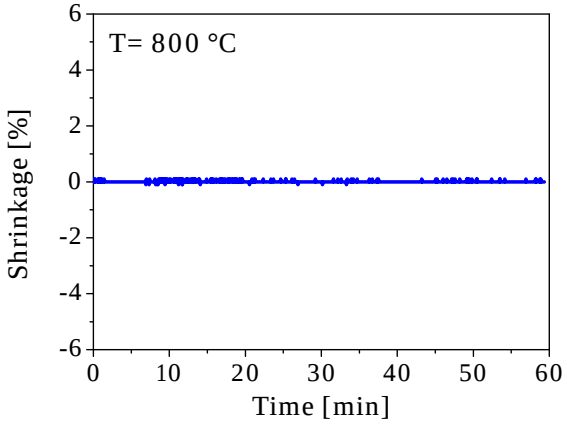

Figure 4.16: Shrinkage of a nano-NN powder compact during isothermal sintering at 800 °C.

In order to determine the initial stage sintering mechanism in $NaNbO_3$, we followed the specific surface area reduction during isothermal sintering of nano-NN compacts. This method was proposed by German and Munir in 1976 and successfully applied to determine the mass-transport processes in materials such as Al_2O_3, TiO_2, B, and others (German and Munir, 1976). According to the authors the material transport mechanism can be identified by analysing the change of the specific surface area reduction ($\Delta S/S_0$) with time. The generalized expression for sintering kinetics was given as:

$$\left(\frac{\Delta S}{S_0}\right)^{\gamma} = t \cdot C \cdot \exp\left(-\frac{Q_A}{R \cdot T}\right) \tag{4.1}$$

where ΔS is the change of the specific surface area, S_0 is the initial specific surface area, γ is the specific surface area reduction exponent, which is directly related to the sintering exponent n ($\gamma=n/2$), t is the sintering time, C is a constant, and Q_A is the activation energy for the active material transport mechanism. Plotting $\log(\Delta S/S_0)$ versus $\log(t)$ gives the value of the specific surface area reduction exponent γ, which can be used to identify the dominant sintering mechanism using **Table 1.2**. It should be noted that in the described model the particles are assumed to be monodispersed spheres and that the method is only valid until neighbouring necks impinge each other, which is at $\Delta S/S_0 \approx 0.5$.

We prepared a series of nano-NN compacts and sintered them isothermally for 5 min, 30 min, and 60 min at three different temperatures: 500 °C, 550 °C and 600 °C. The specific surface areas before and after the sintering step were measured by the BET method and the results are presented in **Figure 4.17**. As expected the specific surface area

decreased with increasing sintering time and sintering temperature. According to German and Munir the sintering mechanism can be identified from the slopes of the linear fits in **Figure 4.17**. The data points were linearly fitted and from the slopes we obtained the values $\gamma = 3.4 \pm 0.8$ and $n = 6.8 \pm 0.8$ for the sintering exponents, which according to **Table 1.2**, indicate the presence of surface diffusion as the dominant sintering mechanism during the initial stage of sintering of the nano-NN. This observation is also consistent with the fact that among all the material transport mechanisms, surface diffusion is expected to depend the most on particle size and is thus enhanced as the particle size is decreased (see analytical sintering models; **Equation 1.7** and **Table 1.2**)

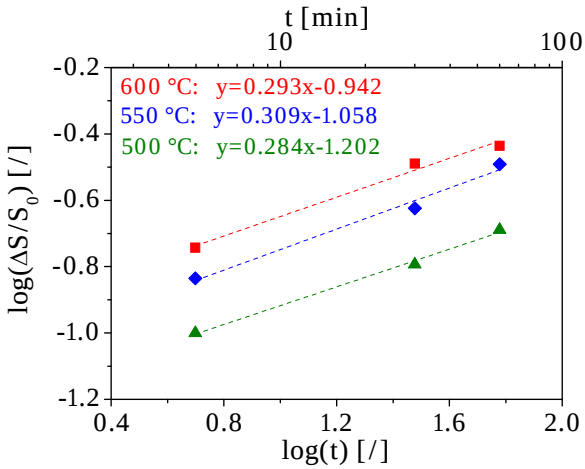

Figure 4.17: Kinetic data for the surface area reduction during isothermal sintering of nano-NN powder compacts at three different temperatures. The data points were fitted with linear functions (dashed lines) and the corresponding equations for each temperature of isothermal sintering are given.

Many authors reported high volatility of the alkaline components in alkaline niobates at increased temperatures (Malič et al., 2008, Wang et al., 2008, Zhen and Li, 2006), which would suggest the increased activity of the evaporation-condensation material transport mechanisms. In order to estimate the volatility of Na during heating we used the IVTANTHERMO EQUI-CALC32 equilibrium calculation program, which was supplied with experimental data obtained from the Knudsen effusion mass spectrometry (KEMS) measurements (Popovič A., private communication) (details in Section 3.2.2). The calculated vapour pressure of Na over pure $NaNbO_3$ as a function of temperature in an air atmosphere is presented in **Figure 4.18**. During the initial sintering stage (500–600 °C) the calculated vapour pressure of Na over $NaNbO_3$ is in the range of $6 \cdot 10^{-19}$ to $6 \cdot 10^{-16}$ bar, which is indeed extremely low. This result supports the exclusion of material transport via the vapour phase during the initial sintering stages in $NaNbO_3$; however, we have to keep in mind that this calculation is only accurate for equilibrium conditions and a flat ideal surface.

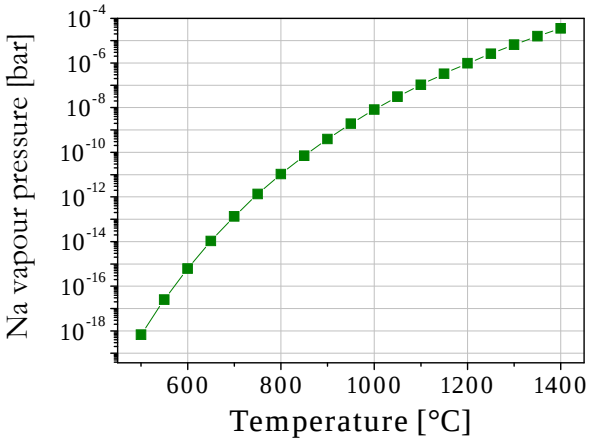

Figure 4.18: Calculated equilibrium vapour pressure of Na over pure $NaNbO_3$ in air atmosphere, as calculated by the IVTANTHERMO EQUI-CALC32 equilibrium calculation program using experimental data from KEMS measurements (Popovič A., private communication).

Figure 4.19 plots the surface area reduction data from **Figure 4.17** against the inverse temperature. According to the model of German and Munir, the slope of this curve equals the ratio Q_A/γ from which we can calculate the activation energy, assuming that the material transport mechanism is known. For the analysis of nano-NN powder compacts the model gives a surface diffusion activation energy of about 50–60 kJ/mol. This value is almost an order of magnitude smaller than the activation energies for surface diffusion in other ceramic systems (**Table 1.1**). The low value of the activation energy may explain the different behaviour of the microstructure-development trajectories (**Figure 4.15**) – since the activation energy is low the surface diffusion gets activated early during the sintering process, and since this is a non-densifying material transport mechanism it contributes only to the grain growth, while densification does not occur. Even in the case when higher heating rates (100 K/min or 200 K/min) were applied, grain growth was observed, which also confirms the low activation energy of the surface diffusion in this material.

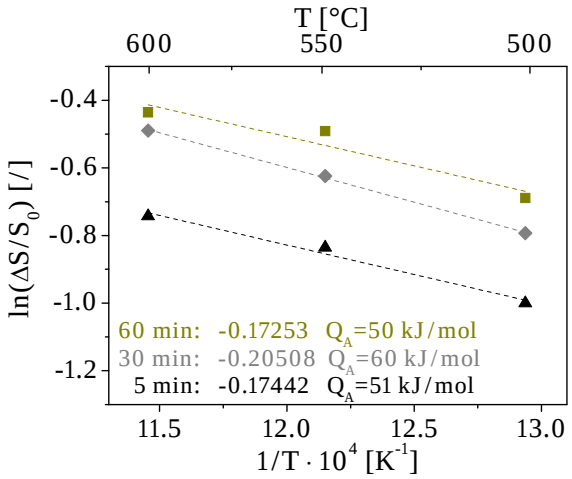

Figure 4.19: Surface area reduction data plotted against inverse temperature. The data points were fitted with linear functions and the corresponding slopes and calculated activation energies are given.

We believe that the low activation energy for surface diffusion originates from two main sources: the intrinsic physical properties of $NaNbO_3$ (low crystal-lattice energy; see

section 4.2.1) and the extrinsic contributions, such as the small particle size and various defects (evidenced by the XRD line-broadening analysis), which are introduced by the milling process. In our experiments, we were not able to distinguish between these two effects and thus the main cause for the low activation energy cannot be unambiguously determined. Due to experimental limitations, we were not able to perform the same surface area reduction analysis and estimate the activation energy for the submicron-NN powder, which would enable us to compare powders with different average particle sizes and microstrains. The following reasoning supports the hypothesis that the low activation energy for surface diffusion of $NaNbO_3$ is not related to the milling process. In 2005, Shiratori et al. prepared $NaNbO_3$ nanopowders using the microemulsion-mediated synthesis (Shiratori et al., 2005). Since this precipitation method does not require any milling steps, it is assumed that the powders had a much smaller quantity of microstrains (if any), as compared to our case. In order to prepare the powders with different particle sizes, the as-synthesized powder with an average particle size of 30 nm was annealed at different temperatures between 400 °C and 1000 °C. The average particle size increased upon increasing the annealing temperature: 90 nm at 400 °C, 180 nm at 600 °C, 230 nm at 700 °C, and above 700 nm at 900 °C. This result suggests that the low-temperature coarsening of the $NaNbO_3$ is related to the small particle size and/or to the low crystal-lattice energy.

The above results could explain the difficulties in obtaining dense $NaNbO_3$ ceramics with small grain sizes (below 1–2 μm), which are reported in the literature. The non-densifying mechanisms, such as surface diffusion, do not only increase the grain size, but also reduce the curvature of the neck surface, which directly reduces the driving force for sintering, and therefore reduces the rate of the densifying mechanisms (Rahaman, 2003). In addition these results explain why special sintering techniques, such as two-stage sintering (Chen and Wang, 2000), were not successful in the case of $NaNbO_3$ (not shown in this work) – this method aims at suppressing the grain growth in the final sintering stage; however, it cannot prevent grain growth during the initial stages.

Although our experiments were carried out only on $NaNbO_3$, we believe that similar sintering mechanisms should also be active in other alkaline niobates, e.g., $(K,Na)NbO_3$.

4.2.2.2 Intermediate and Final Sintering Stages

Upon heating the submicron-NN and nano-NN powder compacts above 1280 °C and 1180 °C, respectively, we observe the onset of densification (**Figure 4.10**), which indicates the activation of another material transport mechanism. Obviously, it should be one of the mechanisms that contribute to densification, such as grain-boundary diffusion or lattice diffusion (Section 1.2.3.1). Note that viscous flow is not likely to occur in ceramic materials and will therefore not be discussed.

According to the sintering models for the intermediate sintering stage, proposed by Coble, the densification rate is described by combining **Equations 1.9** and **1.10** and is written in a more general form as (Coble, 1961):

$$\frac{d\rho}{dt} = C \cdot \frac{D}{G^m} \tag{4.2}$$

The grain size exponent *m* from **Equation 4.2** is dependent on the dominant material transport mechanism and has values of 3 and 4 for the cases of lattice- and grain-boundary diffusion-controlled densification, respectively. Since during this sintering stage densification and grain growth are simultaneously active, both parameters should be measured during an isothermal experiment. If the logarithm of the densification rate is plotted versus the logarithm of the grain size, then the grain size exponent *m* can be

determined from the slope of the data line. This procedure was successfully applied to determine the dominant sintering mechanisms, for example, in pure and MgO-doped Al_2O_3 (Berry and Harmer, 1986).

The shrinkage data for the isothermal sintering of the nano-NN powder compact at 1350 °C are presented in **Figure 4.20a**, while **Figure 4.20b** represents the average grain sizes, as measured after 10 min, 30 min, 60 min, and 90 min of isothermal sintering. The material densifies rapidly during the initial 10 minutes, where a relative density of 87.4 % and an average grain size of 2.1±0.8 μm are reached. A further increase in the sintering time did not significantly contribute to the densification and the final density achieved after 90 minutes was 92.7 %, while the average grain size increased up to 4.5±3.2 μm. The data from **Figure 4.20** were used as the input for the intermediate sintering stage model proposed by Coble (Coble, 1961) and the result is presented in **Figure 4.21**, where the logarithm of the densification rate is plotted versus the logarithm of the grain size. The lines for pure lattice diffusion (m=3) and pure grain-boundary diffusion (m=4) according to Coble's model are added for comparison. The data points obtained from our experiments could be fitted with a line with a slope of 4.6±1, which indicates that the densification at this temperature is grain-boundary diffusion controlled. The dominance of the grain-boundary diffusion is related to the use of a nano-sized powder. Similar observations were made by Kang and Jung for Al_2O_3, who showed that the grain-boundary diffusion dominates over the lattice diffusion when the powders with sizes below 0.8 μm were used (Kang and Jung, 2004).

It should be noted that the presented method for determining the dominant material transport mechanism is subjected to potential errors, such as broad grain-size distributions, the possible simultaneous activation of more than one mechanism, and the assumed rapid specimen heating. Even though these phenomena can contribute to errors, this technique can give valuable qualitative information about the sintering process.

Another factor should be considered when sintering $NaNbO_3$. According to the thermodynamic calculations presented in **Figure 4.18** the vapour pressure of Na over $NaNbO_3$ becomes increasingly important once the temperature is increased above 1000–1200 °C and reaches a value of $1.6 \cdot 10^{-5}$ bar at 1350 °C, which is more than 10 orders of magnitude higher than the pressures during the initial sintering stages. This would suggest that the material transport via the vapour phase becomes increasingly important upon increasing the temperature; however, on the other hand, this phenomenon is limited only to the free surfaces, and their total area decreases when the processes of coarsening and densification progress during sintering. The effect of the Na vapour pressure on the sintering of $NaNbO_3$ at high temperatures therefore remains an open question and requires a detailed analysis, which is beyond the scope of this work.

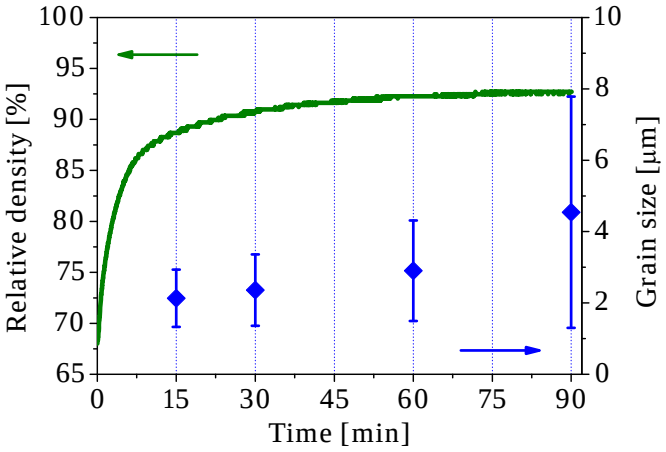

Figure 4.20: The relative density and the average grain size during isothermal sintering of a nano-NN powder compact at 1350 °C.

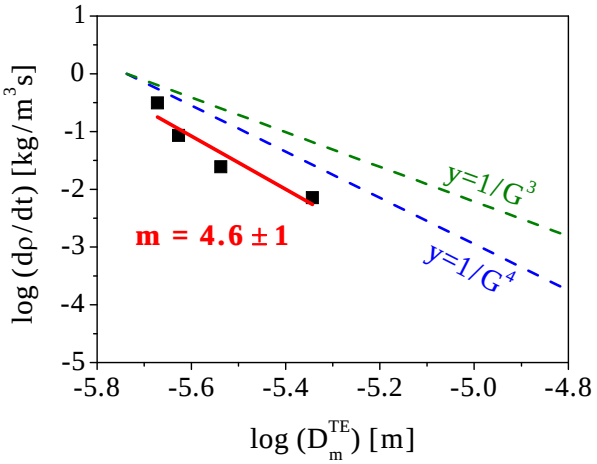

Figure 4.21: The densification rate as a function of the average grain size for the isothermal sintering of nano-NN at 1350 °C. The black squares mark the data points, while the red line represents the linear fit with a slope of 4.6±1. The green and blue dashed lines represent Coble's intermediate stage sintering model for lattice (m=3) and grain-boundary (m=4) diffusion, respectively (Coble, 1961).

4.2.3 Pressure-Assisted Sintering of Nano-NN Powder Compacts

One of the goals of the present work was to prepare dense $NaNbO_3$ ceramics with submicron-sized grains, which would be further used for the phase-transition studies. However, as presented in Sections 4.2.1 and 4.2.2, this goal could not be achieved by conventional sintering techniques due to the low activation energy for surface diffusion, which was activated already during the early sintering stages and resulted in rapid grain growth with only low densification. Since neither the increased heating rates nor the different green states of the samples were able to change the microstructure-development trajectory, and thus reduce the grain growth, we decided to look for an alternative sintering technique.

The problem of inadequate densification during sintering has often been observed in ceramics and one of the solutions was to apply external pressure to the powder system during heating, which is the basic concept of hot pressing, hot isostatic pressing, and hot

forging techniques (Rahaman, 2003). The additional sintering driving force, provided by the external pressure, is larger than the intrinsic driving force, provided by the surface curvature of the powder particles. The analytical models for the sintering process under applied pressure were developed by Coble in 1970 (Coble, 1970). The external pressure was found to enhance the densifying material transport mechanisms, while the non-densifysing mechanisms were not affected. In addition to diffusion, particle rearrangement and grain-boundary sliding were found to contribute to the densification during the initial sintering stage.

In order to investigate the effect of the external pressure on the sintering process of $NaNbO_3$, we performed two sets of experiments using the pressure-assisted sintering technique described in Section 3.2.3. All the experiments were performed on the nano-NN powder, which was compacted using an isostatic pressure of 740 MPa, resulting in green densities of about 68 %. These preparation conditions were chosen in order to reduce the initial amount of free surfaces. In the first set of experiments, the samples were heated with a constant rate of 10 K/min to the sintering temperature at which we applied the external pressure, while in the second set of experiments, the external pressure was applied already at the beginning of the experiment, prior to the heating stage. The obtained relative densities of both sets of experiments are presented in **Figure 4.22**, while the FE-SEM images are shown in **Figure 4.24**. In the case when the external pressure was applied after the heating stage, we obtained relative densities and average grain sizes of 75 % and 0.19±0.09 µm at 1100 °C and 89 % and 0.61±0.24 µm at 1150 °C, respectively. As expected, the obtained relative densities were much higher in the case when the external pressure was applied before the heating stage, i.e., at the beginning of the experiment. The best results, a relative density of 98 % and an average grain size of 0.70±0.29 µm, were obtained after sintering for 6 h at 1150 °C.

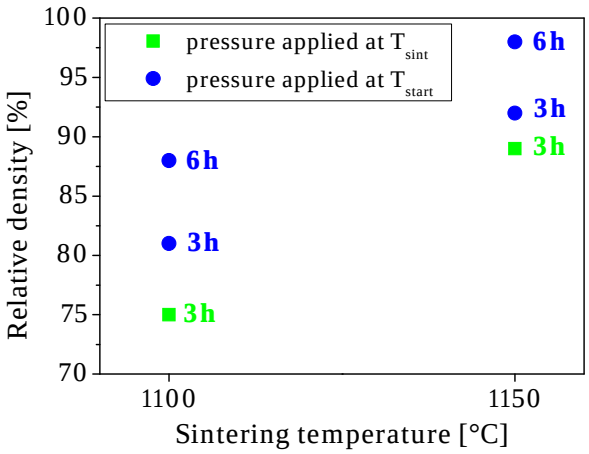

Figure 4.22: Relative densities of the nano-NN samples sintered at different temperatures and for different times using pressure-assisted sintering. The squares mark the samples where the external pressure was applied once the final temperature was reached, while the circles mark the samples where the external pressure was applied also during heating.

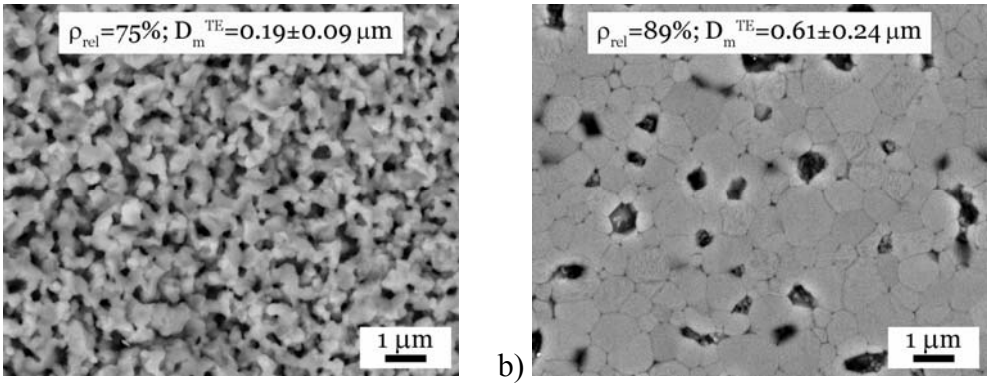

Figure 4.23: FE-SEM images of the nano-NN samples sintered at 1100 °C (a) and 1150 °C (b) for 3 h using pressure-assisted sintering, whereby the external pressure was applied once the samples reached the final temperature.

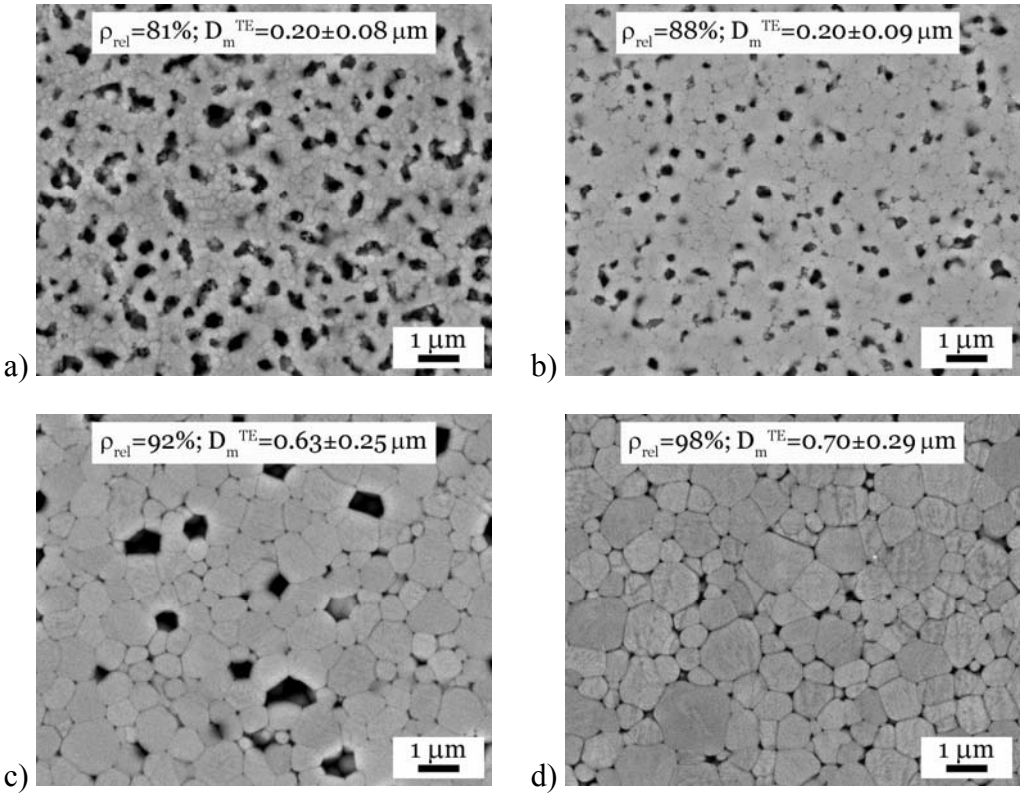

Figure 4.24: FE-SEM images of the nano-NN samples sintered at 1100 °C for 3 h (a) or 6 h (b) and at 1150 °C for 3 h (c) or 6 h (d) using pressure-assisted sintering, whereby the external pressure was applied also during heating.

The comparison of the results of pressure-assisted sintering and conventional sintering of $NaNbO_3$ is presented in **Figure 4.25**. We can observe that the microstructure-development trajectories for the samples sintered with external pressure are very different, as compared to the conventionally sintered samples. The grain growth during the initial sintering stages was successfully reduced and the average grain size did not exceed 0.61 μm until a relative density of 90 % was reached. The obtained average grain sizes were even smaller in the samples where the external pressure was applied upon heating, while the relative densities were higher, which can be due to the additional rearrangement of the particles during the heating stage. The enhanced densification during the initial sintering stages resulted in early closure of the microstructure, as

compared to conventional sintering. Thus the total free surface area was much smaller and the surface diffusion was partially hindered. Since the free surface area was smaller, the total grain-boundary area must have been larger, as compared to the conventionally sintered samples. The larger grain-boundary area could provide material transport paths for grain-boundary diffusion, which, being a densifying material transport mechanism, enhanced the densification. Thus the pressure-assisted sintering proved successful in the preparation of submicron-sized $NaNbO_3$ ceramics with high relative densities.

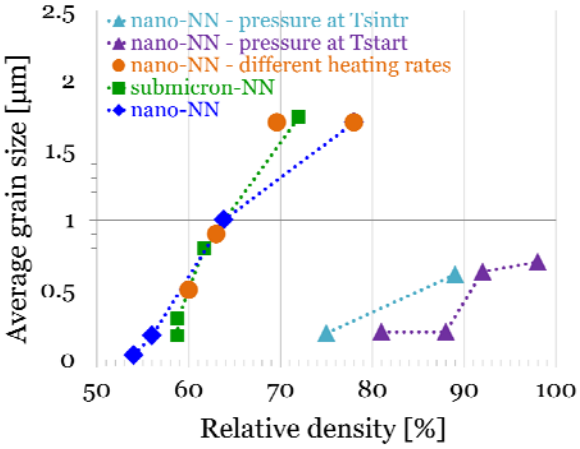

Figure 4.25: The microstructure-development trajectory of the nano-NN compacts sintered with the aid of the external pressure (triangles), as compared to the results of the conventional sintering presented in Section 4.2.1.

4.2.4 Abnormal Grain Growth in $NaNbO_3$

In order to prepare ceramics with coarse microstructures, we decided to use the submicron-NN powder and the conventional sintering techniques. The samples were therefore heated with a constant rate of 5 K/min up to 1350 °C and isothermally sintered for different periods of time: 0, 5, 10, 15, 30, and 120 min. Subsequently, the samples were air-quenched and the polished and thermally etched microstructures are presented in **Figure 4.26**, while the mean grain sizes and size distributions are shown in **Figure 4.27**. The mean grain sizes of the 0 min and 5 min samples were 2.5±1.1 µm and 2.7±1.2 µm, respectively, while the pores were of irregular shapes and were distributed exclusively at the grain junctions. Upon increasing the sintering time to 10 min the mean size of the grains did not change much, only the grain size distribution slightly broadened. During the first 10 min of isothermal sintering the pores moved together with the grain boundaries and inhibited the grain growth. After 15 min the average size of the grains remained at around 2.8 µm; however, a few large grains of several 10 µm were observed. The appearance of the large grains can be explained by the increase of the grain-boundary migration velocity, which at this point exceeded the pore migration velocity (Brook, 1969) (see Section 1.2.4.3). The reason for this is the decrease in the amount and size of the pores as the sintering time is increased (**Figure 4.28**). The process of the pore/grain-boundary separation created the conditions for the onset of abnormal grain growth. A typical situation is shown in **Figure 4.29**, where a distorted pore, which was dragged along by the grain boundary, is being separated from the boundary to be entrapped inside the large grain on the left. With increasing the sintering time, the grains grew very rapidly and after 30 min the mean grain size increased to 35.6±32.0 µm. At this point the relative density reached a value of about 95–96 % and did not change much with any further increase of the sintering time. This can be explained by the increased diffusion paths due

to the occurrence of the large grains, which reduce the rate of densification (Section 1.2.4). After 120 min the majority of the remaining pores on the grain boundaries disappeared and the mean grain size increased to 55.3±31.8 μm.

The above results indicate that the pore/grain-boundary separation conditions (Section 1.2.4.3) during sintering of $NaNbO_3$ occurred after heating the samples at 1350°C for 10–15 min, resulting in abnormal grain growth and a coarse-grained microstructure.

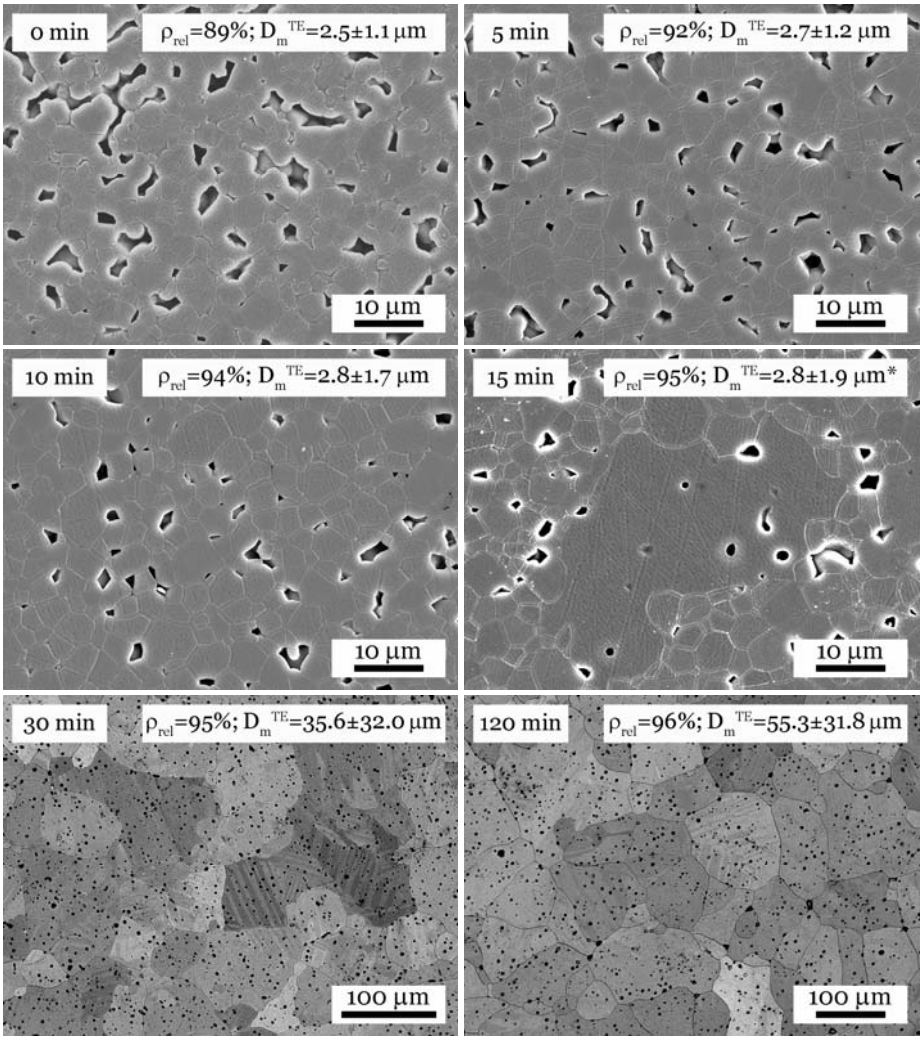

Figure 4.26: SEM images of polished and thermally etched microstructures of $NaNbO_3$, sintered using conventional sintering methods: heating with a constant heating rate of 5 K/min and holding isothermally at 1350 °C for different periods of time (marked in images). Note the change of the magnification for the "30 min" and "120 min" samples. The asterisk marks that besides the reported value also some large grains were observed.

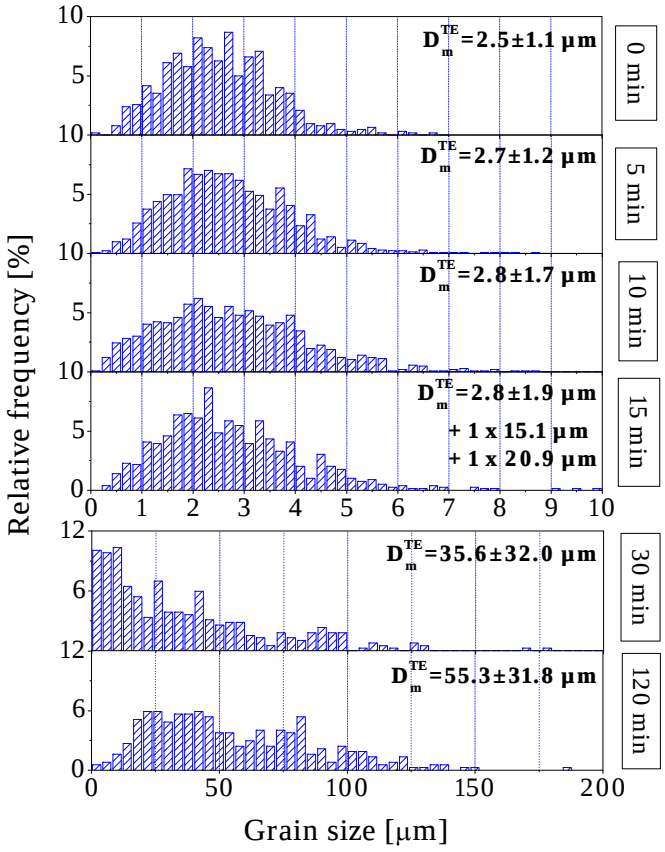

Figure 4.27: Mean grain sizes and grain size distributions of the $NaNbO_3$ samples after different sintering times at 1350 °C. Note the change of scale for the "30 min" and "120 min" samples.

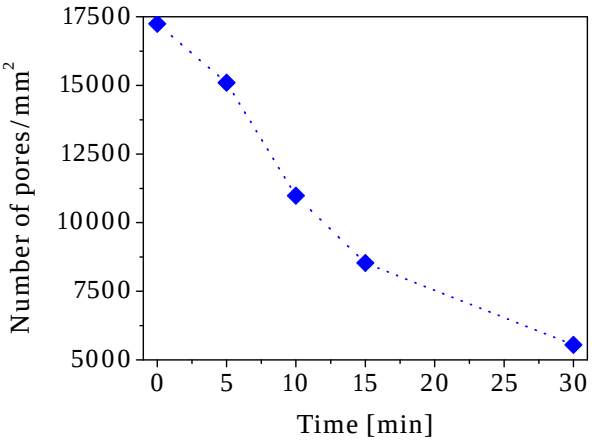

Figure 4.28: Number of intergranular pores per unit area versus time of sintering for $NaNbO_3$ samples at 1350 °C, as determined from the SEM images.

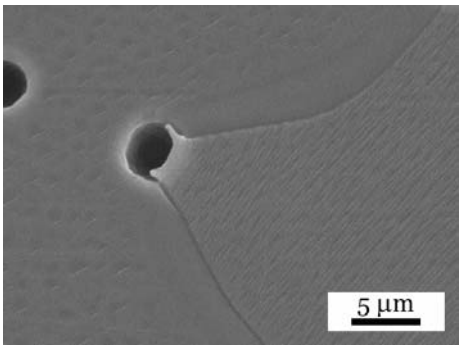

Figure 4.29: The separation of the pore from the grain boundary in $NaNbO_3$ during sintering (sintering conditions: 2 h at 1350 °C; SEM image).

4.2.5 Summary

We studied the sintering behaviour of submicron-NN and nano-NN powder compacts. During the heating stage of conventional sintering both samples behaved similarly, although the densification process started earlier in the case of nano-NN. Both samples exhibited similar microstructure-development trajectories, revealing the dominance of the grain growth (coarsening) processes during the initial stage, while densification occurred only during later stages.

In order to understand the observed microstructure development, we studied the material transport mechanisms during individual sintering stages. These studies were performed on nano-NN powder compacts. By tracking the specific surface area reduction during the initial sintering stage we found the surface diffusion to be the dominant material transport mechanism. The activation energy for this diffusion mechanism was estimated to be very low, around 50–60 kJ/mol, which is in agreement with the rapid grain growth observed during the initial sintering stage. In addition, the presence of non-densifying mechanisms, such as surface diffusion, reduces the driving force for sintering and therefore reduces the rate of the densifying mechanisms. This may be the reason for the often reported, poor densification of $NaNbO_3$ and other alkaline niobates.

Once the temperature exceeded 1280 °C or 1180 °C, for the submicron-NN and nano-NN, respectively, the densifying mechanisms were activated. According to the results from the densification and grain growth analysis at 1350 °C the densification is controlled by grain-boundary diffusion.

In order to prepare dense $NaNbO_3$ ceramics with submicron sized grains, we had to suppress the initial grain growth and enhance the densification processes. Therefore, we decided to use the pressure-assisted sintering technique. The external pressure provided an additional driving force for densification, which resulted in a drastic change of the microstructure-development trajectory. Even at about 200 °C lower temperatures, as compared to conventional sintering, we prepared $NaNbO_3$ ceramics with a relative density of 98 % and an average grain size of 0.7±0.3 µm. The enhanced densification during the initial sintering stage resulted in a reduction of the total free surface area and thus partial prevention of the surface diffusion. On the other hand, the increased grain-boundary area provided paths for material transport via grain-boundary diffusion and thus enhanced densification. In addition, particle rearrangement and grain-boundary sliding may have contributed to the densification during the initial sintering stage.

In order to prepare coarse-grained $NaNbO_3$ ceramics, we sintered the submicron-NN by conventional sintering methods. Abnormal grain growth, which occurred after sintering the samples for 10–15 minutes at 1350 °C, was related to the observed decreased

amount of pores and a reduction of their sizes, which resulted in pore/grain-boundary separation. Dense $NaNbO_3$ ceramics with an average grain size of 55.3±31.8 μm and a relative density between 95–96 % were obtained after sintering for 120 minutes at 1350 °C.

4.3 Phase-Transition Behaviour of $NaNbO_3$

This section reports and discusses the results obtained from the studies of the phase-transition behaviour of $NaNbO_3$, the complexity of which is described in the literature review in Section 1.3.2. The majority of the work was focused on the transitions between the antiferroelectric P and the ferroelectric Q phase. The first part is devoted to the re-examination of the temperature-induced phase transitions of $NaNbO_3$ ceramics, while the second part investigates the size-induced phase transitions found in $NaNbO_3$ powders and ceramics. In the third and the last part we report on the effect of the electric field on the phase transition between the antiferroelectric and ferroelectric phases.

4.3.1 Temperature-Induced Phase Transitions in $NaNbO_3$ Ceramics

Upon heating $NaNbO_3$ undergoes a complex sequence of phase transitions, as described in Section 1.3.2.2. Despite the extensive literature reports, many results regarding the phase stability and phase transition temperatures below 400 °C remain contradictive. Therefore, we first re-examined the temperature-induced phase-transition behaviour of the $NaNbO_3$ ceramics in the temperature range between RT and 700 °C by DSC, dielectric spectroscopy, and high-temperature XRD. Note that all the measurements in this Section were performed on coarse-grained $NaNbO_3$ ceramics, which in our case refers to samples with average grain sizes above 2 μm and relative densities above 96 %.

The DSC curve, obtained after heating the ceramic sample up to 700 °C, is presented in **Figure 4.30**. Four anomalies were observed and connected with the well-known phase transitions: 371.4 °C (*P*→*R*), 511 °C (*S*→*T(1)*), 564.7 °C (*T(1)*→*T(2)*), and 642.4 °C (*T(2)*→*U*). The temperatures are reported as the maxima of the DSC peaks. The presence of the antiferroelectric *P* phase at RT was confirmed by XRD and a more extensive XRD analysis will be given at the end of this section. The *R*→*S* transition, reported to occur in the vicinity of 480 °C, could not be detected. Note, however, that according to the literature, the space group during this transition remains the same (*Pnmm* SG No. 59) and the only change is the disappearance of the Nb displacement, i.e., the material undergoes a change from the antiferroelectric to the paraelectric state (Ahtee et al., 1972). This change is expected to be too small to be detected by the DSC method.

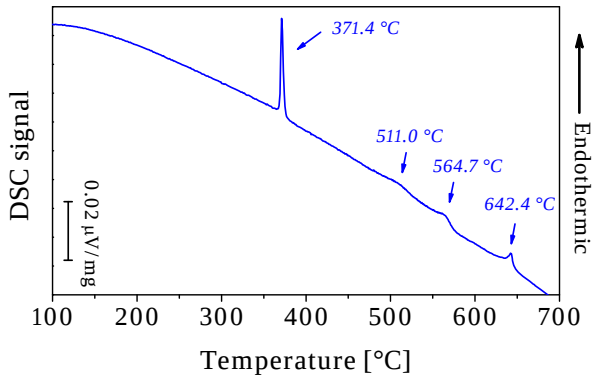

Figure 4.30: DSC curve of the coarse-grained ceramic sample upon heating. The numbers indicate the temperatures of the observed phase transitions, taken as the maxima of the peaks.

In addition, the phase-transition behaviour was studied by measuring the temperature dependence of the dielectric permittivity. Due to enhanced conductivity at higher temperatures we focused only on the temperature region between RT and 450 °C and the result is presented in **Figure 4.31**. The main anomaly with the peak onset at 357 °C and

the peak maximum at 374 °C was found to be frequency independent and was related to the *P*→*R* phase transition, which is in good agreement with the DSC results.

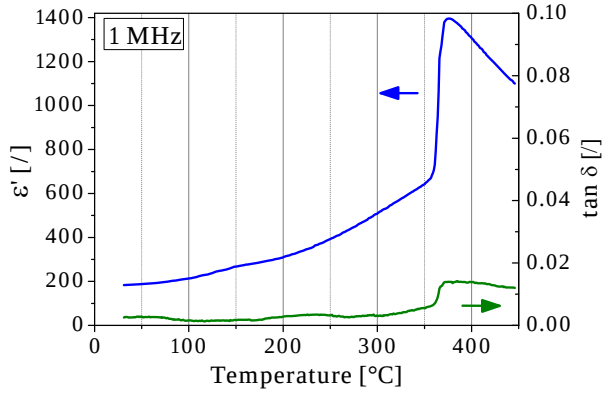

Figure 4.31: Temperature dependence of the real part of the dielectric permittivity and the loss tangent of coarse-grained $NaNbO_3$ ceramics, as measured upon heating.

Upon a closer look, another dielectric anomaly was observed around 150 °C (**Figure 4.31**), which was not detected by the DSC method. This anomaly was previously observed by some authors (Raevskii et al., 2000, Wang et al., 1996); however, it has not been widely accepted as a phase transition and the origin of the anomaly remains unclear. We have re-measured this temperature region over a wide frequency range, between 300 kHz and 1 MHz, and the results are presented in **Figure 4.32**. While the associated peak in *ε'(T)* was difficult to distinguish from the background, more information could be obtained from the temperature dependence of the imaginary part of the complex permittivity *ε''(T)*, which is shown in **Figure 4.32b**. The *ε''(T)* maxima were found to be frequency dependent, which excluded the existence of a phase transition in this temperature region (Ang et al., 2000, Pirc and Blinc, 2007).

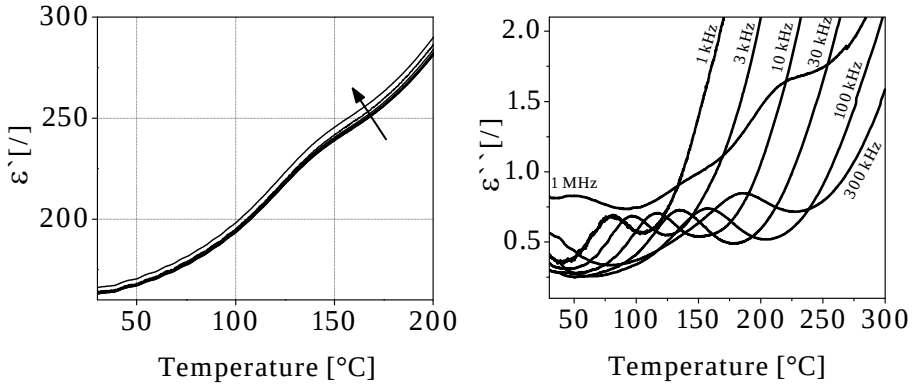

Figure 4.32: Enlarged region of the real (left) and imaginary (right) parts of the dielectric permittivity in the vicinity of 150 °C, measured at different frequencies between 300 kHz and 1 MHz. The arrow indicates the increase in frequency.

The DSC and dielectric measurements revealed merely the regions of stability for individual phases, but did not provide information regarding the nature of these phases. In order to determine the stability regions of the predicted phases and to get an insight into the structural changes, we performed a high-temperature XRD analysis of the coarse-grained $NaNbO_3$ ceramics. We focused only on the main *P*→*R* phase transition, which typically occurs around 360–370 °C and was also the most pronounced transition in the DSC and *ε'(T)* curves.

The XRD patterns were measured on a coarse-grained $NaNbO_3$ ceramic sample in the temperature range between RT and 450 °C. Using the crystallographic cards from the ICDD-PDF database we were able to describe the RT structure with the *P* phase (*Pbcm* space group No. 57; 01-073-0803), while the 450 °C structure was described with the *R* phase (*Pmmn* space group No. 59; 01-073-0298) (PDF-ICDD, 2011). This result is consistent with previous reports for the $NaNbO_3$ ceramics and single crystals (Megaw, 1974). The selected 2θ regions of the XRD patterns measured on a coarse-grained $NaNbO_3$ sample are presented in **Figure 4.33**. Note that only selected temperatures in the vicinity of the *P*→*R* phase transition are presented for the sake of clarity. Upon heating, the first changes in the low 2θ regions of the diffractograms, e.g., 31.8–32.6° and 35.5–41°, were observed at 370 °C; however, a closer look at the peaks at higher 2θ regions revealed the presence of the *R* phase peaks already at 355 °C. In order to investigate the structural changes during the *P*→*R* phase transition, we calculated the unit-cell parameters and the unit-cell volumes at measured temperatures using the Rietveld refinement method and the results are presented in **Figure 4.34** (Rietveld, 1969). Upon heating from RT the unit-cell parameters *a* and *c* increased, while the *b* parameter decreased. As a result the unit-cell volume increased, which could be related to the thermal expansion of the unit cell. At 355 °C a mixed-phase region of coexistence of the *P* and *R* phases was observed, while at 370 °C only the *R* phase was present. This phase transition was also visible in the unit-cell volume curve, where a small anomaly appeared around 355 °C. The low-temperature *P* and the high-temperature *R* phases were both orthorhombic; however, the structure of the latter was much more symmetric, as evidenced by the smaller differences between the unit-cell parameters.

In addition, it should be noted that no anomaly could be observed in the cell parameter or cell-volume curves in the vicinity of 150–190 °C. This supports the absence of a phase transition in this temperature range, as observed by the dielectric spectroscopy described earlier in this section.

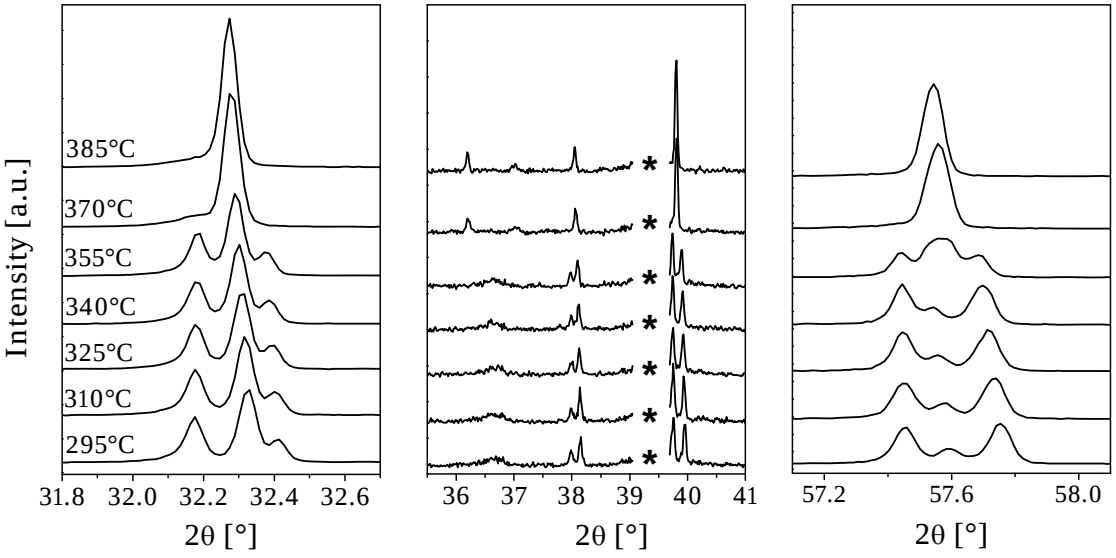

Figure 4.33: Selected 2θ regions of the XRD diffractograms of coarse-grained $NaNbO_3$ ceramics in the temperature region between 295 °C and 385 °C. The asterisk (*) marks the peaks of the substrate, which were cut-out for the sake of clarity.

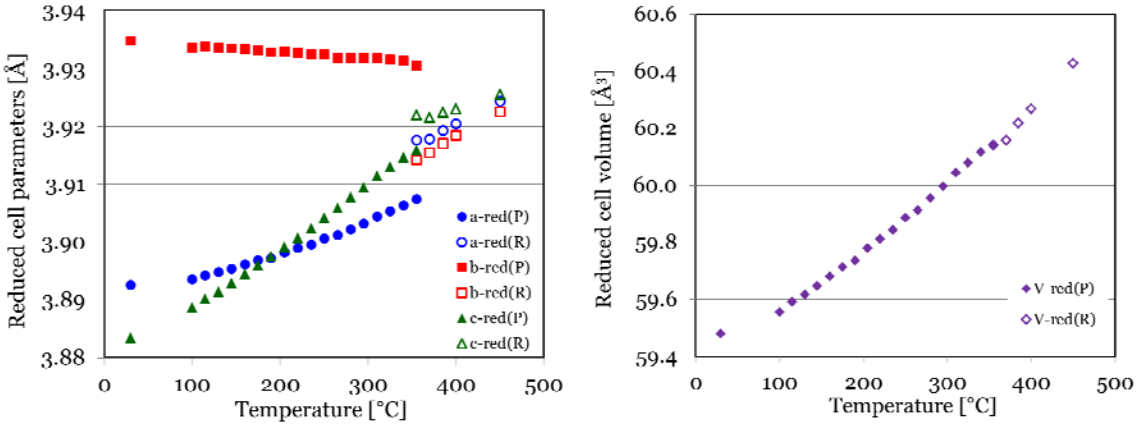

Figure 4.34: Development of the reduced unit-cell parameters and the reduced unit-cell volumes of the coarse-grained $NaNbO_3$ ceramic sample upon heating. The filled symbols represent the low-temperature *P* phase, while the open symbols represent the high-temperature *R* phase.

Using DSC, dielectric measurements and high-temperature XRD we were able to confirm the presence of four phase transitions in the temperature range between RT and 700 °C (**Figure 4.35**), which were in a good agreement with the phase-transition sequence reported by Megaw (Megaw, 1974) for the $NaNbO_3$ single crystals and no additional transitions were observed. The *P*→*R* phase transition was found to occur through a region of coexistence of both phases and resulted in the stabilization of the more symmetric *R* phase above 370 °C. In addition, we investigated the anomaly observed in the vicinity of 150–190 °C and observed frequency dependence of the complex permittivity maxima, which excluded the possibility of another phase transition. The latter was also supported by high-temperature XRD measurements.

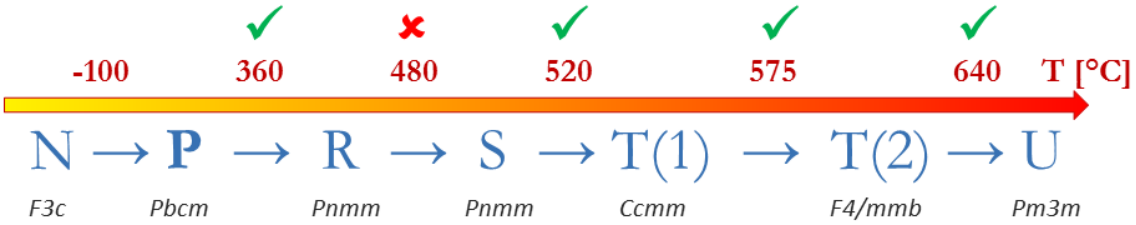

Figure 4.35: The sequence of the temperature-induced phase transitions in $NaNbO_3$, as reported by Megaw (Megaw, 1974). The green tick marks above indicate the phase transitions that we confirmed by DSC and dielectric measurements. Note that the transition below RT was not studied.

4.3.2 Particle/Grain Size-Induced Phase Transitions in $NaNbO_3$

4.3.2.1 Coarse-Grained Ceramics vs. Submicron-Sized Powder

The DSC signals of the coarse-grained ceramics (grain size of approximately 50 μm) and of the submicron-NN powder (particle size of 0.07–0.17 μm) are presented in **Figure 4.36**. We observed differences in the temperature of the main phase-transition peak, which in the case of the ceramics occurred at 371.4 °C (maximum), but was much lower in the case of the powder (onset 303.0 °C, maximum 318.0 °C). The lower intensities of the powder DSC peaks were attributed mainly to different packing. Due to the large

temperature difference, which exceeded 50 °C, the peak of the powder sample could not be related to the $P \rightarrow R$ transition, observed in the ceramic, but was rather close to the temperatures, reported for the $Q \rightarrow R$ transition of the ferroelectric Q phase, detected with other techniques: 300–350 °C (Wada et al., 2003), or 333 °C (Shiratori et al., 2007). This result was an indication of the existence of the Q phase in the submicron-NN powder. Note also that other phase transitions were observed in the powder sample above 500 °C; however, their temperatures were similar to the ones observed in the ceramic sample (discussed in Section 4.3.1).

At this point it should be stressed that the DSC measurements of the $NaNbO_3$ ceramics were performed both on the sintered pellets as well as on the crushed powders, prepared from the same sintered pellets. No differences in the transition temperatures were observed, which indicated that the clamping of the grains within the ceramics did not influence the phase transition.

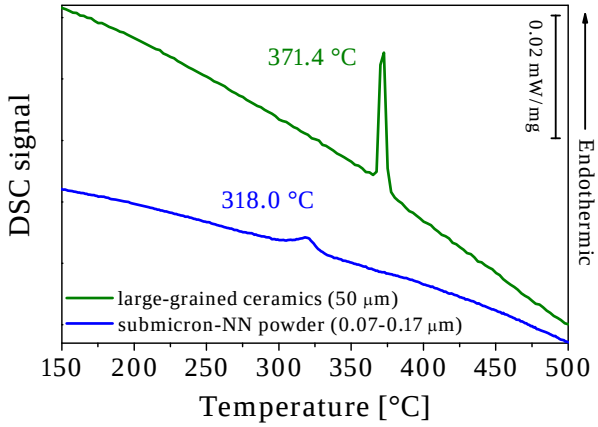

Figure 4.36: The DSC curve of the submicron-NN powder (blue line) compared to the DSC curve of the coarse-grained ceramics (green line) measured upon heating. The numbers above the curves indicate the temperatures of the phase transitions, while the numbers in the legend mark the average grain size and the average particle size of the measured ceramics and powder, respectively.

In order to further elucidate the influence of the particle/grain size on the phase stability in $NaNbO_3$, we compared the XRD diffractograms of the coarse-grained $NaNbO_3$ ceramics and the submicron-NN powder. The full range diffractograms presented in **Figure 4.37a**, revealed pure orthorhombic $NaNbO_3$ in both cases with minimal changes in the intensities of some peaks, which could be related to the different states of the measured sample (ceramic vs. powder). However, upon enlarging the selected 2θ regions (**Figure 4.37b**) some changes could be observed in the diffractograms of the powder: different positions of the peaks in the range between 35.5° and 37.5°, an additional peak in the vicinity of 43 °, and the absence of the peak in the vicinity of 55°. The ICDD-PDF crystallographic cards 01-073-0803 (*Pbcm* SG No. 57) and 01-082-0606 ($P2_1ma$ SG No. 26, setting *cab*), marked by the tick marks in **Figure 4.37b**, were used for comparison in order to identify the polymorphs present in the samples (PDF-ICDD, 2011). The comparison revealed that the coarse-grained $NaNbO_3$ ceramic has the centrosymmetric *Pbcm* space group (antiferroelectric P phase), while the submicron-NN powder has the non-centrosymmetric $P2_1ma$ symmetry (ferroelectric Q phase).

The structure of the Q phase was refined using the Rietveld method (Rietveld, 1969) and is presented in **Figure 4.38**. The unit cell consisted of four basic perovskite units and is basically one half of the antiferroelectric unit cell of the P phase (**Figure 1.16**). The obtained structure is identical to the electric field-induced Q phase observed in $NaNbO_3$

single crystals (Shuvaeva et al., 1993) and to the O_2 phase observed in the $NaNbO_3$ submicron-sized powders obtained by the microemulsion synthesis (Shiratori et al., 2005). The absence of the inversion centre (non-centrosymmetry) is among the most important features of this structure and is one of the conditions for the occurrence of the ferroelectricity.

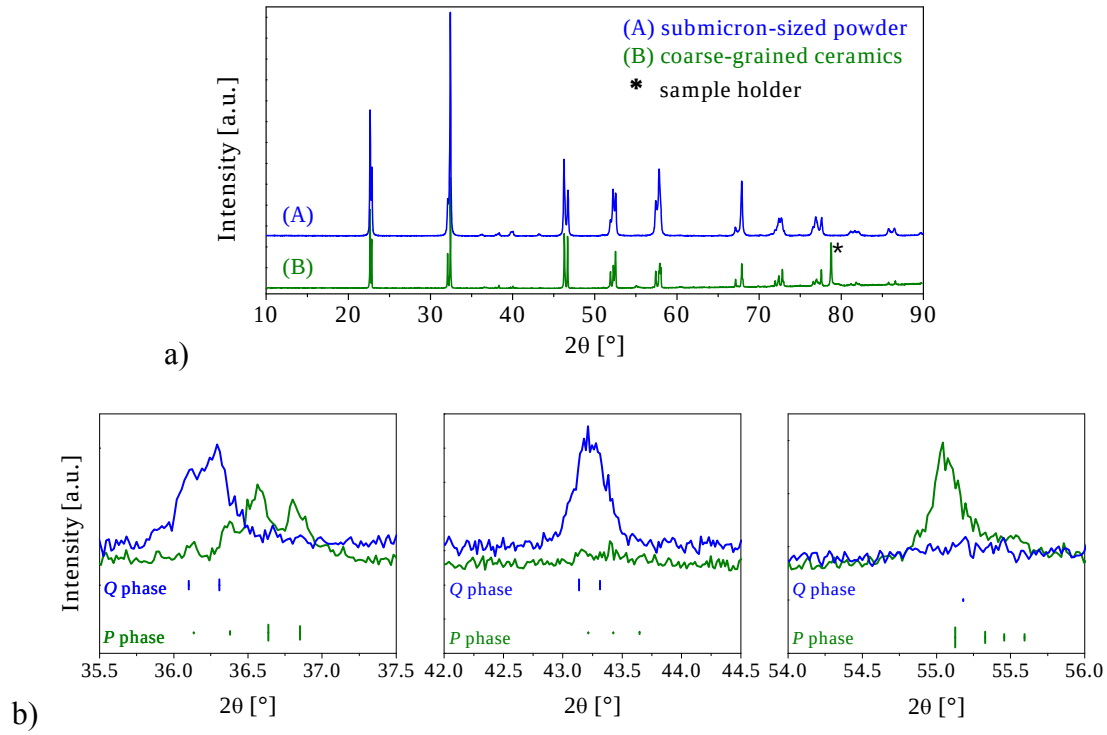

Figure 4.37: XRD patterns of the submicron-NN powder (blue) and the coarse-grained $NaNbO_3$ ceramics (green). Full range diffractograms (a) and enlarged 2θ regions (b), where the set of tick marks represents the reflections associated with the given space groups and their lengths are proportional to the intensities of the peaks (PDF-ICDD, 2011).

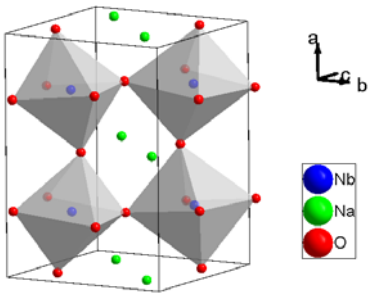

Figure 4.38: The non-centrosymmetric unit cell of the ferroelectric *Q* phase of $NaNbO_3$ at RT, as calculated from the XRD data, measured on the submicron-NN powder.

4.3.2.2 Phase Transitions of the Ferroelectric *Q* Phase

The RT structure of the *Q* phase was investigated and described by Shuvaeva et al. (Shuvaeva et al., 1993); however, little structural data is reported for this polymorph upon heating and the exact transition behaviour is unclear (see Section 1.3.2.3). Therefore, we performed a detailed XRD examination of the crystallographic structure of the submicron-NN powder and its development upon heating. We first measured the

diffractograms of selected regions in the temperature range between RT and 350 °C with a 15 °C step. The temperature development of the (002), (200), (121), (202), and (040) peaks is presented in **Figure 4.39**. The increase of the temperature resulted in a shift of the peaks towards lower 2θ angles, which was related to the increase of the unit-cell volume due to thermal expansion. This was accompanied by a decrease in the number of measured reflections, as the (002) peak disappeared, which was a sign of a higher symmetry of the unit cell.

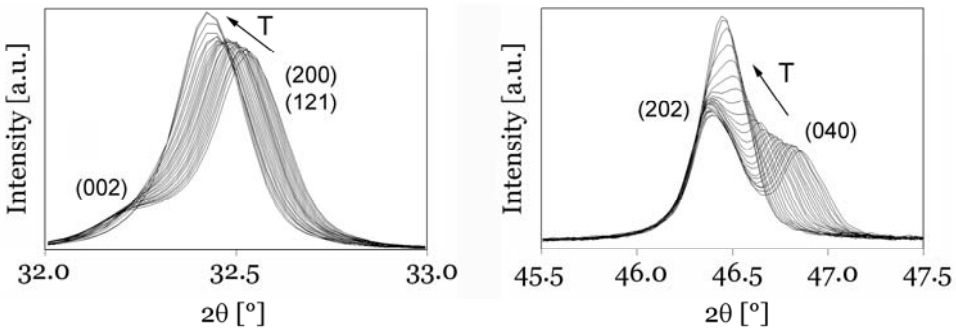

Figure 4.39: Evolution of the (002), (200), (121), (202), and (040) diffraction peaks of the submicron-NN powder upon heating from RT to 350 °C with a 15 °C step.

The unit-cell parameters and volumes were refined for each temperature and the results are shown in **Figure 4.40**. Upon heating, the cell parameters increased with a constant rate up to 265 °C due to the thermal expansion of the material. Above this temperature the values of the cell parameters *b* and *c* started to decrease and consequently the cell volume decreased. Another change was observed at 310 °C, where the values for the cell parameters *a* and *c* increased but the value for *b* decreased rapidly. As a consequence another change in the slope was observed in the cell volume vs. temperature curve at 325 °C. This temperature region is in a good agreement with the temperature of the DSC peak for the submicron-NN powder (**Figure 4.36**); however, the XRD results revealed that the changes in the structure start at lower temperatures. Shiratori et al. reported the phase transition of the submicron-sized $NaNbO_3$ powder at 285–333 °C (Raman) or 300–320 °C (XRD) (Shiratori et al., 2007), which is slightly higher than in our case. This discrepancy may be due to the use of slightly coarser powders, around 280 nm, than in our case. The effect of the particle/grain size on the phase-transition temperature will be further discussed in Section 4.3.2.3.

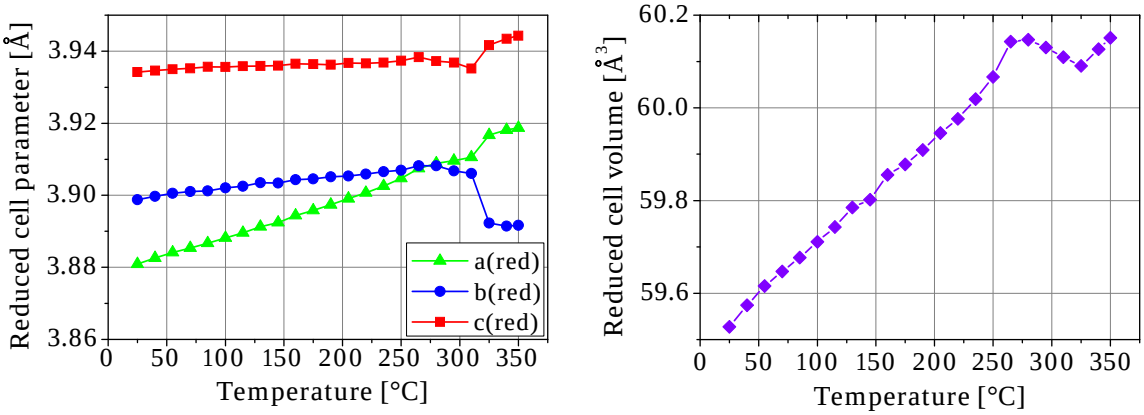

Figure 4.40: Temperature evolution of the reduced unit-cell parameters (left) and the reduced cell volume (right) of the submicron-NN powder in the temperature range between RT and 350 °C.

In addition, Shiratori et al. reported that the above-mentioned phase transition observed in the submicron powder (orthorhombic phase *III* → pseudocubic phase *IV* transition) is different from the phase transition observed in the powders with micron-sized particles (orthorhombic phase P_2 → orthorhombic phase *R* transition) and thus these transitions result in different high-temperature phases.

In order to identify the high-temperature phase and to accurately describe the observed changes in the unit-cell parameters upon heating, we performed full-range XRD measurements of the submicron-NN powder at three different temperatures, chosen according to the changes observed in **Figure 4.40**: RT (reference), 250 °C, and 420 °C. Note that some additional measurements were performed in the region between 265 °C and 325 °C, and the results indicated the presence of a two-phase region; however, this will not be discussed here.

The Rietveld refinement method was used to calculate the structure parameters from the experimental XRD patterns (Rietveld, 1969). We were able to refine the RT and 250 °C structures with the $Pmc2_1$ (No. 26; *Q* phase) and the 420 °C structure with the *Pmmn* (No. 59; *R* phase) space groups. The refined unit-cell parameters and the atomic positions for the three selected temperatures are listed in **Tables 4.1-4.3**.

Table 4.1: Refined structural parameters for the submicron-NN powder at RT. Space group $Pmc2_1$ (No. 26) with a = 7.7633(3) Å, b = 5.5143(2) Å and c = 5.5655(2) Å. Reliability factors: R_{obs} = 3.24 %, R_{wp} = 2.71 %, GOF = 2.58 and $R_{w(all)}$ = 4.34 %.

	x	y	z	U_{iso}	Wyckoff
Nb	0.75	0.754(2)	0.808(3)	0.0056(7)	4c
Na(1)	0	0.250(10)	0.782(12)	0.012(2)[a]	2a
Na(2)	0.5	0.251(11)	0.852(9)	0.012(2)[a]	2b
O(1)	0	0.175(5)	0.263(5)	0.015[b]	2a
O(2)	0.5	0.322(5)	0.285(5)	0.015[b]	2b
O(3)	0.230(3)	0.550(3)	0.058(5)	0.015[b]	4c
O(4)	0.271(3)	0.964(3)	0.513**	0.015[b]	4c

[a] Constrained to the same refined value
[b] Fixed parameters

Table 4.2: Refined structural parameters for the submicron-NN powder at 250 °C. Space group $Pmc2_1$ (No. 26) with a = 7.8066(2) Å, b = 5.5279(2) Å and c = 5.5637(2) Å. Reliability factors: R_{obs} = 2.33 %, R_{wp} = 2.53 %, GOF = 2.38 and $R_{w(all)}$ = 3.13 %.

	x	Y	z	Uiso	Wyckoff
Nb	0.75	0.748(3)	0.814(3)	0.0138(5)	4c
Na(1)	0	0.251(9)	0.817(9)	0.026(2)[a]	2a
Na(2)	0.5	0.234(7)	0.857(5)	0.026(2)[a]	2b
O(1)	0	0.188(7)	0.275(6)	0.015[b]	2a
O(2)	0.5	0.309(7)	0.291(7)	0.015[b]	2b
O(3)	0.232(3)	0.519(4)	0.074(5)	0.015[b]	4c
O(4)	0.266(3)	0.958(4)	0.513**	0.015[b]	4c

[a] Constrained to the same refined value
[b] Fixed parameters

Table 4.3: Refined structural parameters for the submicron-NN powder at 420 °C. Space group *Pmmn* (No. 59) with a = 7.8440(12) Å, b =7.8459(13) Å and c = 7.8567(3) Å. Reliability factors: R_{obs} = 2.54 %, R_{wp} = 2.66 %, GOF = 2.51 and $R_{w(all)}$ = 5.04 %.

	x	y	z	Uiso	Wyckoff
Nb(1)	0.25	0.25	0	0.0185(5)[a]	4c
Nb(2)	0.25	0.25	0.5	0.0185(5)[a]	4d
Na(1)	0	0	0.25(3)	0.047(2)[a]	2a
Na(2)	0	0	0.74(3)	0.047(2)[a]	2a
Na(3)	0	0.5	0.25(3)	0.047(2)[a]	2b
Na(4)	0	0.5	0.75(5)	0.047(2)[a]	2b
O(1)	0.226(8)	0.247(10)	0.252(4)	0.016(2)[a]	8g
O(2)	0.237(6)	0	-0.045(11)	0.016(2)[a]	4f
O(3)	0.299(7)	0	0.499(12)	0.016(2)[a]	4f
O(4)	0	0.271(7)	-0.022(11)	0.016(2)[a]	4e
O(5)	0	0.203(7)	0.509(8)	0.016(2)[a]	4e

[a] Constrained to the same refined value

The calculated unit cells are illustrated in **Figure 4.41**. It should be noted that the phase transitions of the $NaNbO_3$ were reported to be of a displacive nature, with the differences between the phases being the off-centre displacement of the cations and the tilting of the oxygen octahedra (Megaw, 1974).

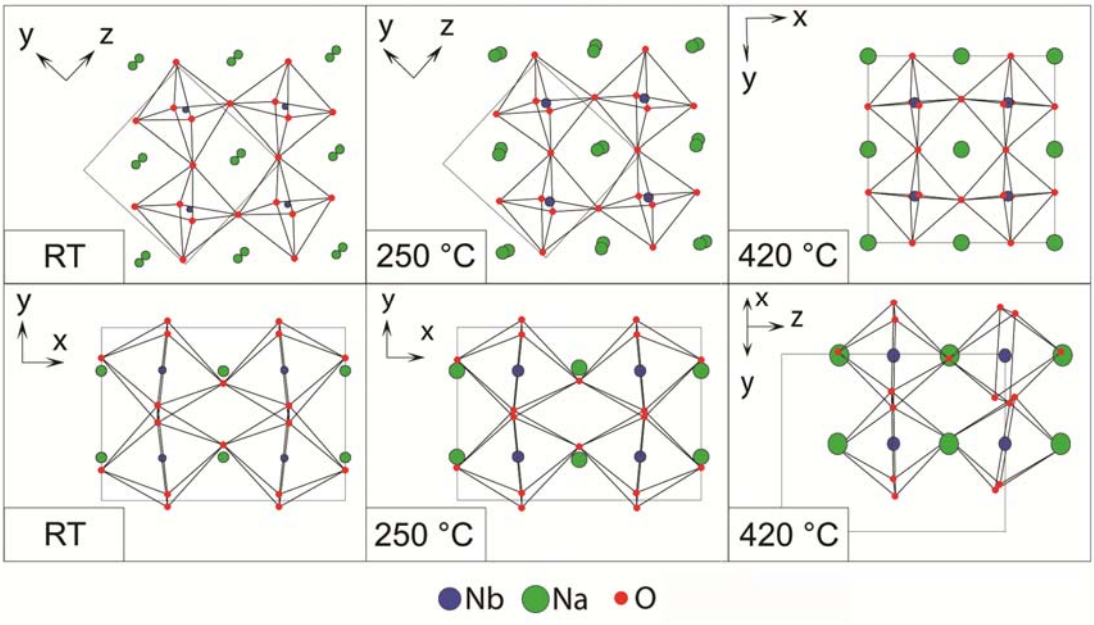

Figure 4.41: Illustrations of the calculated structures of the submicron-NN powder at RT, 250 °C, and 420 °C. Note that the different views at higher temperature are related to the difference in the space groups.

The analysis of the Na^+ cuboctahedral sites was selected to follow the evolution of the octahedral tilting, as well as the displacement of the Na^+ in its site. The distortion of the site from the prototype one, as defined in the cubic structure (U phase, above 640 °C), is related to the tilting of the NbO_6 octahedra. The cuboctahedral cavities observed in the submicron-NN at RT, 250 °C, and 420 °C, are presented in **Figure 4.42a** with the calculated Na–O distances for one of the Na^+ cations (the Na(2); all Na–O distances are available in the Appendix 5.1). The calculated radius of Na^+ in the 12 coordination

number is 1.39 Å and the average value for the Na–O distance is 2.7 Å (Shannon, 1976). Deviations from this value are a signature for the structural changes and therefore tracking the "deviated" distances can give information about the tilting system and the Na^+ displacement. The distribution of the Na–O distances at different temperatures is presented in **Figure 4.42b**, where the distances below 2.4 Å and the ones above 3 Å are considered as "deviated". These borders are marked by the red lines, while the amount of the "deviated" distances is marked by the red numbers. At RT the distortion of the structure was high, as shown by the large spreading of the values of the Na–O distances (11 "deviated" distances). The oxygen octahedra were tilted in three directions and the Na^+ was displaced in the *y*-*z* plane. Upon heating to 250 °C no major change in the Na^+ within its site was observed and only small changes in the amplitude of the octahedral tilting were noticed. Upon further heating, noticeable changes in the structure were observed. At 420 °C the displacement of the Na^+ cation in the *x*-*y* disappeared and only a slight displacement in the *z* direction was detected. The cuboctahedral cavities were more regular (six slightly "deviated" distances), which was the main reason for the observed symmetrisation of the unit-cell parameters.

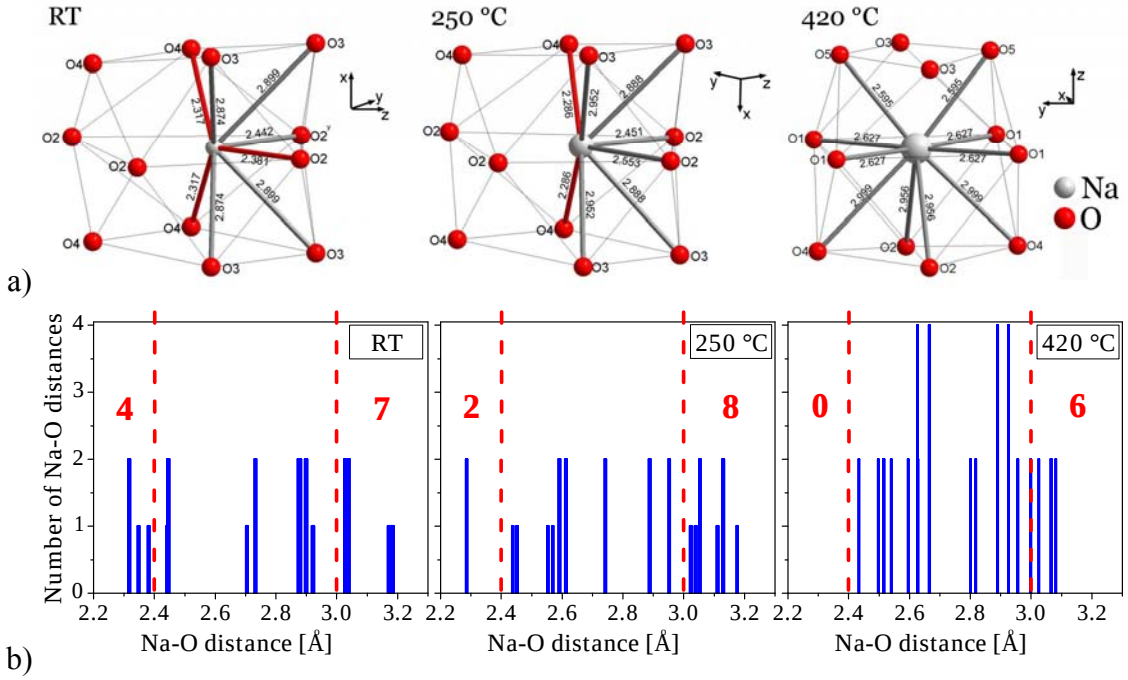

Figure 4.42: a) Cuboctahedral cavities observed in submicron-NN powder for the Na(2) sites at RT, 250 °C, and 420 °C. The Na–O distances between 2.2 Å and 2.4 Å are marked red, between 2.4 Å and 3 Å are grey, while the distances longer than 3 Å are not shown for the sake of clarity. b) Distributions of the Na–O distance values at different temperatures for both Na atoms. The red lines represent the borders of the "normal" Na–O distances between 2.4 Å and 3 Å, while the red numbers give the amount of "deviated" distances at each temperature.

The results presented in Sections 4.3.2.1 and 4.3.2.2 demonstrated the stabilization of the ferroelectric *Q* phase in the submicron-NN powder, while the antiferroelectric *P* phase was stable in the coarse-grained $NaNbO_3$ ceramics. In addition, the phase-transition behaviour of both phases upon heating was investigated. However, from the application point of view, it would be interesting to know if the ferroelectric *Q* phase can also be obtained in the $NaNbO_3$ ceramics by decreasing the average grain size. And if this is the case, at what grain size this transition occurs? These questions are the main topics of the following section.

4.3.2.3 Grain-Size-Induced Transitions between the *P* and the *Q* Phase

To the best of our knowledge the only attempt to investigate the grain-size effect in $NaNbO_3$ ceramics was performed by Pithan et al. in 2006 (Pithan et al., 2006). The $NaNbO_3$ nanopowders obtained by microemulsion-mediated synthesis (Shiratori et al., 2005) were used for the preparation of ceramics by pressure-assisted sintering, which resulted in ceramics with average grain sizes between 0.3 μm and 1.1 μm. At this point it should be noted that the application of commercial pressure-assisted sintering systems typically requires the use of graphite dies and rams, which results in the reduction of the oxide ceramics. Since the authors did not report the usage of special non-graphite dies and they did not present the possible influence of carbon, the composition and defect state of the samples may be questionable. The sintered samples were claimed to consist of a mixture of the antiferroelectric *P* and the ferroelectric *Q* phase, as concluded from the comparison of the grain-size distributions with the size-stability regions for both phases, obtained from the previous analysis of the powders (Shiratori et al., 2005). However, the used analytical methods (XRD, Raman) failed to present a clear distinction between the phases and the critical grain size for the $P \rightarrow Q$ transition remained undefined. A detailed analysis using different characterisation methods is therefore required in order to determine the critical grain size for the size-induced phase transition between the antiferroelectric and ferroelectric phases in $NaNbO_3$.

In order to investigate the effect of the grain size on the phase-transition behaviour of $NaNbO_3$, and consequently on its physical properties, we prepared a series of $NaNbO_3$ ceramic samples with a wide grain-size range from about 0.15 μm to 50 μm using conventional and pressure assisted sintering. Their microstructures are presented in **Figure 4.43**. These samples will be marked as "NNX", where the "X" represents the average grain size in μm. The average grain sizes were measured as described in Section 3.2.2. The NN0.15e sample is an exception as we were not able to perform the same analysis due to the extremely small grain sizes and therefore the size was only estimated from the fracture surfaces (this is marked by the letter "e"). The relative densities of the samples with average grain sizes above 0.6 μm were between 92 % and 99 %; the samples with grain sizes below 0.6 μm had relative densities between 75 % and 88 %; while the relative density of the NN0.15e sample was below 70 %. We found that the relative density did not influence the phase stability or the temperature of the phase transitions and will therefore not be discussed here; however, a more detailed explanation will be given at the end of this section.

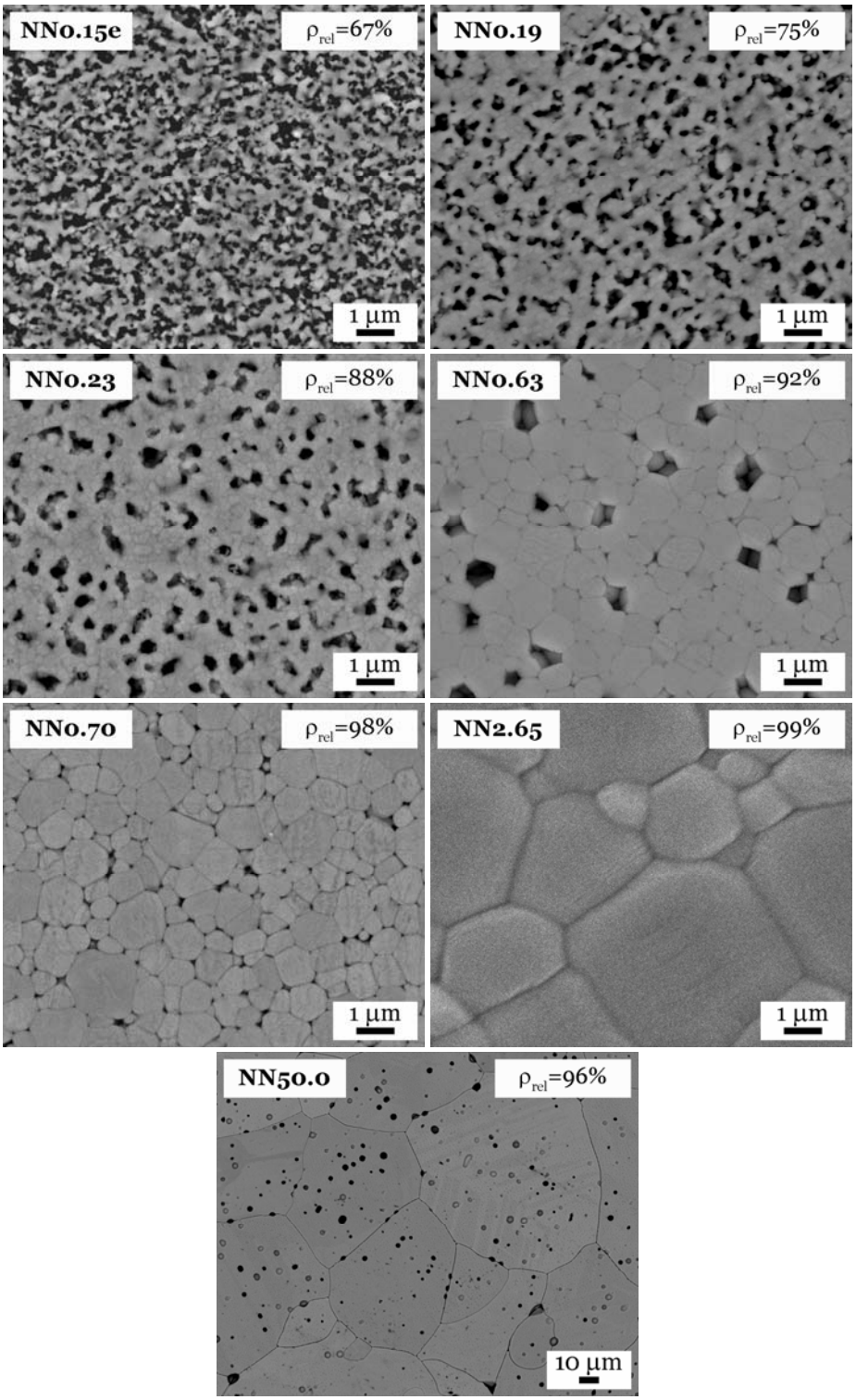

Figure 4.43: SEM images of the polished and thermally etched $NaNbO_3$ ceramics used for the investigations of the grain-size-induced phase transitions. Note the change of scale for the NN50.0 sample.

Three selected samples with different grain sizes (NN2.65, NN0.19, and NN0.15e) were investigated using XRD and the enlarged 2θ regions of the diffractograms are presented in **Figure 4.44**. The phase analysis revealed the presence of the *P* phase in the NN2.65 sample and the *Q* phase in the NN0.15e sample. The phase composition of the NN0.19 sample could not be unambiguously identified due to the limited resolution of the laboratory X-ray diffractometer; however, traces of both phases were observed, which

indicated the presence of a phase mixture. These results are consistent with the phase analysis of the submicron-NN powder and the coarse-grained ceramics in Section 4.3.2.1 (**Figure 4.37**).

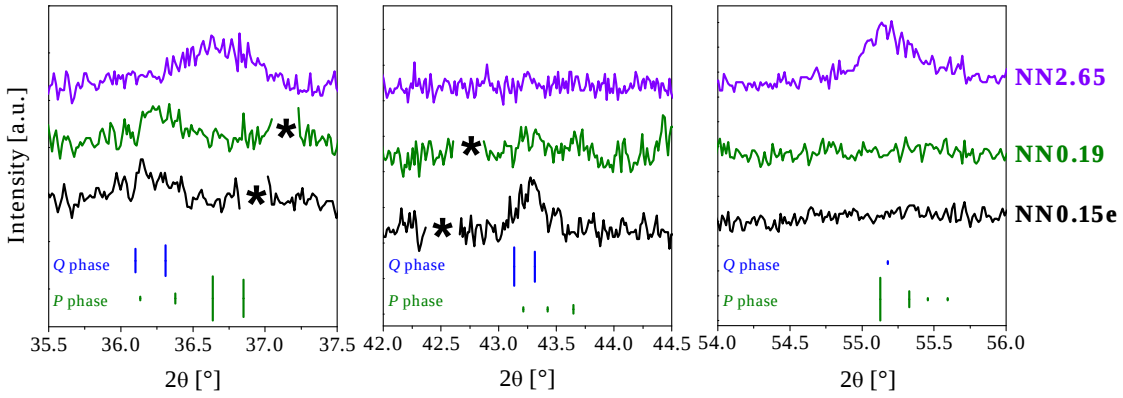

Figure 4.44: Selected 2θ regions of XRD diffractograms of three $NaNbO_3$ samples with different grain sizes (2.65 µm, 0.19 µm and 0.15 µm). The tick marks below the diffractograms represent the reflections associated with the given space groups and their lengths are proportional to the intensities of the peaks (PDF-ICDD, 2011). The asterisk (*) marks the peaks of the substrate, which were cut-out for the sake of clarity.

The similarity between the structures of the *P* and the *Q* phases and the limited resolution of the laboratory X-ray diffractometer hindered a clear distinction between both phases in the mixed-phase region. However, as presented in Section 4.3.2.1, these two phases could be distinguished by their different transition temperatures upon heating: the transformation of the *P* phase occurs at 360–370 °C (*P*→*R*), while the transformation temperature of the *Q* phase is lower, at 300–320 °C (*Q*→*R*). The series of $NaNbO_3$ ceramic samples with different grain sizes was analysed by the DSC method and the results are presented in **Figure 4.45**. Note that the different slopes of the DSC curves are related to the different baselines of the individual measurements; however, they do not influence the positions of the DSC peaks. The following trends were observed:

The DSC peak of the coarse-grained ceramic samples (NN50.0 and NN2.65) occurred at 373 °C and was related to the *P*→*R* phase transition, confirming the presence of the *P* phase, consistent with the XRD results (Section 4.3.1). The decrease of the average grain size of the samples to 0.63 µm resulted in a decrease of the *P*→*R* phase-transition temperature by about 35 °C.

The decrease of the average grain size to 0.23 µm resulted in the appearance of two clearly separated DSC peaks (enlarged in **Figure 4.45b**): the peak at 344 °C could be related to the *P*→*R* transition observed in the coarse-grained ceramics, while the lower peak at 293 °C was closer to the *Q*→*R* transition, observed in the submicron-NN powders (Section 4.3.2.2), and therefore indicated the presence of the *Q* phase.

The further decrease of the average grain size below 0.23 µm reduced the amount of the *P* phase, as evidenced by the decrease of the *P*→*R* peak and the increase of the *Q*→*R* peak. At an average grain size of about 0.15 µm only the *Q* phase was detected, as previously confirmed by XRD (**Figure 4.44**).

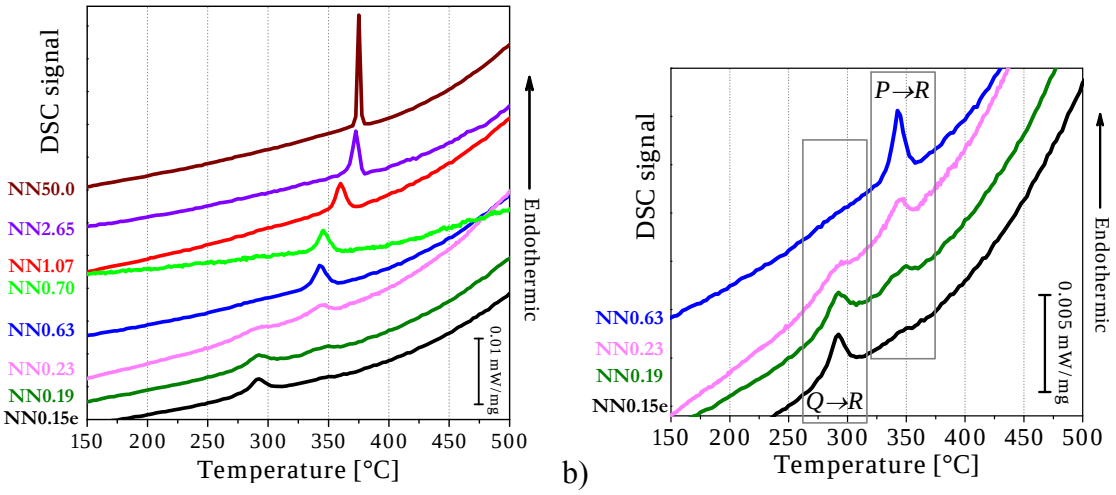

Figure 4.45: DSC curves of the $NaNbO_3$ ceramic samples with different grain sizes, as measured upon heating (a) and the enlarged region of the DSC curves of the selected samples with grain sizes close to the expected $P \rightarrow R$ size-induced phase transition (b). The numbers by the side of the graphs represent the average grain size of the measured samples.

In addition, we measured the temperature dependence of the dielectric permittivity of the samples with different grain sizes. The results for four representative samples obtained upon heating are presented in **Figure 4.46**. Note that the measurement of the dielectric permittivity of the NN0.15e sample was not possible due to the low density. The maximum in the NN2.65 sample occurred at around 375 °C and decreased with decreasing the average grain size down to 0.63 μm. The 0.19-μm sample again showed a double peak with maxima around 304 °C and 346 °C. These results are consistent with the DSC measurements and confirmed the occurrence of the $P \rightarrow R$ transition in the samples with grain sizes between 2.65 μm and 0.63 μm, while both $P \rightarrow R$ and $Q \rightarrow R$ transitions occurred in the NN0.19 sample.

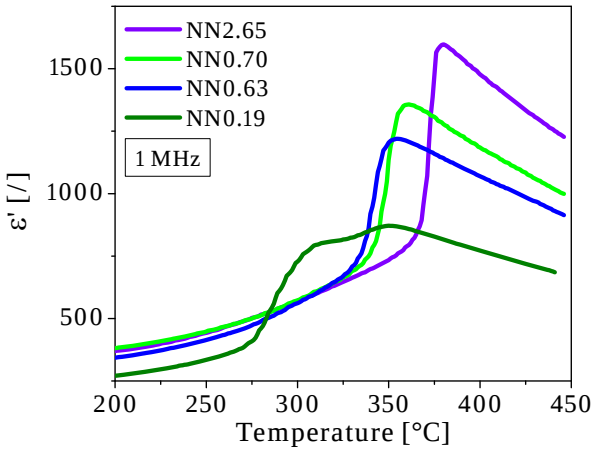

Figure 4.46: Temperature dependence of the real part of the permittivity of $NaNbO_3$ ceramic samples with different grain sizes, as measured upon heating.

The phase-transition temperatures obtained from the DSC and dielectric measurements are collected in **Figure 4.47**. The slightly higher transition temperatures obtained using the dielectric measurements could be related to the experimental differences between both measurement techniques, although the same heating rates were applied.

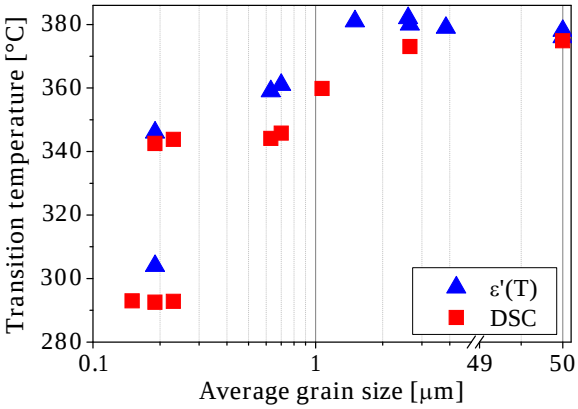

Figure 4.47: Grain size dependence of the phase-transition temperatures of $NaNbO_3$ ceramics as determined by DSC (peak maximum) and dielectric measurements upon heating.

The presented results revealed a strong influence of the grain size of the $NaNbO_3$ ceramics on the phase stability and the temperature of the phase transitions, which may explain the discrepancies in the literature reports, described in Section 1.3.2.

In the above analysis each sample was described by its average grain size; however, if we want to accurately determine the critical grain size for the size-induced $P \rightarrow Q$ transition the entire grain size distribution needs to be considered. The comparison of the grain size distributions of the samples in the investigated transition region (below 0.7 μm) is presented in **Figure 4.48**. The majority of the grains in the NN0.70 and NN0.63 samples, which exhibited only one peak in the DSC curves ($P \rightarrow R$) (**Figure 4.45b**), were in the range between 0.2 μm and 1.2 μm. In both samples that exhibited double peaks in the DSC curves (NN0.23 and NN0.19), the majority of the grains were in the range between 0.1 μm and 0.4 μm; however, from the enlarged distribution histograms and cumulative curves in **Figure 4.48b,c** we could observe an important difference: the amount of grains below 0.2 μm was larger in the NN0.19 sample (about 70 %) than in the NN0.23 sample (about 40 %), which resulted in the larger $Q \rightarrow R$ DSC peak than the $P \rightarrow R$ peak in this sample (**Figure 4.45b**). The opposite situation occurred in the NN0.23 sample, where the amount of the grains with sizes below 0.2 μm was lower and thus also the $Q \rightarrow R$ DSC peak was smaller. Since these observations were only found for a grain size of about 0.2 μm we can conclude that this is the critical grain size for the inducement of the $P \rightarrow Q$ phase transition – larger grains will exhibit the antiferroelectric P phase, while the smaller grains, the ferroelectric Q phase.

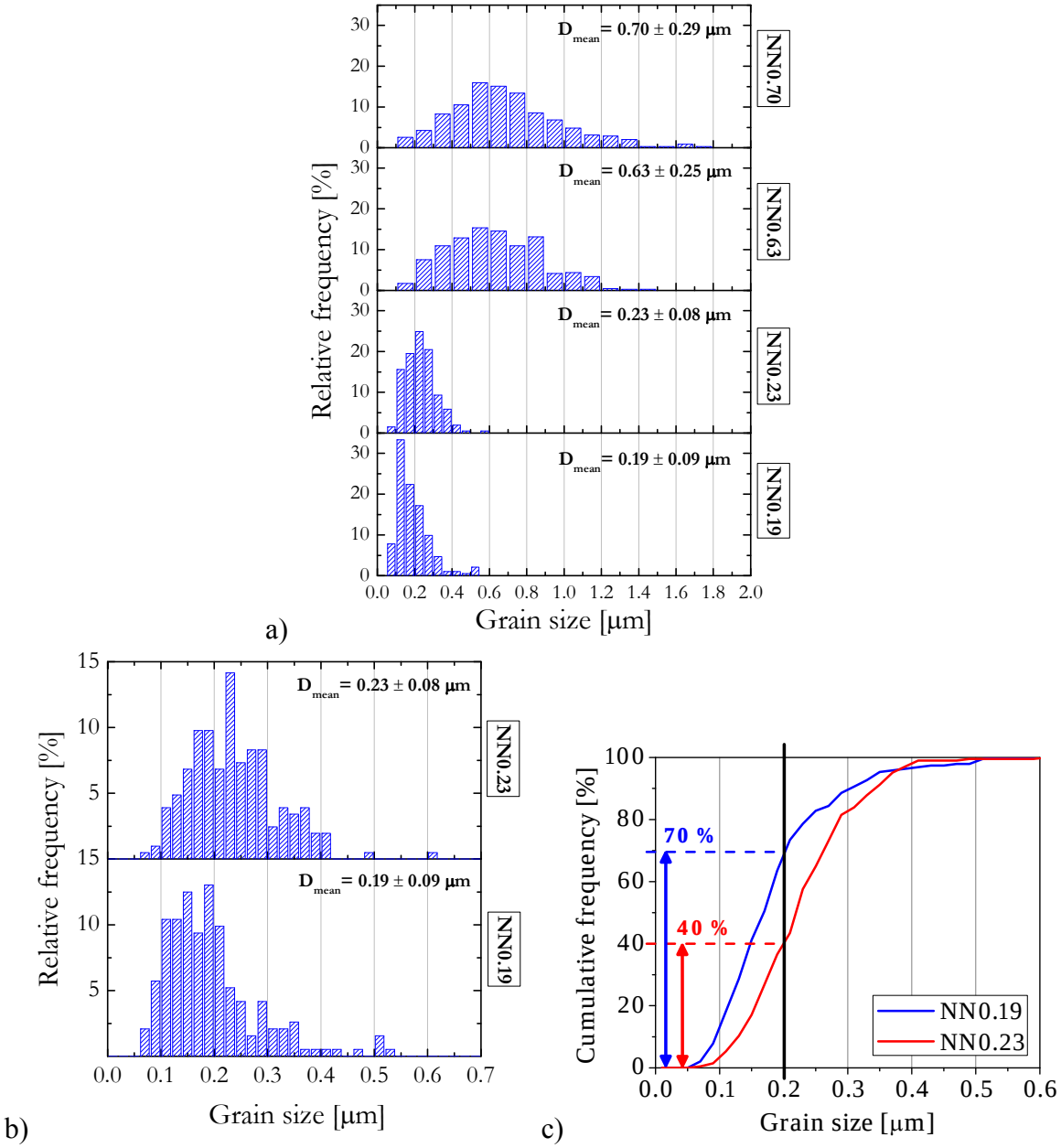

Figure 4.48: Grain size distributions and average grain sizes of the $NaNbO_3$ ceramic samples with average grain sizes below 0.70 µm (a) and enlarged histograms (b) and cumulative curves (c) of the NN0.23 and NN0.19 samples. The arrows in (c) mark the percentage of the grains smaller than 0.2 µm in each sample.

The critical grain size of the ceramics determined in the present work is lower than in previous results obtained from the $NaNbO_3$ powders, where the antiferroelectric O_1→ferroelectric O_2 phase transition was observed at a particle size of 0.6 µm (Shiratori et al., 2005). It should be noted that the authors reported only estimated particle size values obtained from SEM images and BET measurements and no particle size distributions were presented. The discrepancy between the values observed in the ceramic and powder samples may originate from the different synthesis methods used in both studies, microemulsion-mediated synthesis with subsequent annealing versus solid-state synthesis and pressure-assisted sintering.

As discussed earlier in this section, the relative density of the samples did not seem to influence the observed phase-transition temperatures for the investigated relative density range between 67 % and 99 %. To verify this we prepared two samples with similar

average grain sizes (about 0.19 µm) and different relative densities (75 % and 88 %) using pressure assisted sintering. The DSC signals of both samples measured under the same experimental conditions are presented in **Figure 4.49**. Note that the different slopes of the DSC curves are due to the different baselines of the individual measurements; however, this does not influence the positions of the DSC peaks. The differences between the temperatures of the *P*→*R* and the *Q*→*R* phase transitions in both samples were less than 2 °C. In addition, as noted before, there was no temperature difference in the DSC peaks when measuring uncrushed or crushed ceramic pellets (see Section 4.3.2.1). Thus we could conclude that the relative density of the samples or the possible clamping between the grains, for the densities considered here, does not influence the temperatures of the grain-sized-induced phase transitions in $NaNbO_3$.

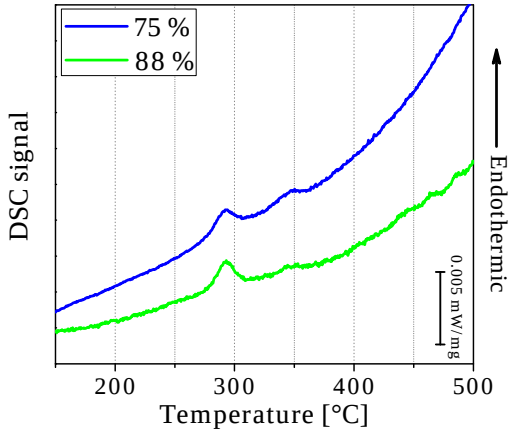

Figure 4.49: DSC signals of two ceramic $NaNbO_3$ samples with similar grain sizes (0.19 µm) and different relative densities: 75 % and 88 %, as measured upon heating.

In summary, the size-induced phases transition in the $NaNbO_3$ ceramics were investigated using XRD, DSC and dielectric measurements. While the antiferroelectric *P* phase was found to be stable in coarse-grained ceramics, the ferroelectric *Q* phase was stabilized in the fine-grained samples. The critical grain size for the *P*→*Q* transition was found to be about 0.2 µm and the samples with grain sizes around this critical value consisted of both phases due to the breadth of the grain size distributions. These results revealed the influence of the grain size on the phase stability and the physical properties of the $NaNbO_3$ ceramics and may facilitate the search for potential applications.

4.3.3 Electric-Field-Induced Phase Transitions in $NaNbO_3$ Ceramics

According to literature reports, described in Section 1.3.2.3, a phase transition in antiferroelectric $NaNbO_3$ could also be induced by applying a sufficient external electric field, resulting in the stabilization of the ferroelectric *Q* phase. However, the exact amplitude of the electric field for this transition at a given temperature and frequency is not known.

In order to determine the effect of the external electric field on the phase composition, we investigated the behaviour of the coarse-grained antiferroelectric $NaNbO_3$ ceramics under an applied electric field at different temperatures. The polarization versus electric field dependence of the samples was measured in the temperature range between RT and 100 °C, while the applied field was 8 kV/mm and the frequency was 0.1 Hz. A detailed description of these measurements is given in Section 3.3.4 and the results are presented in **Figure 4.50**. Between RT and 80 °C the material response to an applied electric field

was linear; however, upon increasing the temperature a ferroelectric hysteresis loop starts to open up around 85 °C. At 100 °C the coercive field was about 4.4 kV/mm (calculated as $(E_C^+ + E_C^-)/2$), while the remanent polarization reached a value of about 32 μC/cm^2. We also measured the electric-field-induced longitudinal strain response using a linear variable differential transformer. No strain could be detected between RT and 80 °C (**Figure 4.51a**); however, once the ferroelectric state was induced around 85 °C a butterfly-like hysteresis loop was observed, as presented in **Figure 4.51b**, which suggests the switching of the ferroelectric and ferroelastic domains. In addition, a piezoelectric d_{33} coefficient of 28 pC/N was measured. These results confirm the inducement of the ferroelectric phase after the application of a sufficiently large electric field and a high-enough temperature.

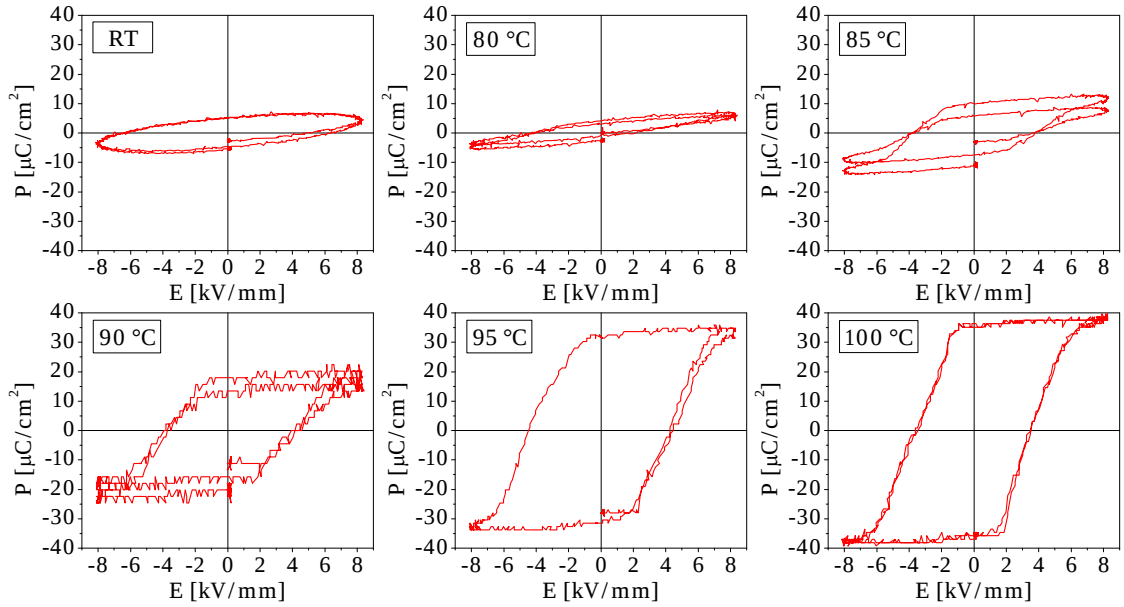

Figure 4.50: Polarization versus electric field loops of $NaNbO_3$ ceramics, measured at different temperatures (E_{max}=8 kV/mm, f=0.1 Hz).

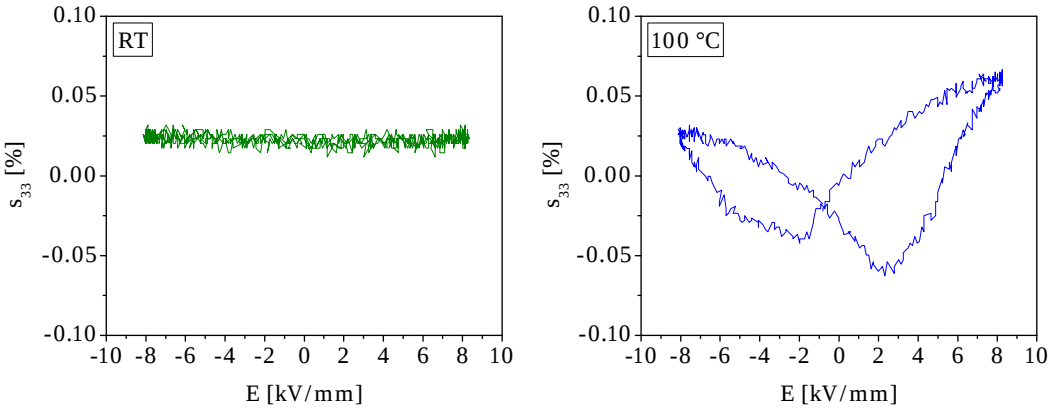

Figure 4.51: Longitudinal strain (s_{33}) versus electric field response of $NaNbO_3$ ceramics at RT and at 100 °C.

In order to identify the structure of the induced ferroelectric phase, we performed an XRD analysis. The enlarged 2θ regions of the XRD patterns of the $NaNbO_3$ coarse-grained ceramic sample, before and after the application of the electric field, are

compared in **Figure 4.52**. The comparison of the diffractograms with the crystallographic data confirmed the presence of the antiferroelectric *P* phase (*Pbcm* space group) in the sample before the application of an electric field, while a phase transformation towards the *Q* phase ($P2_1ma$ symmetry) occurred after the application of the electric field. This situation is identical to the size-induced $P \rightarrow Q$ phase transition, which was observed when comparing the coarse-grained ceramic sample and the submicron-sized powder (**Figure 4.37**).

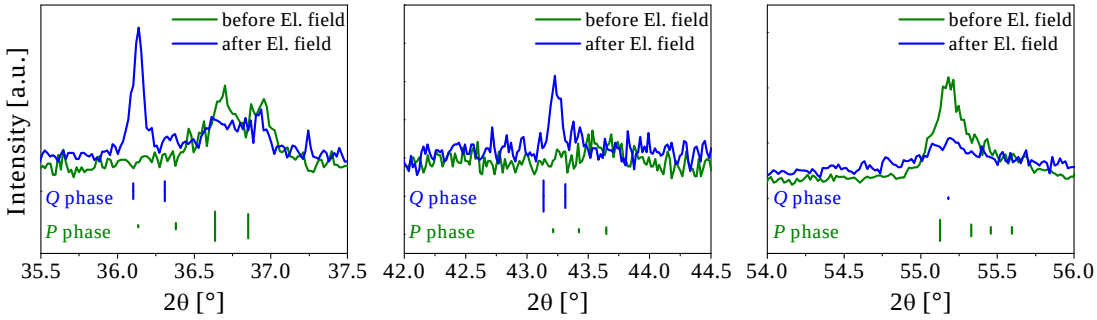

Figure 4.52: Enlarged 2θ regions of the XRD patterns of a $NaNbO_3$ ceramic sample before (green line) and after (blue line) the application of an electric field. The set of tick marks represents the reflections associated with the given space groups and their lengths are proportional to the intensities of the peaks (PDF-ICDD, 2011).

In addition, it should be noted that the ferroelectric phase, once induced, remained stable upon decreasing the temperature to RT, which indicates the irreversible nature of the electric-field-induced $P \rightarrow Q$ phase transition, in agreement with previous observations (Cross and Nicholson, 1955). This is in contrast to the double-hysteresis loops measured in $PbZrO_3$, which suggests a reversible antiferroelectric-ferroelectric phase transition (Sawaguchi and Kittaka, 1952).

Besides the dependence on the temperature, as observed earlier in this section, the inducement of the ferroelectric phase was found to be also influenced by the magnitude of the electric field. The electric field required to induce the ferroelectric phase (when the P(E) response becomes non-linear), will be denoted as the "FE-threshold" field. In order to estimate the temperature dependence of the FE-threshold fields, we performed polarization versus electric field measurements at RT, 150 °C, and 200 °C. During these measurements the temperature was held constant, while the amplitude of the electric field was gradually increased from 1 kV/mm until electrical breakdown occurred. Both characteristic electric field values, the FE-threshold and the electrical breakdown fields, obtained from these measurements, are presented in **Figure 4.53**, where the results of the constant electric field measurements from **Figure 4.50** are also added for comparison. At RT the ferroelectric state could not be induced, which indicates that the FE-threshold field is probably higher than the electrical breakdown field (9.5 kV/mm). However, upon increasing the temperature the ferroelectric hysteresis loop could be induced before the occurrence of the electrical breakdown. The values of both characteristic fields decreased with increasing the temperature. At 200 °C the ferroelectric loop was induced at 6.5 kV/mm, while electrical breakdown occurred at around 7.5 kV/mm.

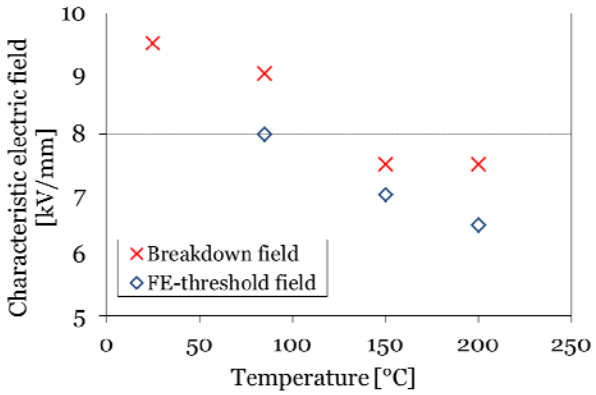

Figure 4.53: Temperature dependence of the characteristic electric field values (FE-threshold field and electrical breakdown field) for $NaNbO_3$ ceramics.

These results were compared with the work of Dungan and Golding, who were up to now the only ones to systematically study the inducement of the ferroelectric phase in $NaNbO_3$ ceramics (Dungan and Golding, 1964). The authors reported the inducement of the ferroelectric loop around 100 °C, which is slightly higher than in our case (85 °C), while the obtained ferroelectric phase had similar characteristics and was stable up to about 270 °C. In addition, the authors noted that the electrical and thermal energies required for the inducement of the ferroelectric phase seem to be sensitive to variations in the raw materials and ceramic processing techniques, which would explain the discrepancy found in the literature. The values of the breakdown fields observed in our ceramic samples were comparable to the values reported for the $NaNbO_3$ single crystals, which were between 8 and 10 kV/mm (Cross and Nicholson, 1955).

4.3.4 Summary

Section 4.3 reports and discusses the results from the investigation of the phase-transition behaviour of $NaNbO_3$. First we re-examined the temperature-induced phase transitions of the coarse-grained $NaNbO_3$ ceramics using DSC, dielectric spectroscopy and high-temperature XRD (Section 4.3.1). The RT structure was confirmed to be the antiferroelectric *P* phase, which upon heating underwent the phase-transition sequence consistent with the reports of Megaw (Megaw, 1974). In order to investigate the dielectric anomaly observed in the vicinity of 150 °C, we performed a dielectric spectroscopy analysis and observed frequency dependence of the ε''(T) maxima, which excluded the possibility of another phase transition, as also supported by the XRD measurements.

In the second part (Section 4.3.2) we focused on the phase transitions induced by the change in the particle or grain size. We compared the DSC signals of the coarse-grained ceramic and submicron-sized powder and observed large differences in the temperature of the main transition peak. XRD analysis revealed that the submicron-sized powder at RT consisted of the ferroelectric *Q* phase. Since little structural data could be found in the literature for the *Q* phase upon heating and the exact transition behaviour was unclear, we performed a detailed XRD examination of this phase upon heating. The $Q \rightarrow R$ transition occurred between 265 °C and 325 °C, possibly through a region of the coexistence of both phases. At RT the distortion of the structure was high: the oxygen octahedra were tilted in three directions and the Na cation was displaced in the *y*-*z* plane. Upon heating the symmetry of the structure increased; after the transition the Na cation was placed in the centre of the *x*-*y* plane and only a slight displacement in the *z* direction was observed. The cuboctahedral cavities were more regular, which was the main reason for the

observed symmetrisation of the unit cell.

In order to investigate the size-induced phase transition in $NaNbO_3$ ceramics, we prepared a series of ceramic samples with average grain sizes from about 0.15 μm to 50 μm and examined them using XRD, DSC and dielectric measurements. The critical grain size for the $P \rightarrow Q$ transition was found to be around 0.2 μm and the samples with grain sizes around this critical value consisted of both phases due to the breadth of the grain size distributions.

Finally, we investigated the phase transition induced by the application of an external electric field with the aim to determine the conditions for this transition (Section 4.3.3). The values of the threshold field for the inducement of the ferroelectric phase and the breakdown field were determined for a temperature range between RT and 200 °C. The ferroelectric nature of the induced phase was confirmed by measurements of the polarization, strain and XRD. While at RT no ferroelectric phase could be induced at fields smaller than the breakdown field, at 200 °C the ferroelectric phase could be induced using an electric field of about 6.5 kV/mm.

5 Summary, Conclusions and Outlook

The present work reports and discusses the results obtained from investigations of the perovskite ceramic material sodium niobate ($NaNbO_3$) - a model system for the study of complex alkaline niobate-based systems and a prototype antiferroelectric. We studied two processing steps of this material, the preparation of the $NaNbO_3$ powders and the sintering, and finally investigated the phase-transition behaviour of the obtained samples. The following summary is divided into three parts; each is focused on one of the major topics. The main conclusions are given and the future prospects are discussed.

5.1 $NaNbO_3$ Nanopowders

In the first part, we presented an alternative processing route for $NaNbO_3$ nanopowders, based on the top-down approach. The submicron $NaNbO_3$ powder (submicron-NN), with a primary particle size of 0.07–0.17 μm and an aggregate size of 0.4–0.7 μm, was prepared using solid-state synthesis and was further milled to the nano-range using agitator bead milling. The optimized milling parameters, the rotation speed of 2000 min^{-1} and the milling time of 75 min, resulted in the production of the $NaNbO_3$ nanopowder (nano-NN) with particle sizes of 25–30 nm and a narrow particle size distribution, as determined by the field-emission scanning electron microscopy (FE-SEM), BET and X-ray diffraction analysis (XRD). This result was comparable to the results obtained by other processing techniques based on the bottom-up approach, such as the Pechini route, microemulsion-mediated synthesis or mechanochemical synthesis. In addition, microstrains of approximately 2 % were found in the prepared nanopowders, which could indicate the presence of defects, created during the milling process.

The compaction behaviour of the obtained nano-NN was investigated and compared to the submicron-NN, prepared via solid-state synthesis. The nanopowder exhibited better compactability at isostatic pressures above 550 MPa, which resulted in higher relative green densities. From the results of the N_2 desorption measurements we observed uniform pore-size distributions in all the powder compacts. The average pore-radius values were 4–10 nm and 20–30 nm for the nano-NN and the submicron-NN powder compacts, respectively; however, the pore-size distributions were much broader for the coarser powder. These results indicated a uniform packing of the particles and the absence of agglomerates and therefore represented a suitable starting point for the sintering process.

The proposed top-down processing route for the preparation of nanopowders may represent an interesting alternative to other processing techniques that are currently widely used in the field of electronic ceramics, such as the solution-based chemical routes or mechanochemical synthesis. The main advantages are the use of widely-available inexpensive reactants, cost efficiency and the possibility to upscale, while the disadvantages are the inducement of the microstrains and the possible contamination of the product during the milling process, which may occur if the processing conditions are not optimized and well controlled. We demonstrated the application of this processing route on the example of $NaNbO_3$; however, with further modifications this method can also be adapted to produce nanopowders from other alkaline-niobate systems, such as, e.g., $(K,Na)NbO_3$.

5.2 Sintering of $NaNbO_3$

The sintering of alkaline-niobate ceramics has been reported to be one of the most problematic processing steps, mainly due to low densification and an inability to control the microstructure. Despite the extensive research of these materials, not much is known about the basic mechanisms that take place on the microscopic level during sintering, such as material-transport mechanisms, grain-boundary and pore migration or grain-growth mechanisms.

We studied the sintering behaviour of submicron-NN and nano-NN powder compacts using optical dilatometry and FE-SEM microstructure analysis. All the samples exhibited similar dynamic sintering curves with a very narrow shrinkage interval just before reaching the melting point at 1400–1410 °C, as previously observed in other alkaline-niobate systems. The submicron-NN sample started to densify at approximately 1280 °C, while the onset of densification of the nano-NN sample was about 100 °C lower; however, at 1280 °C both samples reached the same relative density and above this temperature their densification curves almost coincided, which indicated that the initial differences in particle sizes between both samples disappeared before the samples reached the main densification stage. This was confirmed by comparing the microstructure development during heating, whereby, due to considerable coarsening during the initial sintering stage, both samples exhibited similar microstructures before the start of the main densification stage at 1320 °C: a relative density of 62–64 % and a grain size of 0.8–1.0 μm.

The microstructure-development trajectories were used to follow the competing effects of grain growth and densification. The use of different starting $NaNbO_3$ powders (submicron- and nano-sized) or the application of different heating rates (10–200 K/min) did not influence the course of the microstructure-development trajectories, which indicated the dominance of the grain-growth processes during the initial sintering stage, well before the onset of densification. This behaviour was different than observed for some other ceramic systems, such as, e.g., Al_2O_3, $BaTiO_3$ or ZrO_2, where rapid densification and negligible grain growth were observed during the intermediate sintering stage and considerable grain growth occurred only after the critical density was reached. By analysing the specific surface area reduction during the isothermal sintering of the nano-NN powder compacts we identified the surface diffusion to be the dominant material-transport mechanism during the initial sintering stage and the corresponding activation energy was estimated to be very low, between 50–60 kJ/mol. The important consequence of the activation of non-densifying material-transport mechanisms was the reduction of the sintering driving force and, thus, hindrance of the densifying mechanisms, which could explain the observed difficulties in obtaining high densities and fine-grained microstructures in these materials. The low activation energy for surface diffusion may originate from the intrinsic physical properties of $NaNbO_3$, since the reported calculated lattice energy is much lower than for most other perovskite systems, or from the extrinsic contributions, such as the small particle size. Further investigations are needed in order to determine the exact origin.

In addition, we investigated the sintering behaviour of the nano-NN powder compacts during the intermediate sintering stage using optical dilatometry, microstructure analysis and the analytical model proposed by Coble. The results indicated the dominance of the grain-boundary diffusion, which could be related to the use of very fine starting powders. In addition, the results obtained from the Knudsen effusion mass spectrometry indicated a Na vapour pressure over $NaNbO_3$ of $1.6 \cdot 10^{-5}$ bar at 1350 °C, which suggested that the material transport via the vapour phase becomes increasingly important during the later stages of sintering, provided that free surfaces are still available.

Based on the results presented above, we decided to use the pressure-assisted sintering technique in order to prepare dense $NaNbO_3$ ceramics with submicron-sized grains. The nano-NN powder compacts were sintered at different temperatures, 1100 °C and 1150 °C, for different periods of time, 3 h and 6 h, while an external pressure of 24.5 MPa was applied. The application of the external pressure resulted in a considerable shift of the microstructure-development trajectories towards smaller grain sizes and higher densities, which was connected to the successful impediment of the surface diffusion due to the early reduction of the total free surface area, additional rearrangement of the particles during the heating stage and the increased grain-boundary area, which provided material transport paths for grain-boundary diffusion and thus enhanced densification. The highest relative density (98 %) and the smallest average grain size (0.70±0.29 μm) were obtained after sintering for 6 h at 1150 °C.

Finally, we investigated the phenomenon of abnormal grain growth during the conventional sintering of $NaNbO_3$ ceramics. The samples sintered for 0–10 min at 1350 °C consisted of grains with average sizes of approximately 2.5–2.9 μm and a uniform grain-size distribution; however, once the sintering time was increased to 15 min a few large grains of several 10 μm were observed, while the grain size of the matrix remained at approximately 2.8–2.9 μm. The abnormal grain growth was related to the decreased quantity of pores, the decrease in the pore size, and the resulting increase in the grain-boundary-migration velocity, which at this point exceeded the pore-migration velocity and initiated the pore/grain-boundary separation. A further increase of the sintering time resulted in a coarse-grained microstructure with an average grain size of 35–55 μm and a relative density of 95–96 %.

The above results underlined the importance of understanding the processes that are active during the individual sintering stages. The obtained knowledge enabled us to identify the problems related to obtaining high densities and fine-grained microstructures, to choose an alternative sintering technique to overcome these problems and, finally, to produce dense $NaNbO_3$ ceramics with grain sizes ranging from the submicron range up to 50 μm.

5.3 Phase Transition Behaviour of $NaNbO_3$

The last part of the present work reports the results obtained from investigations of the complex phase-transition behaviour of $NaNbO_3$ submicron-sized powders and ceramics with different average grain sizes.

We re-examined the temperature-induced phase transitions of the coarse-grained $NaNbO_3$ ceramics using differential scanning calorimetry (DSC), dielectric spectroscopy and high-temperature XRD. We confirmed the presence of the antiferroelectric *P* phase at RT, which underwent the following sequence of transitions upon heating: 371.4 °C (*P*→*R*), 511 °C (*S*→*T(1)*), 564.7 °C (*T(1)*→*T(2)*), and 642.4 °C (*T(2)*→*U*). In addition, another anomaly was observed in the permittivity curve in the vicinity of 150 °C, but was not detected using DSC and XRD. The detailed dielectric analysis revealed the frequency dependence of the *ε''(T)* peaks, which excluded the presence of a phase transition in this temperature region.

Furthermore, we investigated the effect of the particle or grain size on the phase stability of $NaNbO_3$. The comparison of the DSC curves of the coarse-grained ceramics (grain size of approximately 50 μm) and the submicron-NN powder (particle size of approximately 0.07–0.17 μm) revealed a large difference (about 50 °C) in the temperatures of the main transition peak, which was related to the stabilization of the ferroelectric *Q* phase in the case of the submicron-NN, as confirmed by XRD. The phase

transition of the ferroelectric *Q* phase during heating was studied in detail using high-temperature XRD and the *Q*→*R* transition was found to occur between 265 °C and 325 °C, possibly through a region of coexistence of both phases. The analysis of the Na cuboctahedral cavities revealed a large distortion of the structure at RT, as evidenced by the three tilt directions of the oxygen octahedra and the displacement of the Na cation in the *y*-*z* plane; however, during heating the symmetry of the structure increased and above the *Q*→*R* transition the Na cation was placed in the centre of the *x*-*y* plane and only a slight displacement in the *z* direction was observed. The cuboctahedral cavities were more regular, which was the main reason for the observed symmetrisation of the unit cell. The antiferroelectric *P* and the ferroelectric *Q* phase were found to transform to the same high-temperature *R* phase; however, the transition temperature of the latter was much lower.

In order to investigate the size-induced phase transitions in $NaNbO_3$ ceramics, we prepared a series of ceramic samples with grain sizes ranging from about 0.15 μm to 50 μm and examined them using the XRD, DSC and dielectric measurements. The temperature of the *P*→*R* transition, which occurred at approximately 370 °C in the coarse-grain ceramics, was found to decrease by about 35 °C upon decreasing the average grain size from 50 μm to 0.63 μm. Upon a decrease of the grain size to 0.23 μm we observed the presence of two $NaNbO_3$ phases: the antiferroelectric *P* and the ferroelectric *Q* phase. A further decrease of the grain size to 0.19 μm reduced the amount of the antiferroelectric *P* phase, as is evident from the DSC curves, while the amount of the ferroelectric *Q* phase increased. At a grain size of about 0.15 μm only the ferroelectric *Q* phase was detected. The critical grain size for the inducement of the *P*→*Q* transition was found to be roughly 0.2 μm, which is smaller than for the previous results obtained from the $NaNbO_3$ powders (0.6 μm). This discrepancy may be related to the use of different processing methods and to a more accurate critical-size determination in the present work, since we considered the full grain-size distributions and not only the estimated particle-size values. Despite the fact that samples with grain sizes below 0.6 μm did not reach the closed-porosity state, the determined critical grain size for the inducement of the ferroelectric state is important for the future search of potential applications of the $NaNbO_3$ ceramics.

Finally, we investigated the $NaNbO_3$ phase transition induced by the application of an external electric field. While no ferroelectric phase could be induced at RT, the antiferroelectric *P* phase was found to transform to the ferroelectric *Q* phase upon applying an electric field of 8 kV/mm at 80 °C or a field of 6.5 kV/mm at 200 °C, as confirmed by the occurrence of the ferroelectric hysteresis loops, the butterfly-like strain hysteresis loops and the XRD analysis. The obtained remanent polarization was 32 $\mu C/cm^2$ and the d_{33} piezoelectric coefficient was 28 pC/N. The induced ferroelectric state remained stable upon removal of the electric field and decreasing the temperature to RT, which indicated the irreversible nature of this *P*→*Q* phase transition. This result explained the previously observed absence of the double hysteresis loops in antiferroelectric $NaNbO_3$ ceramics and may limit the application of these materials for high-energy storage capacitors.

6 Acknowledgements

(will be added later)

7 References

Acker, J.; Kungl, H.; Hoffmann, M. J. Influence of Alkaline and Niobium Excess on Sintering and Microstructure of Sodium-Potassium Niobate $(K_{0.5}\ Na_{0.5})NbO_3$. *Journal of the American Ceramic Society* **93**, 1270–1281 (2010).

Ahn, C. W. et al. Sintering Behavior of Lead-Free $(K,Na)NbO_3$-Based Piezoelectric Ceramics. *Journal of the American Ceramic Society* **92**, 2033–2038 (2009).

Ahtee, M.; Glazer, A. M.; Megaw, H. D. The structures of sodium niobate between 480 °C and 575 °C, and their relevance to soft-phonon modes. *Philosophical Magazine* **26**, 995–1014 (1972).

Akhtar, M. J.; Akhtar, Z. U. N.; Jackson, R. A.; Catlow, C. R. A. Computer-Simulation Studies of Strontium-Titanate. *Journal of the American Ceramic Society* **78**, 421–428 (1995).

Allen, T. *Particle Size Measurement: Surface Area and Pore Size Determination* (Chapman & Hall, London, 1997).

Ang, C.; Yu, Z.; Jing, Z. Impurity-induced ferroelectric relaxor behavior in quantum paraelectric $SrTiO_3$ and ferroelectric $BaTiO_3$. *Physical Review B* **61**, 957–961 (2000).

Barrett, E. P.; Joyner, L. G.; Halenda, P. P. The Determination of Pore Volume and Area Distributions in Porous Substances. I. Computations from Nitrogen Isotherms. *Journal of the American Chemical Society* **73**, 373–380 (1951).

Bateman, C. A.; Bennison, S. J.; Harmer, M. P. Mechanism for the Role of Magnesia in the Sintering of Alumina Containing Small Amounts of a liquid Phase. *Journal of the American Ceramic Society* **72**, 1241–1244 (1989).

Berry, K. A.; Harmer, M. P. Effect of MgO Solute on Microstructure Development in Al_2O_3. *Journal of the American Ceramic Society* **69**, 143–149 (1986).

Bouziane, E.; Fontana, M. D.; Ayadi, M. Study of the low-frequency Raman scattering in $NaNbO_3$ crystal. *Journal of Physics: Condensed Matter* **15**, 1387–1395 (2003).

Bron, V. A. Some crystal-chemical relationships in the activated sintering of highly refractory oxides in the solid phase. *Powder Metallurgy and Metal Ceramics* **1**, 339–344 (1964).

Brook, R. J. Pore-Grain Boundary Interactions and Grain Growth. *Journal of the American Ceramic Society* **52**, 56–57 (1969).

Burke, J. E. The Development of Pore-Free Ceramics. In: Somiya, S.; Moriyoshi, Y. (ed.) *Sintering Key Papers*. 3–17 (Elsevier Science Publishing, London, New York, 1989).

Burke, J. E.; Turnbull, D. Recrystallization and grain growth. *Progress in Metal Physics* **3**, 220–292 (1952).

Castro, A.; Jimenez, B.; Hungria, T.; Moure, A.; Pardo, L. Sodium niobate ceramics prepared by mechanical activation assisted methods. *Journal of the European Ceramic Society* **24**, 941–945 (2004).

Chang, H. Y.; Liu, K. S.; Lin, I. N. Conventional and Microwave Sintering Studies of $SrTiO_3$. *Journal of Materials Research* **10**, 2052–2059 (1995).

Chen, I. W.; Wang, X. H. Sintering dense nanocrystalline ceramics without final-stage grain growth. *Nature* **404**, 168–171 (2000).

Coble, R. L. Diffusion Models for Hot Pressing with Surface Energy and Pressure Effects as Driving Forces. *Journal of Applied Physics* **41**, 4798–4807 (1970).

Coble, R. L. Initial Sintering of Alumina and Hematite. *Journal of the American Ceramic Society* **41**, 55–62 (1958).

Coble, R. L. Sintering Crystalline Solids. I. Intermediate and Final State Diffusion Models. *Journal of Applied Physics* **32**, 787–792 (1961).

Coblenz, W. S.; Dynys, J. M.; Cannon, R. M.; Coble, R. L. Initial Stage Solid State Sintering Models. A Critical Analysis and Assessment. In: Kuczynski, G. C. (ed.) *Materials science reseach*. 141–157 (Plenum Press, New York, 1980).

Cross, L. E.; Nicholson, B. J. LV. The optical and electrical properties of single crystal of sodium niobate. *Philosophical Magazine* **46**, 453–466 (1955).

Darlington, C. N. W.; Knight, K. S. High-temperature phases of $NaNbO_3$ and $NaTaO_3$. *Acta Crystallographica B* **55**, 24–30 (1999).

Darlington, C. N. W.; Megaw, H. D. The low-temperature phase transition of sodium niobate and the structure of the low-temperature phase, N. *Acta Crystallographica B* **29**, 2171–2185 (1973).

Dungan, R. H.; Golding, R. D. Metastable Ferroelectric Sodium Niobate. *Journal of the American Ceramic Society* **47**, 73–76 (1964).

Egerton, L.; Dillon, D. M. Piezoelectric and Dielectric Properties of Ceramics in the

System Potassium-Sodium Niobate. *Journal of the American Ceramic Society* **42**, 438–442 (1959).

Fletcher, N. H.; Hilton, A. D.; Ricketts, B. W. Optimization of energy storage density in ceramic capacitors. *Journal of Physics D: Applied Physics* **29**, 253–258 (1996).

Frenkel, J. Viscous flow of crystalline bodies under the action of surface tension. *Journal of Physics (USSR)* **9**, 385–391 (1945).

German, R. M. *Sintering theory and practice* (John Wiley & Sons, New York, 1996).

German, R. M.; Munir, Z. A. Surface-Area Reduction during Isothermal Sintering. *Journal of the American Ceramic Society* **59**, 379–383 (1976).

Glazer, A. M.; Megaw, H. D. The structure of sodium niobate (T2) at 600 °C, and the cubic-tetragonal transition in relation to soft-phonon modes. *Philosophical Magazine* **25**, 1119–1135 (1972).

Glazer, A. M.; Megaw, H. D. Studies of the lattice parameters and domains in the phase transitions of $NaNbO_3$. *Acta Crystallographica Section A* **29**, 489–495 (1973).

Hao, X. H.; Zhou, J.; An, S. L. Effects of PbO Content on the Dielectric Properties and Energy Storage Performance of $(Pb_{0.97}La_{0.02})(Zr_{0.97}Ti_{0.03})O_3$ Antiferroelectric Thin Films. *Journal of the American Ceramic Society* **94**, 1647–1650 (2011).

Harmer, M. P.; Brook, R. J. Fast Firing - Microstructural Benefits. *Transactions and Journal of the British Ceramic Society* **80**, 147–148 (1981).

Horn, D. S.; Messing, G. L. Anisotropic grain growth in TiO_2-doped alumina. *Materials Science and Engineering A* **195**, 169–178 (1995).

Hsueh, C. H.; Evans, A. G.; Coble, R. L. Microstructure Development during Final Intermediate Stage Sintering – I. Pore Grain-Boundary Separation. *Acta Metallurgica* **30**, 1269–1279 (1982).

Jaeger, R. E.; Egerton, L. Hot Pressing of Potassium-Sodium Niobates. *Journal of the American Ceramic Society* **45**, 209–213 (1962).

Jaffe, B.; Cook, W. R. J.; Jaffe, H. *Piezoelectric Ceramics* (Academic Press, London, New York, 1971).

Jenko, D.; Benčan, A.; Malič, B.; Holc, J.; Kosec, M. Electron microscopy studies of potassium sodium niobate ceramics. *Microscopy and Microanalysis* **11**, 572–580 (2005).

Jimenez, R.; Sanjuan, M. L.; Jimenez, B. Stabilization of the ferroelectric phase and relaxor-like behaviour in low Li content sodium niobates. *Journal of Physics: Condensed*

Matter **16**, 7493–7510 (2004).

Johnson, D. L.; Cutler, I. B. Diffusion Sintering: I, Initial Stage Sintering Models and Their Application to Shrinkage of Powder Compacts. *Journal of the American Ceramic Society* **46**, 541–545 (1963).

Kang, S.-J. L. *Sintering: Densification, Grain Growth, and Microstructure* (Elsevier Butterworth-Heinemann, Oxford, 2005).

Kang, S.-J. L.; Jung, Y.-I. Sintering kinetics at final stage sintering: model calculation and map construction. *Acta Materialia* **52**, 4573–4578 (2004).

Kanters, J.; Eisele, U.; Rödel, J. Effect of initial grain size on sintering trajectories. *Acta Materialia* **48**, 1239–1246 (2000).

Kay, H. F.; Vousden, P. XCV. Symmetry changes in barium titanate at low temperatures and their relation to its ferroelectric properties. *Philosophical Magazine* **40**, 1019–1040 (1949).

Kim, D.-H.; Kim, C. H. Entrapped Gas Effect in the Fast Firing of Yttria-Doped Zirconia. *Journal of the American Ceramic Society* **75**, 716–718 (1992).

Kingery, W. D.; Berg, M. Study of the Initial Stages of Sintering Solids by Viscous Flow, Evaporation-Condensation, and Self-Diffusion. *Journal of Applied Physics* **26**, 1205–1212 (1955).

Kingery, W. D.; Bowen, H. K.; Uhlmann, D. R. *Introduction to ceramics* (John Wiley & Sons, Inc., New York, 1976).

Kinoshita, K.; Yamaji, A. Grain-size effects on dielectric properties in barium titanate ceramics. *Journal of Applied Physics* **47**, 371–373 (1976).

Kittel, C. Theory of Antiferroelectric Crystals. *Physical Review* **82**, 729–732 (1951).

Kodaira, K.; Shioya, J.; Shimada, S.; Matsushita, T. Sintering and Dielectric-Properties of $KNbO_3$. *Journal of Materials Science Letters* **1**, 277–278 (1982).

Konieczny, K. Pyroelectric and dielectric study of $NaNbO_3$ single crystals. *Materials Science and Engineering B* **60**, 124–127 (1999).

Kosec, M.; Kolar, D. Activated Sintering and Electrical Properties of $NaKNbO_3$. *Materials Research Bulletin* **10**, 335–339 (1975).

Kuczynski, G. C. Self-diffusion in sintering of metallic particles. *Transactions AIME* **185**, 169–178 (1949a).

Kuczynski, G. C. Study of the Sintering of Glass. *Journal of Applied Physics* **20**, 1160–1163 (1949b).

Lanfredi, S.; Dessemond, L.; Rodrigues, A. C. M. Dense ceramics of $NaNbO_3$ produced from powders prepared by a new chemical route. *Journal of the European Ceramic Society* **20**, 983–990 (2000).

Lange, F. F. Sinterability of Agglomerated Powders. *Journal of the American Ceramic Society* **67**, 83–89 (1984).

Lefkowitz, I.; Lukaszewicz, K.; Megaw, H. D. The high-temperature phases of sodium niobate and the nature of transitions in pseudosymmetric structures. *Acta Crystallographica* **20**, 670–683 (1966).

Lehl, H. (ed.) Niob. Teil B 4, Alkalioxoniobate, Niobverbindungen mit weiteren Kationen, Kohlenstoffverbindungen des Niob. In: *Gmelins Handbuch der anorganischen Chemie*. 1–473 (Chemie, Weinheim, 1973).

Lewis, G. V.; Catlow, C. R. A. Defect studies of doped and undoped barium titanate using computer simulation techniques. *Journal of Physics and Chemistry of Solids* **47**, 89–97 (1986).

Liu, H. B.; Dkhil, B. A brief review on the model antiferroelectric $PbZrO_3$ perovskite-like material. *Zeitschrift für Kristallographie* **226**, 163–170 (2011).

Malič, B.; Benčan, A.; Rojac, T.; Kosec, M. Lead-free Piezoelectrics Based on Alkaline Niobates: Synthesis, Sintering and Microstructure. *Acta Chimica Slovenica* **55**, 719–726 (2008).

Matsumoto, R. L. K. Generation of Powder Compaction Response Diagrams. *Journal of the American Ceramic Society* **69**, C246–C247 (1986).

Matthias, B. T. New Ferroelectric Crystals. *Physical Review* **75**, 1771–1771 (1949).

Megaw, H. D. 7 Phases of Sodium Niobate. *Ferroelectrics* **7**, 87–89 (1974).

Molak, A. The Influence of Reduction in Valency of Nb Ions on the Antiferroelectric Phase-Transition in $NaNbO_3$. *Solid State Communications* **62**, 413–417 (1987).

Mostaghaci, H.; Brook, R. J. Fast-Firing of Non Stoichiometric $BaTiO_3$. *Transactions and Journal of the British Ceramic Society* **80**, 148–149 (1981).

Nichols, F. A. Further Comments on the Theory of Grain Growth in Porous Compacts. *Journal of the American Ceramic Society* **51**, 468–468 (1968).

Nobre, M. A. L.; Longo, E.; Leite, E. R.; Varela, J. A. Synthesis and sintering of ultra fine $NaNbO_3$ powder by use of polymeric precursors. *Materials Letters* **28**, 215–220 (1996).

Powder Diffraction File, *Version 4.1102*. (International Center for Diffraction Data, Newtown Square, 2011).

Petricek, V.; Dusek, M. *The Crystallographic Computing System JANA2006*, *Version 01/07/2011* (Institute of Physics, Academy of Scienecs of the Czech Republic, Prague, 2006).

Pirc, R.; Blinc, R. Vogel-Fulcher freezing in relaxor ferroelectrics. *Physical Review B* **76**, 020101–3 (2007).

Pithan, C. et al. Microemulsion mediated synthesis of nanocrystalline $(K_x,Na_{1-x})NbO_3$ powders. *Journal of Crystal Growth* **280**, 191–200 (2005).

Pithan, C. et al. Consolidation, microstructure and crystallography of dense $NaNbO_3$ ceramics with ultra-fine grain size. *Journal of the Ceramic Society of Japan* **114**, 995–1000 (2006).

Polotai, A.; Breece, K.; Dickey, E.; Randall, C.; Ragulya, A. A novel approach to sintering nanocrystalline barium titanate ceramics. *Journal of the American Ceramic Society* **88**, 3008–3012 (2005).

Raevski, I. P.; Prosandeev, S. A. A new, lead free, family of perovskites with a diffuse phase transition: $NaNbO_3$-based solid solutions. *Journal of Physics and Chemistry of Solids* **63**, 1939–1950 (2002).

Raevskii, I. P. et al. A new phase transition in sodium niobate. *Technical Physics Letters* **26**, 744–746 (2000).

Rahaman, M. N. *Ceramic Processing and Sintering* (Marcel Dekker, New York, 2003).

Reed, J. S. *Principles of Ceramics Processing* (John Wiley & Sons, New York, 1995).

Reznitchenko, L. A.; Turik, A. V.; Kuznetsova, E. M.; Sakhnenko, V. P. Piezoelectricity in $NaNbO_3$ ceramics. *Journal of Physics: Condensed Matter* **13**, 3875–3881 (2001).

Rietveld, H. A profile refinement method for nuclear and magnetic structures. *Journal of Applied Crystallography* **2**, 65–71 (1969).

Rödel, J. et al. Perspective on the Development of Lead-free Piezoceramics. *Journal of the American Ceramic Society* **92**, 1153–1177 (2009).

Rodriguez-Carvajal, J. *FullProf Suite Program*, *Version 2.05* (Rodriguez-Carvajal J., Grenoble, 2011).

Rojac, T.; Kosec, M.; Malič, B.; Holc, J. Mechanochemical synthesis of $NaNbO_3$. *Materials Research Bulletin* **40**, 341–345 (2005).

Rojac, T. et al. A study of the mechanochemical synthesis of $NaNbO_3$. *Journal of the European Ceramic Society* **27**, 2265–2271 (2007).

Rollett, A. D.; Srolovitz, D. J.; Anderson, M. P. Simulation and theory of abnormal grain growth – anisotropic grain boundary energies and mobilities. *Acta Metallurgica* **37**, 1227–1240 (1989).

Saito, T.; Adachi, H.; Wada, T.; Adachi, H. Pulsed-Laser Deposition of Ferroelectric $NaNbO_3$ Thin Films. *Japanese Journal of Applied Physics* **44**, 6969–6972 (2005).

Saito, Y. et al. Lead-free piezoceramics. *Nature* **432**, 84–87 (2004).

Sakowski-Cowley, A. C.; Lukaszewicz, K.; Megaw, H. D. The structure of sodium niobate at room temperature, and the problem of reliability in pseudosymmetric structures. *Acta Crystallographica B* **25**, 851–865 (1969).

Sawaguchi, E.; Kittaka, T. Antiferroelectricity and Ferroelectricity in Lead Zirconate. *Journal of the Physical Society of Japan* **7**, 336–337 (1952).

Sawaguchi, E.; Maniwa, H.; Hoshino, S. Antiferroelectric Structure of Lead Zirconate. *Physical Review* **83**, 1078–1078 (1951).

Shafer, M. W.; Roy, R. Phase Equilibria in the System Na_2O-Nb_2O_5. *Journal of the American Ceramic Society* **42**, 482–486 (1959).

Shannon, R. Revised effective ionic radii and systematic studies of interatomic distances in halides and chalcogenides. *Acta Crystallographica A* **32**, 751–767 (1976).

Shiratori, Y. et al. Polymorphism in micro-, submicro-, and nanocrystalline $NaNbO_3$. *Journal of Physical Chemistry B* **109**, 20122–20130 (2005).

Shiratori, Y.; Magrez, A.; Fischer, W.; Pithan, C.; Waser, R. Temperature-induced Phase Transitions in Micro-, Submicro-, and Nanocrystalline $NaNbO_3$. *Journal of Physical Chemistry C* **111**, 18493–18502 (2007).

Shuvaeva, V. A. et al. Crystal structure of the electric-field induced ferroelectric phase of $NaNbO_3$. *Ferroelectrics* **141**, 307–311 (1993).

Snyder, R. L.; Fiala, J.; Bunge, H. J. *Defect and Microstructure Analysis by Diffraction* (Oxford University Press, New York, 1999).

Srdić, V. V.; Winterer, M.; Hahn, H. Sintering Behavior of Nanocrystalline Zirconia Doped with Alumina Prepared by Chemical Vapor Synthesis. *Journal of the American Ceramic Society* **83**, 1853–1860 (2000).

Stevanovic, S.; Zeljkovic, V.; Obradovic, N.; Labus, N. Investigation of Sintering Kinetics of ZnO by Observing Reduction of the Specific Surface Area. *Science of Sintering* **39**, 259–265 (2007).

Takuya, M. et al. Piezoelectric Properties of Epitaxial $NaNbO_3$ Thin Films Deposited on (001)$SrRuO_3$/Pt/MgO Substrates. *Japanese Journal of Applied Physics* **46**, 6960–6963 (2007).

Tan, X. L.; Ma, C.; Frederick, J.; Beckman, S.; Webber, K. G. The Antiferroelectric <-> Ferroelectric Phase Transition in Lead-Containing and Lead-Free Perovskite Ceramics. *Journal of the American Ceramic Society* **94**, 4091–4107 (2011).

Uchino, K. *Ferroelectric Devices* (Marcel Dekker, New York, Basel, 2000).

Vojisavljević, K. et al. Structural characterization of mechanically milled ZnO: influence of zirconia milling media. *Journal of Physics: Condensed Matter* **20**, 475202–9 (2008).

Vousden, P. The structure of ferroelectric sodium niobate at room temperature. *Acta Crystallographica* **4**, 545–551 (1951).

Wada, T.; Tsuji, K.; Saito, T.; Matsuo, Y. Ferroelectric $NaNbO_3$ ceramics fabricated by spark plasma sintering. *Japanese Journal of Applied Physics* **42**, 6110–6114 (2003).

Wang, J. D.; Raj, R. Estimate of the Activation-Energies for Boundary Diffusion from Rate-Controlled Sintering of Pure Alumina, and Alumina Doped with Zirconia or Titania. *Journal of the American Ceramic Society* **73**, 1172–1175 (1990).

Wang, X. B. et al. High temperature Raman study of phase transitions in antiferroelectric $NaNbO_3$. *Journal of Molecular Structure* **385**, 1–6 (1996).

Wang, X. H. et al. Two-step sintering of ceramics with constant grain-size, II: $BaTiO_3$ and Ni-Cu-Zn ferrite. *Journal of the American Ceramic Society* **89**, 438–443 (2006).

Wang, Y.; Damjanovic, D.; Klein, N.; Setter, N. High-Temperature Instability of Li- and Ta-Modified (K,Na)NbO_3 Piezoceramics. *Journal of the American Ceramic Society* **91**, 1962–1970 (2008).

Waser, R.; Böttger, U.; Tiedke, S. (ed.) *Polar Oxides: Properties, Characterization, and Imaging* (Wiley-VCH, Weinheim, 2005).

Wilcox, D.; Dove, B.; McDavid, D.; Greer, D. *UTHSCSA Image Tool for Windows*, *Version 3.0* (University of Texas Health Science Center, San Antonio, 2002).

Wood, E. Polymorphism in potassium niobate, sodium niobate, and other ABO_3 compounds. *Acta Crystallographica* **4**, 353–362 (1951).

Yuzyuk, Y. I. et al. Ferroelectric Q-phase in a $NaNbO_3$ epitaxial thin film. *Applied Physics Letters* **96**, 222904–3 (2010).

Yuzyuk, Y. I. et al. Modulated phases in $NaNbO_3$: Raman scattering, synchrotron X-ray diffraction, and dielectric investigations. *Journal of Physics: Condensed Matter* **17**, 4977–4990 (2005).

Zhen, Y. H.; Li, J. F. Normal sintering of $(K,Na)NbO_3$-based ceramics: Influence of sintering temperature on densification, microstructure, and electrical properties. *Journal of the American Ceramic Society* **89**, 3669–3675 (2006).

8 Index of Figures

9 Index of Tables

10 Appendix

10.1 Na–O Interatomic Distances in the Coordination Sphere of Na Obtained from the Structural Refinement of the Submicron-NN Powder at Different Temperatures

RT			
Na1	–O1	2.91(6)	1x
	–O1	2.72(6)	1x
	–O1	2.35(6)	1x
	–O1	3.17(6)	1x
	–O3	2.88(5)	2x
	–O3	2.44(4)	2x
	–O4	3.02(4)	2x
	–O4	2.74(4)	2x
Na2	–O2	3.18(6)	2x
	–O2	2.44(6)	1x
	–O2	2.39(6)	1x
	–O3	2.91(4)	2x
	–O3	2.88(4)	2x
	–O4	3.03(5)	2x
	–O4	2.31(4)	2x

250 °C			
Na1	–O1	3.04(6)	1x
	–O1	2.57(6)	1x
	–O1	2.44(6)	1x
	–O1	3.11(6)	1x
	–O3	2.74(4)	2x
	–O3	2.59(4)	2x
	–O4	3.13(4)	2x
	–O4	2.61(4)	2x
Na2	–O2	3.18(5)	1x
	–O2	2.45(5)	1x
	–O2	3.02(5)	1x
	–O2	2.55(5)	1x
	–O3	2.89(3)	2x
	–O3	2.95(3)	2x
	–O4	3.05(3)	2x
	–O4	2.29(3)	2x

420 °C			
Na1	–O1	2.63(7)	4x
	–O2	2.96(18)	2x
	–O3	3.07(16)	2x
	–O4	3.00(17)	2x
	–O5	2.60(18)	2x
Na2	–O1	2.93(7)	4x
	–O2	2.50(16)	2x
	–O3	3.03(16)	2x
	–O4	2.82(16)	2x
	–O5	2.43(18)	2x
Na3	–O1	2.67(7)	4x
	–O2	2.63(18)	2x
	–O3	2.5(2)	2x
	–O4	2.8(2)	2x
	–O5	3.08(18)	2x
Na4	–O1	2.89(7)	4x
	–O2	3.1(3)	2x
	–O3	2.5(3)	2x
	–O4	2.5(3)	2x
	–O5	3.0(2)	2x

11 Personal Bibliography

11.1 Scientific Articles from the Thesis

1. Koruza, J.; Tellier, J.; Malič, B.; Bobnar, V.; Kosec, M. Phase transitions of sodium niobate powder and ceramics, prepared by solid state synthesis. *Journal of Applied Physics* **108**, 113509 (2010).

2. Koruza, J.; Malič, B.; Kosec, M. Microstructure evolution during sintering of sodium niobate. *Journal of the American Ceramic Society* **94**, 4174–4178 (2011).

3. Popovič, A.; Bencze, L; Koruza, J.; Malič, B.; Kosec, M. Knudsen effusion mass spectrometric approach to the thermodynamics of Na_2O-Nb_2O_5 system. *International Journal of Mass Spectrometry* **309**, 70–78 (2012).

4. Koruza, J.; Malilč, B.; Noshchenko, O.; Kosec, M. Top-down processing of $NaNbO_3$ nanopowder. *Journal of Nanomaterials* **2012**, 1–7 (2012).

11.2 Other Scientific Articles

1. Malič, B.; Razpotnik, H.; Koruza, J.; Kokalj, S.; Cilenšek, J.; Kosec, M. Linear thermal expansion of lead-free piezoelectric $K_{0.5}Na_{0.5}NbO_3$ ceramics in a wide temperature ranged. *Journal of the American Ceramic society* **94**, 2273–2275 (2011).

2. Seo, Y.-H.; Benčan, A.; Koruza, J.; Malič, B.; Kosec, M.; Webber, K. Compositional dependence of R-curve behavior in soft $Pb(Zr_{1-x}Ti_x)O_3$ ceramics. *Journal of the American Ceramic Society* **94**, 4419–4425 (2011).

3. Seo, Y.-H.; Webber, K.;, Benčan, A.; Koruza, J.; Malič, B.; Kosec, M.; Rödel, J. Deconvolving ferroelastic and phase transformation toughening in $Pb(Zr_{1-x}Ti_x)O_3$ and $Pb_{1-y}La_y(Zr_{1-x}Ti_x)O_3$. *Journal of the American Ceramic Society* **95**, 3713–3715 (2012).

11.3 Conference Contributions

11.3.1 Published Scientific Conference Contributions

1. Rožič, B.; Koruza, J.; Kutnjak, Z.; Malič. B.; Kosec, M. Direct measurements of the electrocaloric effect in lead-free $K_{0.5}Na_{0.5}NbO_3$-$SrTiO_3$ ceramics sintered in air. In: Pullar, R. (ed.) *Proceedings of the 21th International Symposium on Applications of Ferroelectrics, 11th European Conference on the Applications of Polar Dielectrics, 4th International Symposium Piezoresponse Force Microscopy and Nanoscale Phenomena in Polar Materials (ISAF/ECAPD/PFM) 2012*. 1–4 (Danvers: IEEE, Aveiro, 2012).

2. Rožič, B.; Kutnjak, Z.; Uršič, H.; Malič, B.; Holc, J.; Koruza, J.; Kupec, A.; Kosec, M. Electrocaloric thermometry : an experimental method for the direct electrocaloric measurements. In: Belavič, D.; Šorli, I. (ed.) *Proceedings of the 48th International Conference on Microelectronics, Devices and Materials & the Workshop on Ceramic Microsystems*. 339–343 (MIDEM - Society for Microelectronics, Electronic Components and Materials, Otočec, 2012).

3. Koruza, J.; Tellier, J.; Malič, B.; Kosec, M. Phase transitions of the $NaNbO_3$ submicron-sized powder between room temperature and 700 °C. In: Petelin, D.; Tavčar, A.; Kaluža, B. (ed.) *Proceedings of the 4th Jožef Stefan International Postgraduate School Students Conference*. 247–253 (Mednarodna podiplomska šola Jožefa Stefana, Ljubljana, 2012).

11.3.2 Published Scientific Conference Contributions – Invited Talks

1. Malič, B.; Benčan, A.; Koruza, J.; Glinšek, S.; Rojac, T.; Kosec, M. Understanding and controlling microstructure evolution in lead-free piezoelectric sodium potassium niobate ceramics. In: *Electroceramics XII*. CD proceedings (NTNU, Trondheim 2010).

2. Malič, B.; Popovič, A.; Koruza, J.; Kosec, M. Vapour pressure over alkali niobate ceramics followed by Knudsen effusion mass spectrometry as a tool for optimisation of processing and properties. In: *Electroceramics XIII*. 42 (University of Twente, Enschede, 2012).

3. Rožič, B.; Kutnjak, Z.; Malič, B.; Uršič, H.; Koruza, J.; Kosec, M.; Pirc, R.; Lu, S.-G.; Zhang, Q. M. Electrocalorics : materials for application in cooling and heating new generation devices. In: *11th Symposium of Physics of the University of Maribor*. (CAMTP, Maribor, 2012).

11.3.3 Published Scientific Conference Contributions - Abstracts

1. Rožič, B.; Kutnjak, Z.; Malič, B.; Uršič, H.; Koruza, J.; Holc, J.; Kosec, M.; Pirc,

R.; Lu, S.-G.; Pirc, R.; Neese, B.; Zhang, Q. M. Giant electrocaloric effect in organic and inorganic ferroelectric and relaxor ferroelectric materials. In: *21th International Symposium on Applications of Ferroelectrics, 11th European Conference on the Applications of Polar Dielectrics, 4th International Symposium Piezoresponse Force Microscopy and Nanoscale Phenomena in Polar Materials (ISAF/ECAPD/PFM) 2012*. 227 (IEEE Ultrasonics, Ferroelectrics, and Frequency Control Society, Aveiro, 2012).

2. Seo, Y.-H.; Koruza, J.; Benčan, A.; Franzbach, D.; Malič, B.; Kosec, M.; Webber, K. The effect of nonlinear processes on the saturated remanent state of lead zirconate titanate. In: *21th International Symposium on Applications of Ferroelectrics, 11th European Conference on the Applications of Polar Dielectrics, 4th International Symposium Piezoresponse Force Microscopy and Nanoscale Phenomena in Polar Materials (ISAF/ECAPD/PFM) 2012*. 501 (IEEE Ultrasonics, Ferroelectrics, and Frequency Control Society, Aveiro, 2012).

3. Koruza, J.; Seo, Y.-H.; Benčan, A.; Malič, B.; Kosec, M.; Webber, K. Lattice distortions in donor doped $Pb(Zr,Ti)O_3$ depending on the Zr/Ti ratio. In: *13th European Powder Diffraction Conference*. 133 (EPDIC, Grenoble, 2012).

4. Rožič, B.; Kutnjak, Z.; Uršič, H.; Malič, B.; Koruza, J.; Kosec, M.; Pirc, R.; Lu, S.-G.; Neese, B.; Zhang, Q. M. Nano-electrocalorics : nanomaterials for application in cooling and heating new generation devices. In: Mihailović, D.; Kobe, S.; Kaučič, V.; Osterman, N.; Novak Tušar, N.; Žužek Rozman, K.; Šturm, S. (ed.) *SLONANO 2012*. 66 (Institut Jožef Stefan, Ljubljana, 2012).

5. Koruza, J.; Malič, B.; Kosec, M. Microstructure design of sodium niobate ceramics. In: *Electroceramics XIII*. 50 (University of Twente, Enschede, 2012).

6. Vijatović Petrović, M. M.; Bobić, J. D.; Curecheriu, L. P.; Koruza, J.; Stojanović, B. Synthesis procedure and properties of $NiFe_2O_4$-$BaTiO_3$ composites. In: *Joint Conference COST SIMUFER MP0904 action "Single-and multiphase ferroelectrics and multiferoics with restricted geometries" and the 9th Edition IEEE-ROMSC 2012*. 59 (University of Iasi, Iasi, 2012).

7. Koruza, J.; Malič, B.; Noshchenko, O.; Kosec, M. A top-down approach for preparation of sodium niobate nanopowder. In: Godec, M.; Donik, Č.; Paulin, I.; Kocijan, A. (ed.) *20th Conference on Materials and Technology*. 82 (Inštitut za kovinske materiale in tehnologije, Portorož, 2012).

8. Koruza, J.; Malič, B.; Trefalt, G.; Kosec, M. Microstructure evolution during two-stage sintering of sodium niobate. In: *International Conference on Sintering 2011*. 201 (KAIST, Jeju, 2011).

9. Koruza, J.; Malič, B.; Trefalt, G.; Kosec, M. Microstructure development upon two-stage sintering of nano-sodium niobate. In: Godec, M. (ed.) *19th Conference on Materials and Technology*. 83 (Inštitut za kovinske materiale in tehnologije, Portorož, 2011).

10. Koruza, J.; Tellier, J.; Malič, B.; Kosec, M. Fazne premene natrijevega niobata. In: Pribošič, I.; Krnel, K. (ed.) *5. dan mladih raziskovalcev*. 26 (Institut Jožef Stefan, Ljubljana, 2011).

11. Hreščak, J.; Koruza, J.; Benčan, A.; Kosec, M. Synthesis, sintering and characterisation of strontium doped $K_{0.5}Na_{0.5}NbO_3$ ceramics. In: Srdić, V. V; Mitoseriu, L. (ed.) *The Ninth Students' Meeting and Application of Ceramics, SM-2011 and the Second Early Stage Researchers Workshop, COST MP0904*. 128 (University of Novi Sad, Novi Sad, 2011).

12. Koruza, J.; Malič, B.; Kosec, M. Study of the sintering process and microstructure evolution in sodium niobate. In: *Electroceramics XII*. CD proceedings (NTNU, Trondheim, 2010).

13. Koruza, J.; Tellier, J.; Malič, B.; Kosec, M. Structural behaviour of sodium niobate Q polymorph between 25 °C and 420 °C. In: *12th European Powder Diffraction Conference, EPDIC12*. 103 (EPDIC, Darmstadt, 2010).

14. Koruza, J.; Malič, B.; Kosec, M. Microstructure evolution during sintering of sodium niobate. In: Jenko, M. (ed.) *18th Conference on Materials and Technology*. 27 (Inštitut za kovinske materiale in tehnologije, Portorož, 2010).

15. Koruza, J.; Malič, B.; Kosec, M. Razvoj mikrostrukture med procesom sintranja natrijevega niobata. In: Kuščer, D.; Perc, B. (ed.) *4. Dan Mladih Raziskovalcev KMBO*. 31 (Institut Jožef Stefan, Ljubljana, 2010).

16. Koruza, J.; Malič, B.; Kosec, M. Study of the microstructure evolution during air sintering of sodium niobate. In: Benčan, A.; Kuščer, D.; Malič, B.; Kosec, M. (ed.) *Workshop on structural characterisation*. 20 (Institut Jožef Stefan, Ljubljana, 2010).

17. Koruza, J.; Malič, B.; Kosec, M. Sintranje piezoelektričnih keramičnih materialov na osnovi alkalijskih niobatov. In: Kaluža, B.; Eleršič, K.; Pogorelec, B.; Šetina, B., Vahčič, M. (ed.) *2nd Jožef Stefan International Postgraduate School Students Conference*. 56 (Mednarodna podiplomska šola Jožefa Stefana, Ljubljana, 2010).

18. Koruza, J.; Malič, B.; Kosec, M. Študij sinteze natrijevega niobata v trdnem staju. In: Iskra, J.; Milošev, I. (ed.) *Dan mladih raziskovalcev 2009*. 1 (Institut Jožef Stefan, Ljubljana, 2009).

19. Koruza, J.; Malič, B.; Kosec, M. The influence of milling of Na_2CO_3 synthesis and sintering of sodium niobate. In: *Piezo 2009 : Electroceramics for end-users IV*. 62 (Piezo Institute, Zakopane, 2009).

20. Koruza, J.; Malič, B.; Kosec, M. Study of the solid state synthesis of sodium niobate. In: Stojanivić, B.; Pardo, L.; Vilarinho, P. (ed.) *2nd Training School and 6th Workshop COST 539 ELENA Advanced Functional Characterization of Nanostructured Materials*. 72– 73 (Verzal, Madrid, 2009).

21. Koruza, J.; Malič, B.; Kosec, M. Solid state synthesis of sodium. In: Jenko, M. (ed.) *1st International Conference on Materials and Technology*. 34 (Inštitut za kovinske materiale in tehnologije, Portorož, 2008).